



Qualification of innovative floating substructures for 10MW wind turbines and water depths greater than 50m

Project acronym LIFES50+
Grant agreement 640741
Collaborative project
Start date 2015-06-01
Duration 40 months

Deliverable D4.6 Model validation against experiments and map of model accuracy across load cases

Lead Beneficiary DTU
Due date 2018-10-31
Delivery date 2018-11-01
Dissemination level Public
Status Final
Classification Unrestricted

Keywords Validation, accuracy, numerical models, state-of-the-art, floating wind turbines

Company document number [Click here to enter text.](#)



The research leading to these results has received funding from the European Union Horizon2020 programme under the agreement H2020-LCE-2014-1-640741.

Disclaimer

The content of the publication herein is the sole responsibility of the publishers and it does not necessarily represent the views expressed by the European Commission or its services.

While the information contained in the documents is believed to be accurate, the authors(s) or any other participant in the LIFES50+ consortium make no warranty of any kind with regard to this material including, but not limited to the implied warranties of merchantability and fitness for a particular purpose.

Neither the LIFES50+ Consortium nor any of its members, their officers, employees or agents shall be responsible or liable in negligence or otherwise howsoever in respect of any inaccuracy or omission herein.

Without derogating from the generality of the foregoing neither the LIFES50+ Consortium nor any of its members, their officers, employees or agents shall be liable for any direct or indirect or consequential loss or damage caused by or arising from any information advice or inaccuracy or omission herein.

Document information

Version	Date	Description
1	2018-10-04	<p>Draft</p> <p>Prepared by Madsen, F.J., Pegalajar-Jurado, A., Bredmose, H., Faerron-Guzman, R., Müller, K., Lemmer, F.</p> <p>Reviewed by Thys, M., Manjock, A.</p> <p>Approved by Bredmose, H.</p>
2	2018-10-30	<p>Submitted to project coordinator</p> <p>Prepared by Madsen, F.J., Pegalajar-Jurado, A., Bredmose, H., Faerron-Guzman, R., Müller, K., Lemmer, F.</p> <p>Reviewed by Bredmose, H.</p> <p>Approved by Bredmose, H.</p>
3	2018-10-31	<p>Final version for QA before submission</p> <p>Prepared by Bredmose, H.</p> <p>Reviewed by Jan Arthur Norbeck</p> <p>Approved by Petter Andreas Berthelsen</p>

Authors	Organization
Madsen, F.J.	DTU
Pegalajar-Jurado, A.	DTU
Bredmose, H.	DTU
Faerron-Guzman, R.	USTUTT
Müller, K.	USTUTT
Lemmer, F.	USTUTT

Contributors	Organization
Yu, W.	USTUTT
Fröhlich, C.	USTUTT

Definitions & Abbreviations

WP	Work Package
SoA	State of the Art
PSD	Power Spectral Density
HiL	Hardware in the Loop
DoF	Degree of Freedom
RNA	Rotor-Nacelle Assembly
QTF	Quadratic Transfer Function
QuLAF	Quick Load Analysis of Floating wind turbines
RWT	Reference Wind Turbine
EoM	Equation of Motion
DEL	Damage-Equivalent Load
FFT	Fast Fourier Transform
iFFT	Inverse Fast Fourier Transform
PDF	Probability Density Function
SLOW	Simplified Low-Order Wind turbine
TSR	Tip-Speed Ratio

Executive Summary

Different numerical tools are required for different stages in the design of a floating offshore wind substructure. Simplified, low-order tools are useful to explore various design variations in the early stages, while state-of-the-art (SoA) models are employed to assess the final design under several environmental conditions. The numerical tools can be benchmarked against physical tests and compared to each other. This is the aim of the present deliverable which provides an assessment of the state-of-the-art and simplified numerical models for the two public floaters of the LIFES50+ project.

For the OO-Star Wind Floater Semi 10MW, the design-driving load cases are identified as DLC 1.2 (normal environment), 1.6 (severe sea state) and 6.1 (extreme environment), referencing work of WP7. The OO-Star FAST model presented in D4.5 is adapted and compared to test results of DLC 1.6 and 6.1. A global linear damping matrix is calibrated for each sea state such that the standard deviation in each degree of freedom is matched for a subset of the full time series. The results show that this approach is viable and generally yields predictions within 10% error at the 95% percentile of the response's exceedance probability for the full test duration. We find that a better match may be possible if the damping calibration is carried out for simulations with the same duration as the tests, or if the full second-order solution is used instead of the Newman's approximation.

The OO-Star SoA model of D4.5 with linear radiation-diffraction forcing is further used to benchmark a simplified frequency-domain model, QULAF. The two models are compared for ten environmental conditions within DLC 1.2. The tower-base moment is estimated by the frequency-domain model with errors up to 12% for wave-only cases and 7% for wind and wave cases, and CPU speeds around 1300 and 2700 times faster than real time, respectively.

For the NAUTILUS-DTU10, the design-driving load cases identified in D7.7 are also DLC 1.2, 1.6 and 6.1. The NAUTILUS FAST model of D4.5 is adapted and compared to model basin test results of DLC 1.6 and 6.1. The damping is calibrated through adjustment of the drag coefficients of the different Morison elements. While the calibration of the drag coefficients yields a good match in the slow-drift response for surge and sway in the pink noise test and provides good results in the wave-frequency range, the low-frequency response for the irregular wave cases is generally under-predicted. This is linked to a simplified and quasi-static representation of the mooring system; difficulties in achieving a calibrated damping that can reproduce all DOFs accurately at the same time; and possible in-accuracies in the applied Newman approximation for the second-order forcing.

The NAUTILUS FAST model is further compared to a frequency-domain simplified model, which includes constant added mass and parameterized actuator-disc aerodynamics. Results for two irregular sea states in terms of time series and power spectral density show very good agreement with the FAST model in surge, heave and pitch.

The report finalizes with a global summary.



Contents

1	Introduction	6
2	Ocean basin testing.....	7
3	State-of-the-art model of the OO-Star Wind Floater Semi 10MW	9
3.1	Design-driving load cases.....	9
3.2	Comparison to ocean basin tests.....	11
3.3	Comparison to a simplified frequency-domain model	22
3.4	Conclusions for the OO-Star Wind Floater Semi 10MW.....	39
4	State-of-the-art model of the NAUTILUS-DTU10	40
4.1	Design-driving load cases.....	40
4.2	Comparison to ocean wave tests.....	40
4.3	Comparison to a low-order model	57
4.4	Conclusions for the NAUTILUS-DTU10	61
5	Conclusions	63
6	References	65

1 Introduction

The present report makes out Deliverable D4.6 of the LIFES50+ project, 'Model validation against experiments and map of model accuracy across load cases'. The general scope of Work Package 4 (WP4) is the application of numerical models of varying fidelity throughout the design process.

Different numerical tools are required for different stages in the design of a floating offshore wind substructure. Simplified, low-order tools are useful to explore various design variations in the early stages, while state-of-the-art (SoA) models are employed to assess the final design under several environmental conditions. Further, high-fidelity numerical tools are often used for detailed analysis at the component level. The numerical tools can be benchmarked against physical tests and compared to each other. This is the aim of the present report which provides an assessment of the state-of-the-art and simplified numerical models developed within the LIFES50+ project.

The two public LIFES50+ concepts, namely the OO-Star Wind Floater Semi 10MW and the NAUTILUS-DTU10, were described in D4.2 [1]. State-of-the-art numerical models of these two public floating concepts were presented in D4.5 [2]. The design-driving load cases for each concept were identified in D7.7 [3]. In the present report, a summary of the design-driving load cases of D7.7 [3] is first provided. Next, the SoA models are benchmarked for wave-only conditions against the corresponding wave basin experimental results of D3.4 [4]. The ability of each model to reproduce the measured response is discussed, as well as the model calibration employed to achieve a good agreement between numerical and experimental results. Finally, the SoA models are used to evaluate the simplified numerical tools used in D4.1 [5]. The accuracy of the low-order models is mapped through different load cases, and the limitations in the simplified approach are identified and discussed.

For the OO-Star Wind Floater Semi 10MW, the design-driving load cases were identified in D7.7 [3] as DLC 1.2 (normal environment), 1.6 (severe sea state) and 6.1 (extreme environment). The same cases are the subject of the subsequent comparisons to model tests and simplified numerical models.

The OO-Star FAST model presented in D4.5 [2] is adapted to the test conditions and extended to include second-order hydrodynamics through Newman's approximation. The model is compared to test results of DLC 1.6 and 6.1, and the elements of a diagonal linear damping matrix are calibrated to match the standard deviation of the measured response for each sea state. For convenience, this calibration is carried out for simulations shorter than the duration of the tests. The results are presented in terms of time series, power-spectral density (PSD) and exceedance probability plots, as well as tables with mean, standard deviation and response level at the 95% percentile of the exceedance probability. The results show that this approach is viable and generally yields predictions within 10% error at the 95% percentile of the response's exceedance probability. We find that a better match may be possible if the damping calibration is carried out for simulations with the same duration as the tests, or if the full second-order solution is used instead of the Newman's approximation.

The OO-Star SoA model of D4.5 [2] with linear radiation-diffraction forcing is also used to benchmark a simplified frequency-domain model, which relies on precomputed aerodynamic loads and parameterized damping. The two models are compared for ten environmental conditions within DLC 1.2 in terms of time series, PSD, exceedance probability and damage-equivalent bending moment at the tower base. The tower-base moment is estimated by the frequency-domain model with errors up to 12% for wave-only and 7% for wind and waves, and CPU speeds around 1300 and 2700 faster than real time, respectively. The limitations observed are related to missing viscous hydrodynamic forcing, in-accuracies in the modelling of aerodynamic loads around rated wind speed and under-prediction of the tower response.



For the NAUTILUS-DTU10, the design-driving load cases identified in D7.7 [3] were also DLC 1.2 (normal environment), 1.6 (severe sea state) and 6.1 (extreme environment). The same cases are the subject of the subsequent comparisons to model tests and simplified numerical models.

The NAUTILUS FAST model of D4.5 [2] is adapted to the test conditions and extended to include second-order hydrodynamics through Newman's approximation. The approach to model viscous drag on the heave plates is modified. As a difference to the modelling of the OO floater, the damping is calibrated through adjustment of the drag coefficients of the different Morison elements. The dynamic mooring module MoorDyn is replaced by quasi-static mooring module MAP++. The model is compared to test results of DLC 1.6 and 6.1. The results are presented in terms of power spectral density and show that a good agreement in the wave range is obtained. While the calibration of the drag coefficients yields a good match in the slow-drift response in surge and sway for the pink noise test, the slow-drift response is generally under-predicted by the model.

The NAUTILUS FAST model is also compared to a simplified model, SLOW, which includes constant added mass and parameterized actuator-disc aerodynamics. Results for two irregular sea states in terms of time series and power spectral density show very good agreement with the FAST model in surge, heave and pitch.

2 Ocean basin testing

The test campaigns carried out at the SINTEF Ocean Basin Laboratory (see Figure 1) in 2017 and 2018, are extensively described in [4]. Froude scaling with a geometric scale factor of 1:36 was applied. The data are given in full scale unless stated otherwise. The lab-scale floating wind turbines (see Figure 2) consisted of a stiff floater and tower, connected by a flexible spring at the tower base designed to match the first coupled tower natural frequency for each concept. Following the hardware-in-the-loop (HIL) testing approach, the aerodynamic loads computed in real time by a numerical model were exerted on the tower top by a cable-driven parallel robot. The present report, however, focuses on the wave-only cases where the system of cables was not connected.

The instrumentation relevant to this report includes:

- Wave probes to measure free-surface elevation. A wave calibration phase took place before each floating structure was placed in the basin, in which the free-surface elevation was measured at three locations using conductance-type wave probes. One of the wave probes was placed at the location where the centre of the floating structure would later be. The raw time series of free-surface elevation measured by this wave probe were used as the input to the numerical models for each sea state. Another wave probe used in the calibration phase was kept during the tests. It was therefore possible to assess the wave repeatability between the calibration phase and the actual testing phase.
- Z-type force transducers to record mooring line tension. One device was located at the upper end (fairlead) of each mooring line. The pre-tension was measured once at the start of the test campaign. For each test, the force sensors were zeroed before the test and the pre-tension was added afterwards.
- A Qualisys motion capture system to track the floater motion in 6 degrees of freedom (DoFs). The system consisted of four reflective markers placed on the floater, and two infrared cameras located onshore. The motion signals were zeroed once at the start of the test campaign.

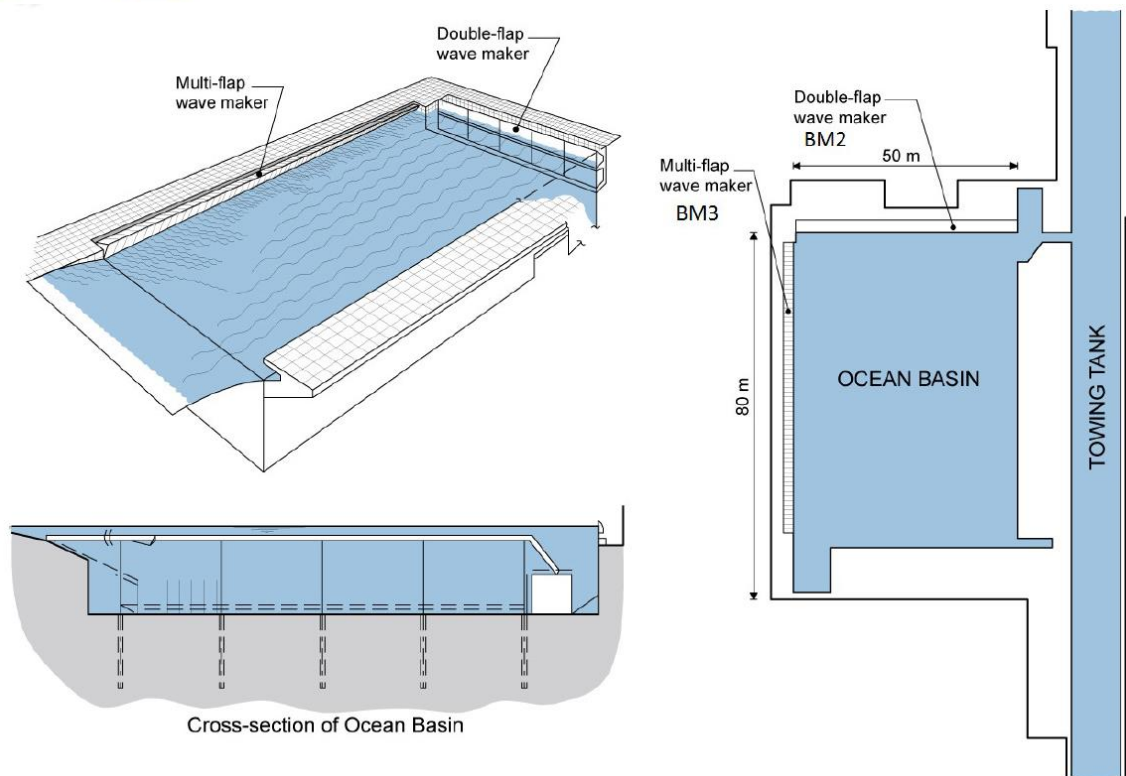


Figure 1: Ocean Basin facility at SINTEF Ocean

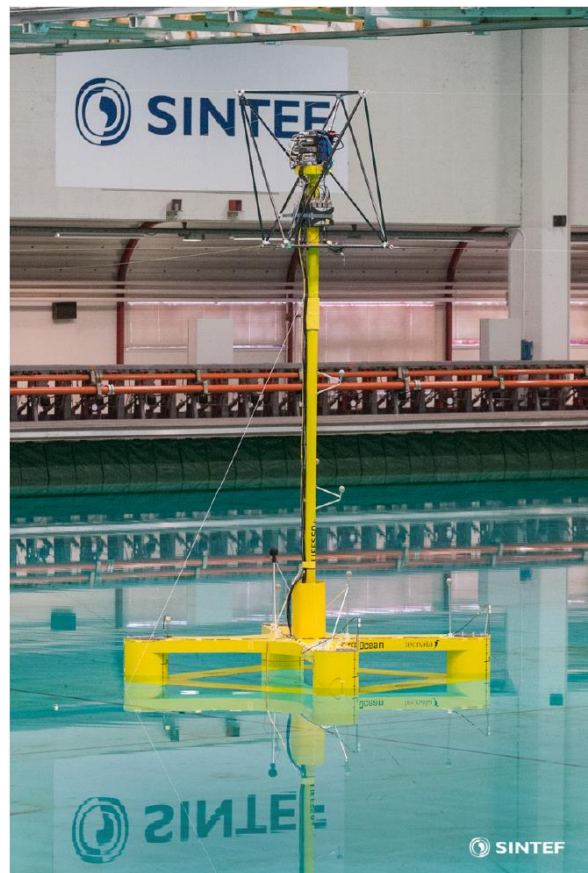


Figure 2: Physical model of the OO-Star Semi (left) and NAUTILUS-DTU10 (right)

3 State-of-the-art model of the OO-Star Wind Floater Semi 10MW

The SoA model [2] of the DTU 10MW Reference Wind Turbine [6] mounted on the OO-Star Wind Floater Semi 10MW [1] was implemented in FAST v8.16.00a-bjj [7] in full scale dimensions with active control and 15 DoFs for turbine and floater: first and second flapwise blade modal deflections, first edgewise blade modal deflection, drivetrain rotational flexibility, drivetrain speed, first and second fore-aft and side-side tower modal deflections, and floater surge, sway, heave, roll, pitch and yaw. The mooring loads, calculated by MoorDyn [8], included buoyancy, mass inertia and hydrodynamic loads resulting from the motion of the mooring lines in calm water. Hydrodynamic loads on the floater were first computed in WAMIT [9] and coupled to FAST through the Cummins equation [10]. Viscous effects were modelled internally by the Morison drag term. Further details on the modelling of floating wind turbines in FAST can be found in [11], while a thorough description of the FAST model used in this study is presented in [2] and [12].

3.1 Design-driving load cases

Part of the work performed in this deliverable and in LIFES50+ D7.7 [3] was to provide methodologies to support the designer in identifying critical design-driving load cases and the included environmental conditions. These methodologies were subsequently applied for the herein addressed models and key results are summarized in this section.

3.1.1 Identification of load driving cases and environmental conditions

As part of LIFES50+ efforts, in [13] a thorough ULS analysis was performed with FAST based on the LIFES50+ OO-Star Wind Floater Semi 10MW [1] with mounted DTU 10MW RWT and investigating all load cases defined in the LIFES50+ design basis (see, e.g. [14]).

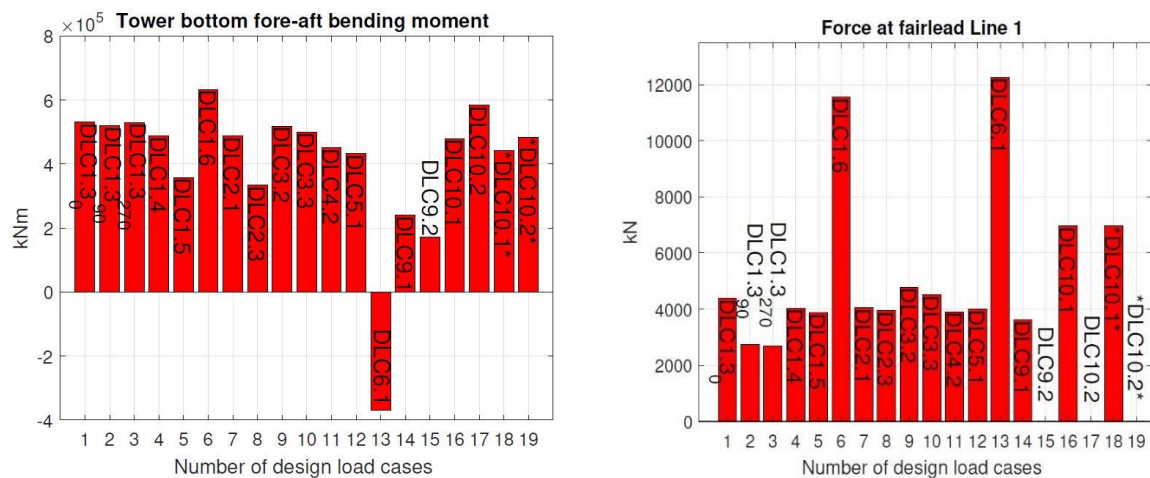


Figure 3: Tower bottom bending moment and fairlead 1 tension for ULS analysis, see [13].

Figure 3 summarizes the results of the performed ULS study. It is highlighted that, due to the limited availability of environmental data, the definition of DLC1.6 (ultimate loads during power production) is rather conservative. Overall, it was found that the controller may have a significant contribution, as it describes the trade-off between avoiding platform instabilities, loading and accelerations. Controller optimization for a given platform may reduce the loading for the power production significantly. The authors of [13] also note that the results of DLCs 10.1 and 10.2 may be influenced by some instabilities of the blade modeling, when misaligned inflow conditions are present. Nonetheless, mooring line failure remains one of the driving cases for the considered concept in that study. Due to the large number of concept and load case specific settings, such as controller design and timings of gusts, the results of the

ULS study are interpreted such that the evaluation of all load cases is required in order to identify the design driving load case for a given concept. However, based on overall experience and underlined by results from the ULS study, the load cases

- 1) DLC 1.2 – fatigue loads during power production (normal environment)
- 2) DLC 1.6 – ultimate loads during power production (severe sea states)
- 3) DLC 6.1 – ultimate loads during idling conditions (extreme environment)

are documented as providing a good overview on the overall performance of a system and may be used as initial indicator. For semisubmersibles in general, it was noted that they are inherently subject to large motions induced by the ocean environment and that maximum tower base and platform hull loading is to be expected for storm cases, such as DLC 6.1.

A second question is the definition of critical environmental conditions within the selected load cases. Typically, available standards require that conservative assumptions are taken into account, when simplifications with respect to the environment are performed (e.g. considering only one peak wave period rather than analyzing various combinations). For semisubmersibles in particular, periods are of high interest because the relation of wavelengths to platform dimensions, which is defined by the wave period may result in significant loading for the tower base (pitch motion) or mooring lines (heave motions). Identifying these critical environmental conditions may be done using so-called global sensitivity analysis [15]. By application of these tools, it was generally found that for DLC 1.2 and for the RNA loading, wind impact is dominant, for tower base loads, wind speed dominates for small wind speeds and wave loads for large wind speeds. It was found that concept specific wave periods may lead to increased loading which cannot be identified from potential flow analysis alone. For DLC 1.6 and for the RNA again the wind impact was dominating, for the tower base wind speed and wave periods showed the largest impact and for the fairlead tensions wave directionality and periods had the highest influence. Finally, for DLC 6.1 the ocean environment also had some impact on the RNA loading next to wind speed: the wave period as well as wind-wave-misalignment (largest loading for misalignments around 90°) were documented to have significant influence. This trend was also seen in the loadings of the tower base and the fairlead tension. Figure 4 shows exemplarily the scatterplots for visual evaluation of the impact of environmental variables on the fatigue loads on the tower base loading.

Load models of situations during normal sea states and power production to predict fatigue loads can be considered to be sufficiently accurate using state-of-the-art models. This is due to the fact that most loading situations are close to linear and also because the statistical property of interest (fatigue damage is closely related to the distribution of load cycles) is fairly robust towards outliers. This is not the case for ultimate load models, where the measure of interest is the peak or maximum load. As described in the previous paragraph, for both ULS DLCs 1.6 and 6.1 the wave environment (wave heights and wave periods) already showed considerable influence on the maximum loading based on potential flow & Morison elements for quadratic damping. This highlights the importance of investigating the accuracy of these simplified models during validation campaigns in the wave tank.

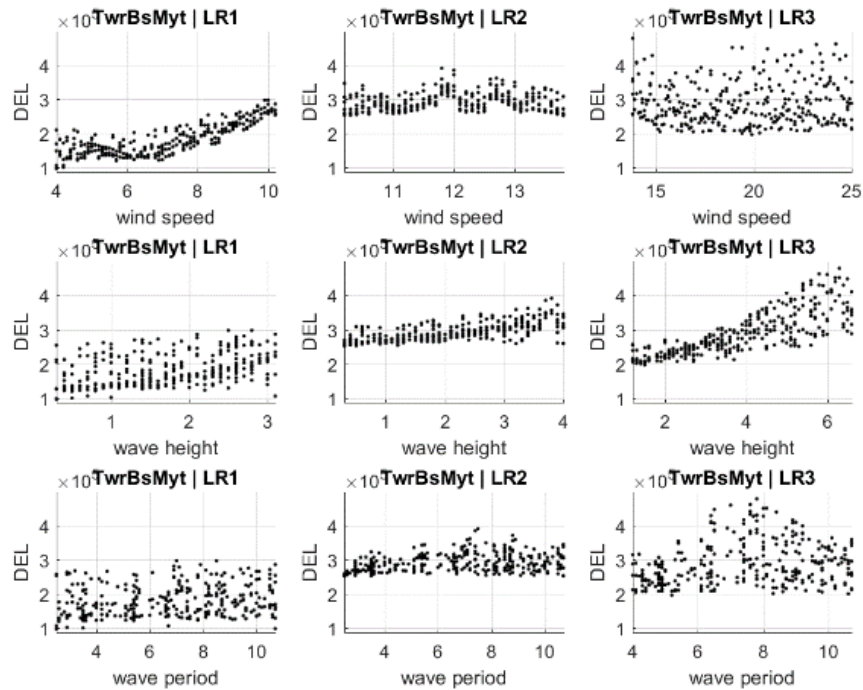


Figure 4: LIFES50 + OO-Star Wind Floater Semi 10MW scatterplots of results of simulation study considering variation of wind speed, wave height and wave period for three different load ranges.

3.2 Comparison to ocean basin tests

3.2.1 Model adaption

Minor changes were made to the FAST model of the OO-Star Wind Floater Semi 10MW in order to replicate the physical model used in the experiments:

- Since there was no overhang of the rotor nacelle assembly (RNA) present in the Real-Time Hybrid Model tests the downwind distance from the tower-top to the nacelle centre of mass was set to zero.
- The platform mass and inertias have been updated to match the values measured in the experiments, see [4].
- To avoid a minor offset in the heave response, the displaced volume in the model was adjusted slightly.
- Since waves-only tests were studied in this deliverable and no physical rotor was present in the tests, no effort was put into modelling the elastic properties of the tower and rotor.

A static equilibrium analysis was conducted to validate the mooring line tensions in the updated FAST model. Table 1 shows the pre-tensions in the model compared to measured values [4].

Table 1: Pretensions in the mooring lines for the OO-Star physical model and FAST model.

[kN]	Line 1	Line 2	Line 3
Experiments	1680	1680	1650
FAST	1663	1663	1663
Discrepancy	-1.0 %	-1.0 %	0.8 %

3.2.2 Approach for damping calibration

The free decay tests of the rigid body motion of the floating wind turbine were done by imposing an initial displacement to the structure and then allowing it to freely oscillate, in order to understand the system characteristics such as natural frequencies and the system damping. The six rigid body natural frequencies were identified based on natural periods of the decays as seen in Figure 5, and the results are listed in Table 2. Some discrepancies in the natural frequencies are observed, which are likely to originate from uncertainties in the model adaption (especially in the modelling of the system inertias and the mooring system).

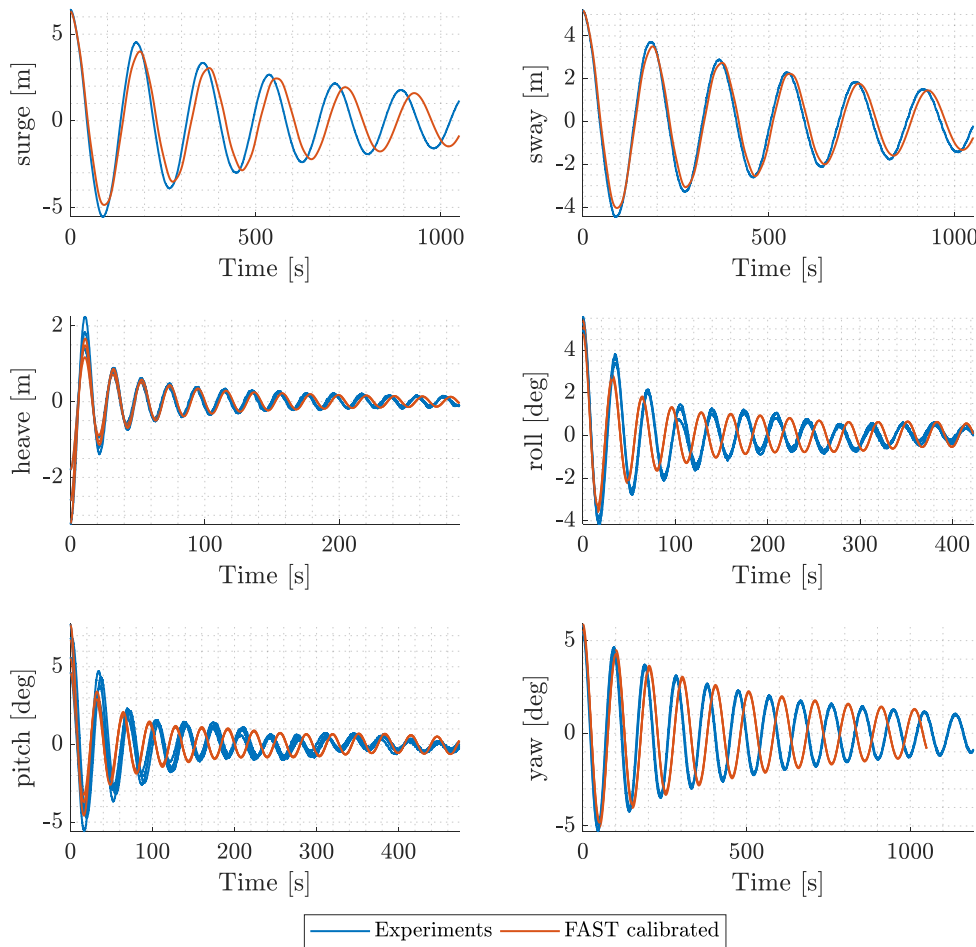


Figure 5: All six response decays, with heave, roll, pitch and yaw having multiple realisations.

Table 2: Measured and computed rigid body natural frequencies.

	Surge	Sway	Heave	Pitch	Roll	Yaw
	[Hz]	[Hz]	[Hz]	[Hz]	[Hz]	[Hz]
Experiments	0.0056	0.0055	0.0486	0.0291	0.0289	0.0105
FAST	0.0054	0.0054	0.0478	0.0314	0.0313	0.0099
Discrepancy	-4 %	-1 %	-2 %	8 %	8 %	-6 %

It should be noted that the heave, roll and yaw free decays were repeated three times with different initial displacements and pitch decay tests were repeated four times. This was done in the experiments as well as in the simulations. Data treatment of the experimental results included band pass filtering and drift removal.

In order to compare and thus calibrate the hydrodynamic damping of the numerical model, the linearized damping ratios were analysed as a function of displacement, as shown in Figure 6. The motion amplitude associated with a damping ratio is obtained by taking the mean of the two successive peak amplitudes used in determining that specific data point, thus labelled ‘average cycle amplitude’. The equivalent linear damping ratio ζ was calculated using:

$$\zeta = \frac{1}{\sqrt{1 + \left(\frac{2\pi}{\delta}\right)^2}} \quad (3.1)$$

where δ is the logarithmic decrement and was calculated for any two successive peaks.

The methodology for calibrating the damping in the numerical model (used in, for example, Borg et al. [16]) was to add a global linear damping matrix, \mathbf{B}_1^* , and a quadratic damping matrix, \mathbf{B}_2^* , to the equations of motion of the floater, see Equation (3.2). \mathbf{B}_1^* and \mathbf{B}_2^* were set to zero in the initial (uncalibrated) model where the only sources of damping were the wave radiation damping and the drag computed by the Morison equation. In the HydroDyn-module of FAST the user can specify the elements of these global damping matrices.

$$(\mathbf{M} + \mathbf{A}_\infty)\ddot{\xi} + \int_0^t \mathbf{K}(t - \tau) \dot{\xi}(\tau) d\tau + \mathbf{B}_1^* \dot{\xi} + \mathbf{B}_2^* |\dot{\xi}| \dot{\xi} + \mathbf{C} \xi = F_{exc} + F_{moor} + F_{visc} \quad (3.2)$$

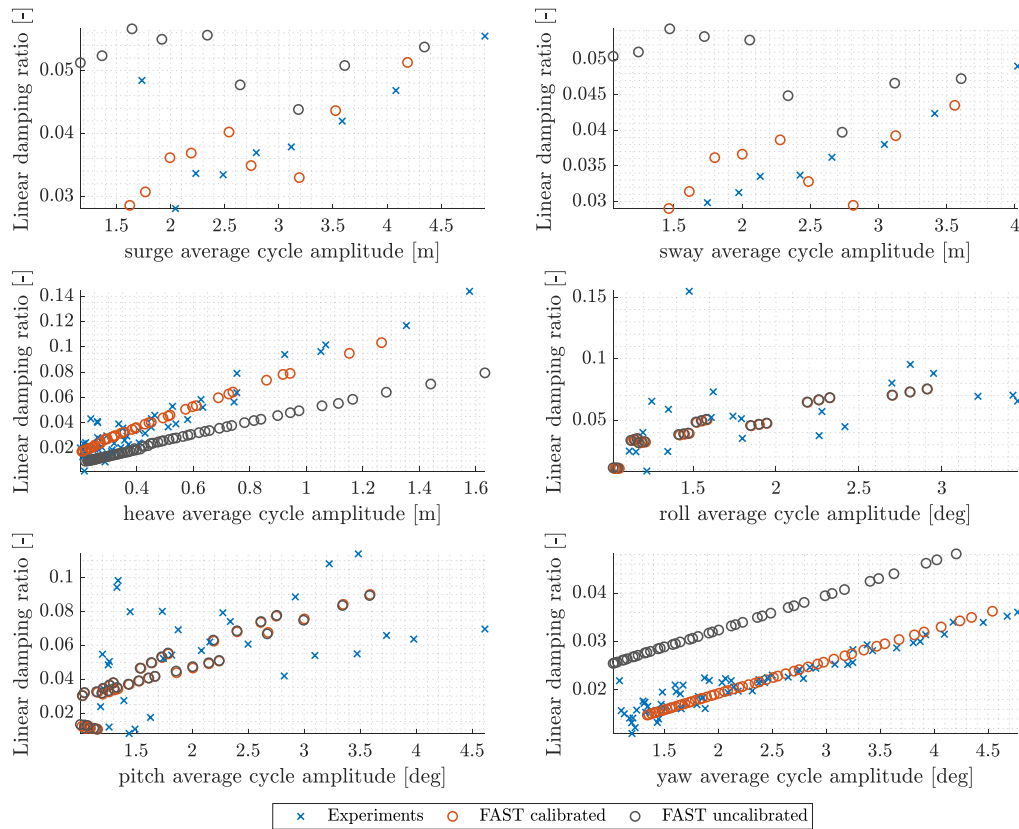
where $\xi = [\xi_1, \xi_2, \dots, \xi_6]^T$ correspond to the system six degrees of freedom; surge, sway, heave, roll, pitch and yaw. \mathbf{M} illustrates the mass and inertia matrix of the combined system, \mathbf{A}_∞ is the resulting infinite-frequency limit of the added mass matrix, $\mathbf{K}(t) = \frac{2}{\pi} \int_0^\infty \mathbf{B}_{rad}(\omega) \cos(\omega t) d\omega$ in the convolution integral denotes the retardation kernel (based on radiation damping \mathbf{B}_{rad} only), and \mathbf{C} the hydrostatic stiffness matrix.

The forces acting on the combined system are the wave excitation loads F_{exc} , the mooring reactions F_{moor} and the viscous effects F_{visc} .

The \mathbf{B}_1^* and \mathbf{B}_2^* denotes a constant linear and a quadratic global damping matrix respectively. In this case only elements along the main diagonals of \mathbf{B}_1^* and \mathbf{B}_2^* were added and tuned, hence the off-diagonal elements were zero. The values along the main diagonals were obtained iteratively through trial and error and the results can be seen in Figure 6 with the final values listed in Table 3. As is apparent from the figure, the nature of hydrodynamic damping is not linear. The linear damping matrix \mathbf{B}_1^* contributes a constant level of damping, independent on amplitude. The experimental results show that this linear damping description is not sufficient. The addition of the quadratic damping through \mathbf{B}_2^* contributes to increased damping for increased amplitude. The results for surge, sway and heave demonstrates a good match after calibration of \mathbf{B}_2^* .

Table 3: Additional linear and quadratic hydrodynamic viscous damping for the OO-Star Wind Floater

Linear	1 (Surge)	2 (Sway)	3 (Heave)	4 (Roll)	5 (Pitch)	6 (Yaw)
1 (Surge)	-1.2E+05	0	0	0	0	0
2 (Sway)	0	-1.1E+05	0	0	0	0
3 (Heave)	0	0	5.0E+04	0	0	0
4 (Roll)	0	0	0	0	0	0
5 (Pitch)	0	0	0	0	0	0
6 (Yaw)	0	0	0	0	0	-5.0E+07
Quadratic						
1 (Surge)	1.0E+06	0	0	0	0	0
2 (Sway)	0	1.0E+06	0	0	0	0
3 (Heave)	0	0	5.0E+06	0	0	0
4 (Roll)	0	0	0	0	0	0
5 (Pitch)	0	0	0	0	0	0
6 (Yaw)	0	0	0	0	0	-2.0E+09


Figure 6: Variation of linear damping ratio in each degree of freedom for the OO-Star Wind Floater

3.2.3 Results

In the following the calibrated FAST model of the OO-Star Wind Floater will be tested in different wave conditions and compared to the ocean wave tests. For the analysis, the initial value in each time series has been subtracted, since the motion signals were not zeroed between tests.

The study is based on the planar version (motion in surge, heave and pitch) of the ocean basin load cases in D3.4 [4] where only waves are applied. For each sea state, the response in each of the planar DoFs (surge, heave and pitch) is shown in terms of a representative portion of the time series (left column), a Power Spectral Density (PSD) plot (central column) and an exceedance probability plot (right column). To avoid initial transient effects the first 1800 s were discarded from both the PSD and the exceedance probability calculations. Each response plot is followed by a table comparing test and model response in each planar DoF in terms of the mean $\bar{\xi}$, standard deviation σ and value at the 95% percentile $\xi^{95\%}$. The relative error in σ and $\xi^{95\%}$ is also shown.

3.2.3.1 Pink Noise – $H_s = 2$ m, $T_p = [4.5, 18.2]$ s

Figure 7 below shows the planar response to pink noise waves with $H_s = 2$ m and $T_p = [4.5, 18.2]$ s. The study was conducted with FAST applying the additional linear and quadratic hydrodynamic viscous damping in Table 3. First, the first-order wave forcing was used, but by comparing the responses to the tests it was clear that the contribution from the sub-harmonics was crucial especially for the surge motion, as seen in the figure. For this reason second-order forcing was included in terms of the Newman approximation. A comparison of the Newman approximation and the full Quadratic Transfer Function (QTF) will be presented in D4.8.

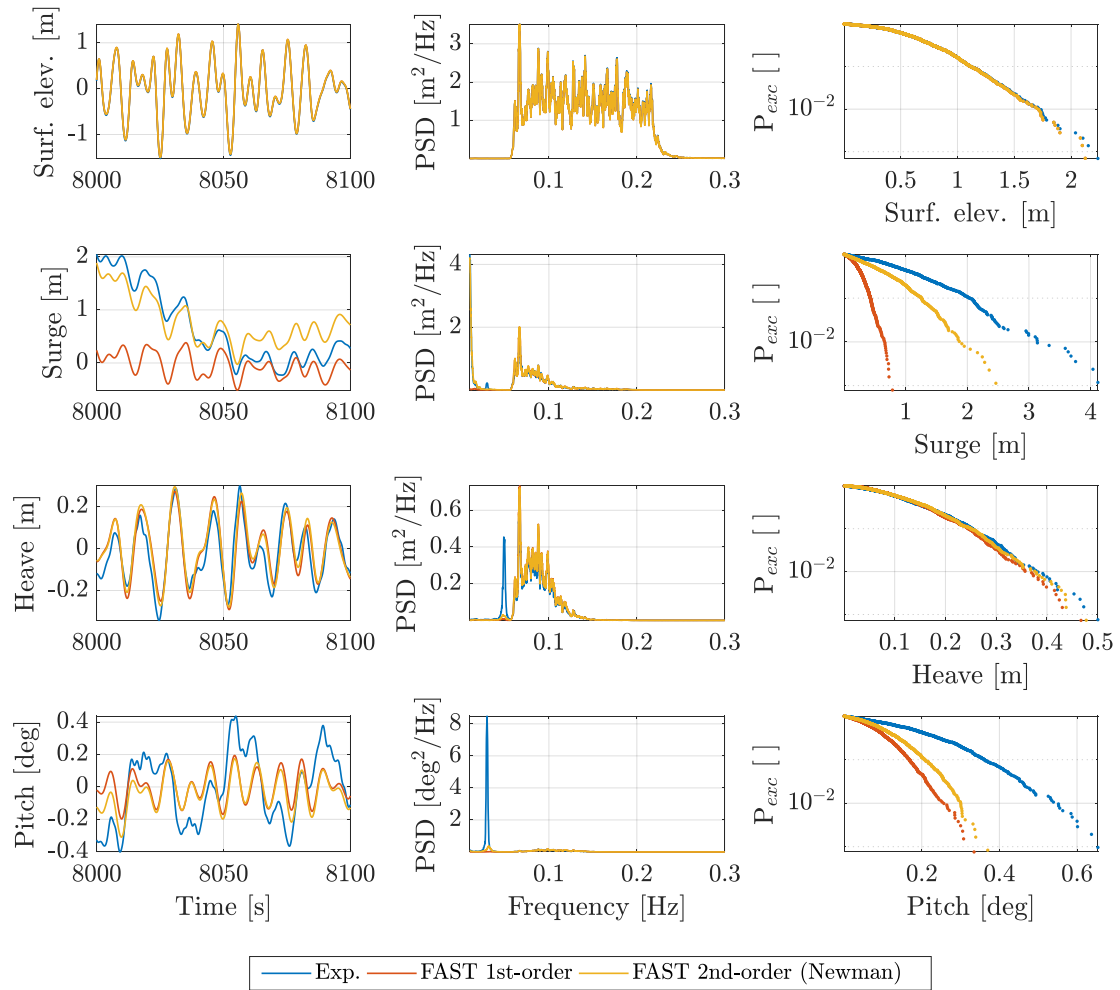


Figure 7: Time, frequency and exceedance probability plots for the pink noise waves – baseline

Figure 7 also shows that the FAST model is significantly damped in surge and pitch compared to the experiments, even when applying the 2nd-order wave forcing. For this reason, it was decided to re-calibrate the additional linear damping terms for surge, heave and pitch in \mathbf{B}_1^* and their sea state dependence investigated. These dependencies have also been investigated in for example [17], [18], [19] and [20]. The Morison drag term introduces both forcing and damping. By increasing the drag coefficients not only the damping increases, but also the excitation. For that reason, it was chosen only to adjust the additional linear damping terms through \mathbf{B}_1^* .

This was done for the pink noise waves and the three load cases: DLC 1.6, 6.1 (1) and 6.1 (2). The additional linear damping terms for each sea state were further calibrated by matching the standard deviation of the responses for the model and the experiments. Due to the long duration of the tests, it was decided to do the calibrations based on shorter versions of the load cases, i.e. 1000 s (without transient). A better match is likely obtained for longer simulations.

Figure 8 shows how the planar damping terms changes with significant wave height. The negative damping is compensating for the missing wave excitation forces, which increases with H_s .

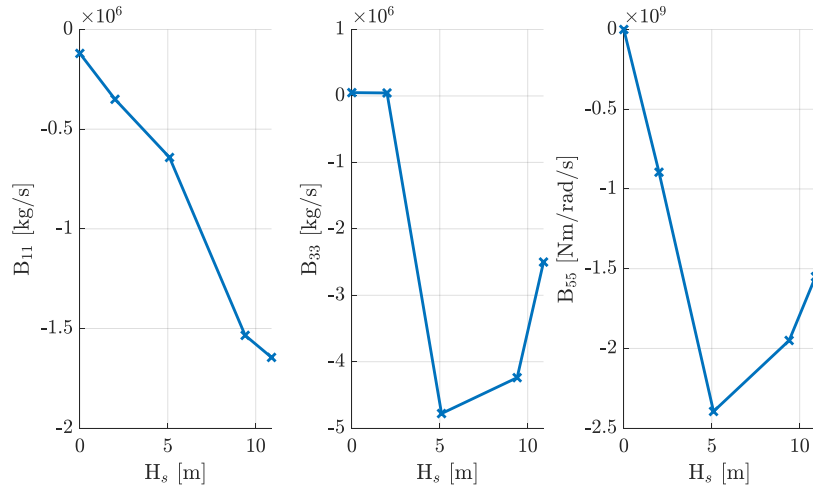


Figure 8: Global calibrated linear damping diagonals for different sea states.

The fine-calibrated additional linear damping terms was used to re-simulate the pink noise waves again and the results for $H_s = 2$ m, $T_p = [4.5, 18.2]$ s are shown in Figure 9. Comparing this to Figure 7, the surge and pitch are now matching the experiments much better. This can also be emphasised when looking at the corresponding results statistics, see Table 4, where the errors are within 13% in the 95% percentile.

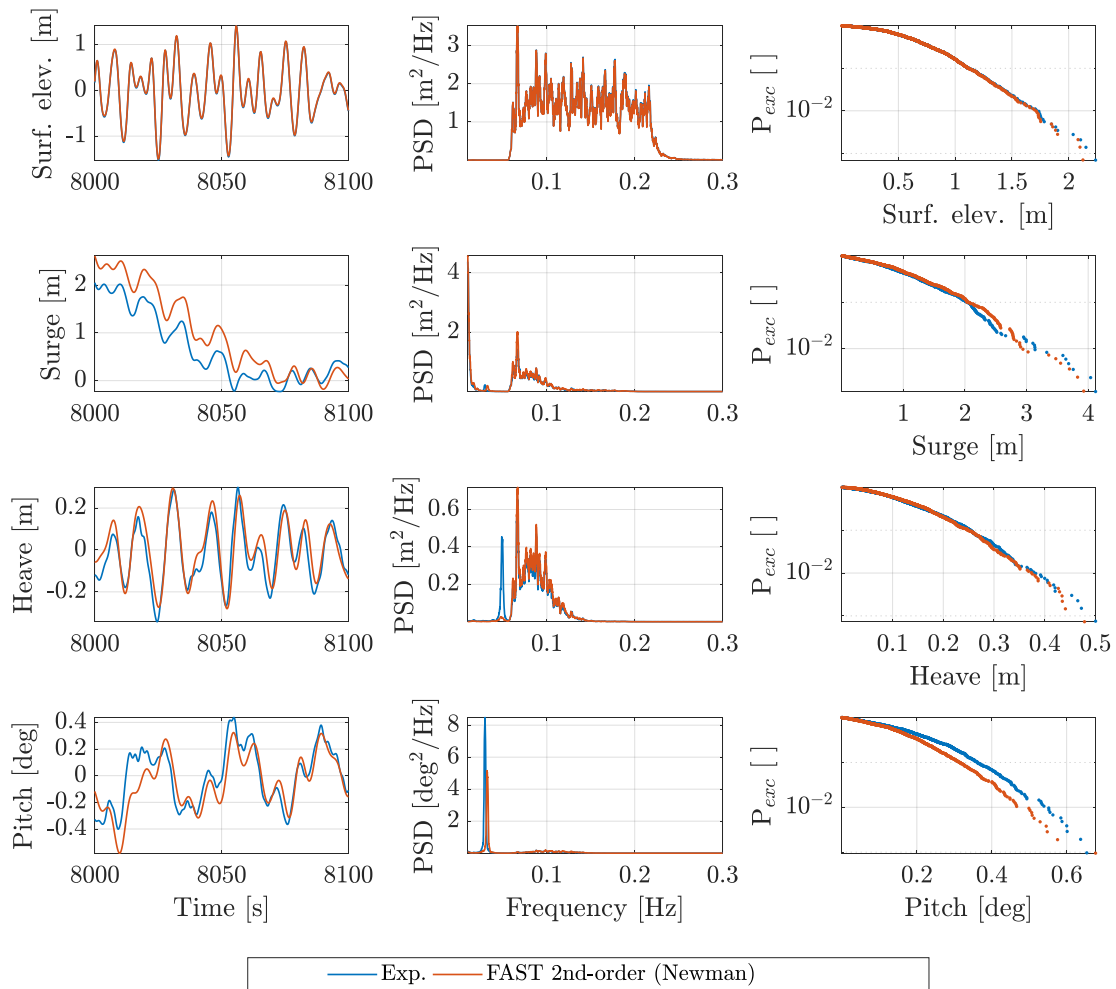


Figure 9: Time, frequency and exceedance probability plots for pink noise waves – fine-calibrated

Table 4: Results statistics for pink noise waves after fine-tuning of the global linear damping matrix

	$\bar{\xi}_{test}$	$\bar{\xi}_{model}$	σ_{test}	σ_{model}	Error [%]	$\xi_{test}^{95\%}$	$\xi_{model}^{95\%}$	Error [%]
Surge [m]	0.77	0.72	1.13	1.19	4.94	2.27	2.44	7.20
Heave [m]	-0.02	0.00	0.13	0.12	-0.58	0.30	0.29	-3.11
Pitch [deg]	-0.02	-0.04	0.19	0.17	-11.64	0.42	0.37	-12.77

3.2.3.2 DLC 1.6 – $H_s = 10.9$ m, $T_p = 15$ s

In Figure 10 the planar response to irregular waves are shown for DLC 1.6 with $H_s = 10.9$ m, $T_p = 15$ s (severe sea states). Corresponding result statistics are presented in Table 5.

A good match of the 95% percentile for all three responses are obtained as they are all within 10% of the test results. However, beyond the 95% percentile the values for surge starts to deviate, as it can be seen on the exceedance probability curves. Also, a significant error in the standard deviation of the surge response of -14.20% can be seen, implying that the additional linear damping term for the surge motion in \mathbf{B}_1^* needs some fine-adjustment. Even though the response of the pitch motion is matched well, it is seen from the PSD, that some low frequency response at the pitch natural frequency is missing for the simulated response. In the time series, for the particular window shown, a difference in phase is observed for the wave frequency range. It was checked that this is not a general tendency for the full time series.

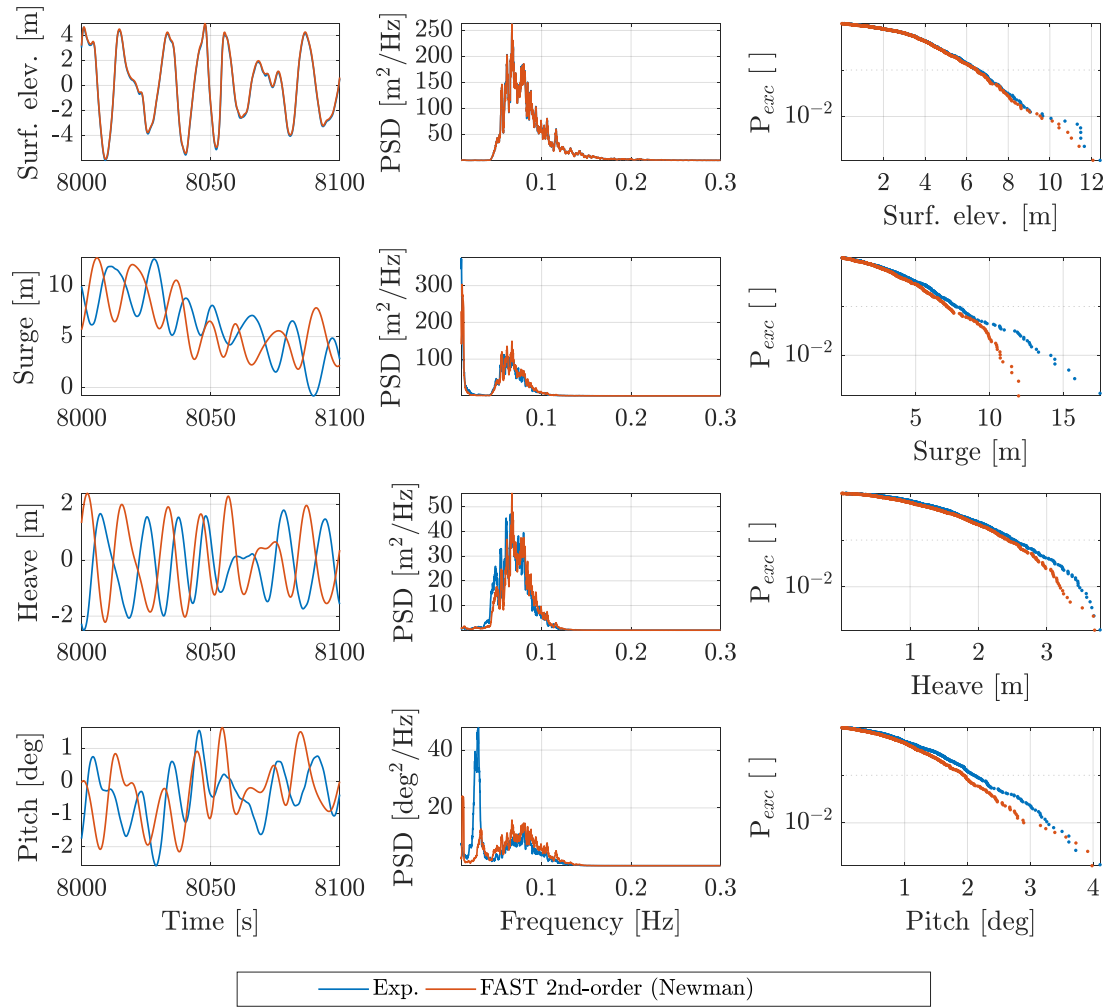


Figure 10: Time, frequency and exceedance probability plots for DLC 1.6

Table 5: Results statistics for DLC 1.6

	$\bar{\xi}_{test}$	$\bar{\xi}_{model}$	σ_{test}	σ_{model}	Error [%]	$\xi_{test}^{95\%}$	$\xi_{model}^{95\%}$	Error [%]
Surge [m]	5.28	6.03	4.15	3.56	-14.20	9.44	8.97	-4.99
Heave [m]	-0.20	0.12	1.18	1.15	-3.14	2.89	2.79	-3.61
Pitch [deg]	-0.19	-0.27	0.98	0.91	-6.48	2.50	2.26	-9.40

3.2.3.3 DLC 6.1 (1) – $H_s = 5.1$ m, $T_p = 9$ s

The planar response to irregular waves is shown in Figure 11 for DLC 6.1 with $H_s = 5.1$ m, $T_p = 9$ s (extreme environment). Corresponding result statistics are presented in Table 6.

It is observed that the errors are within 13% in the 95% percentile, but around that point the FAST model starts to under-predict the heave response. The deviation in the maximum values for the heave response is approximately 1 m. It can also be seen from the time series of the pitch response that some sub-harmonics are not captured in the FAST model resulting in a significant error in the standard deviation of -13.5% even though the deviation in the 95% percentile is only -7.7%.

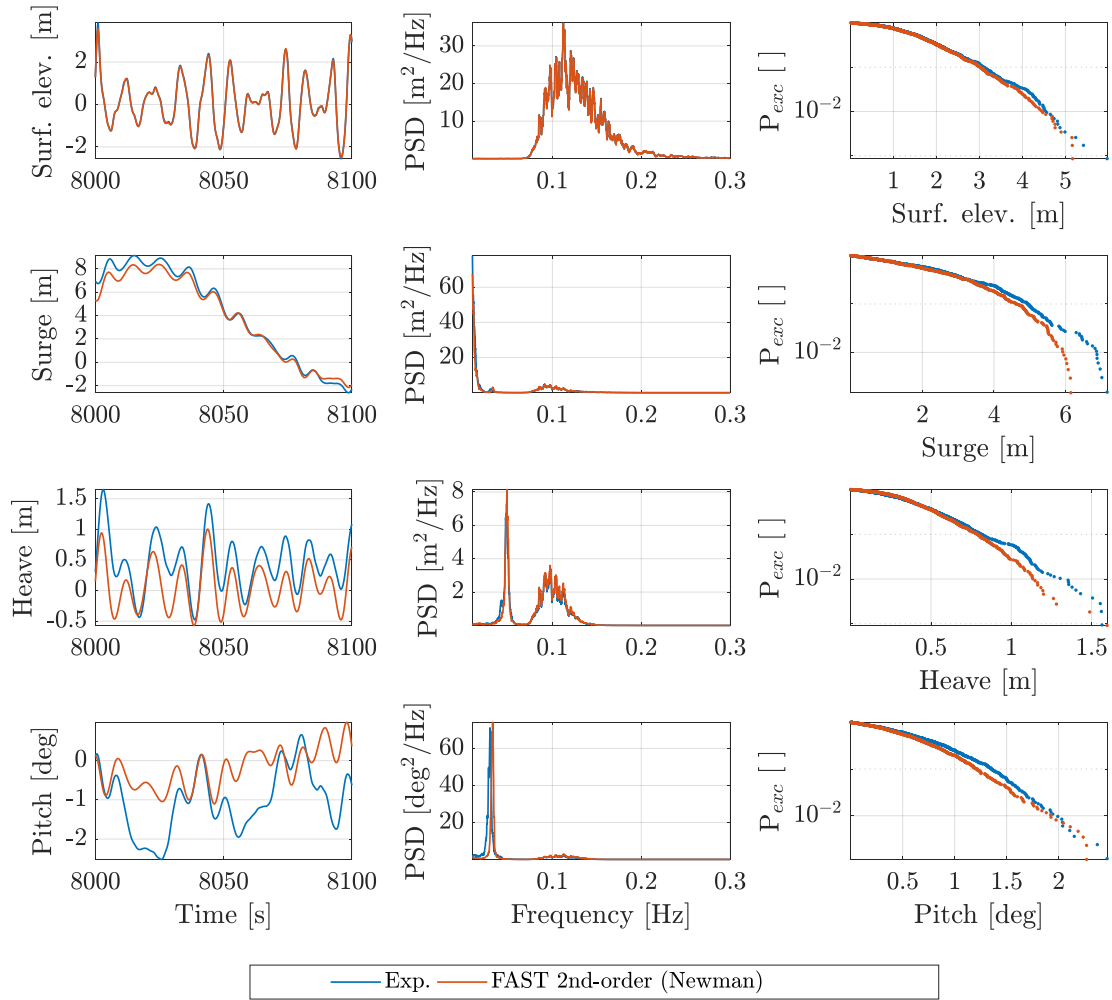


Figure 11: Time, frequency and exceedance probability plots for DLC 6.1 (1)

Table 6: Results statistics for DLC 6.1 (1)

	$\bar{\xi}_{test}$	$\bar{\xi}_{model}$	σ_{test}	σ_{model}	Error [%]	$\xi_{test}^{95\%}$	$\xi_{model}^{95\%}$	Error [%]
Surge [m]	3.66	3.33	2.89	2.71	-6.10	5.46	5.13	-6.01
Heave [m]	0.29	0.05	0.38	0.36	-4.73	1.04	0.91	-12.22
Pitch [deg]	-0.70	-0.18	0.72	0.63	-13.48	1.55	1.43	-7.69

3.2.3.4 DLC 6.1 (2) – $H_s = 9.4$ m, $T_p = 16$ s

The planar response to irregular waves is shown in Figure 12 for DLC 6.1 with $H_s = 9.4$ m, $T_p = 16$ s. Corresponding result statistics are presented in Table 7.

It is observed that the errors are within 5% in the 95% percentile and the errors in the standard deviations are within 8%. Even though some of the excitations at the pitch natural frequency are not captured, see the pitch PSD, the overall response is matched very well.

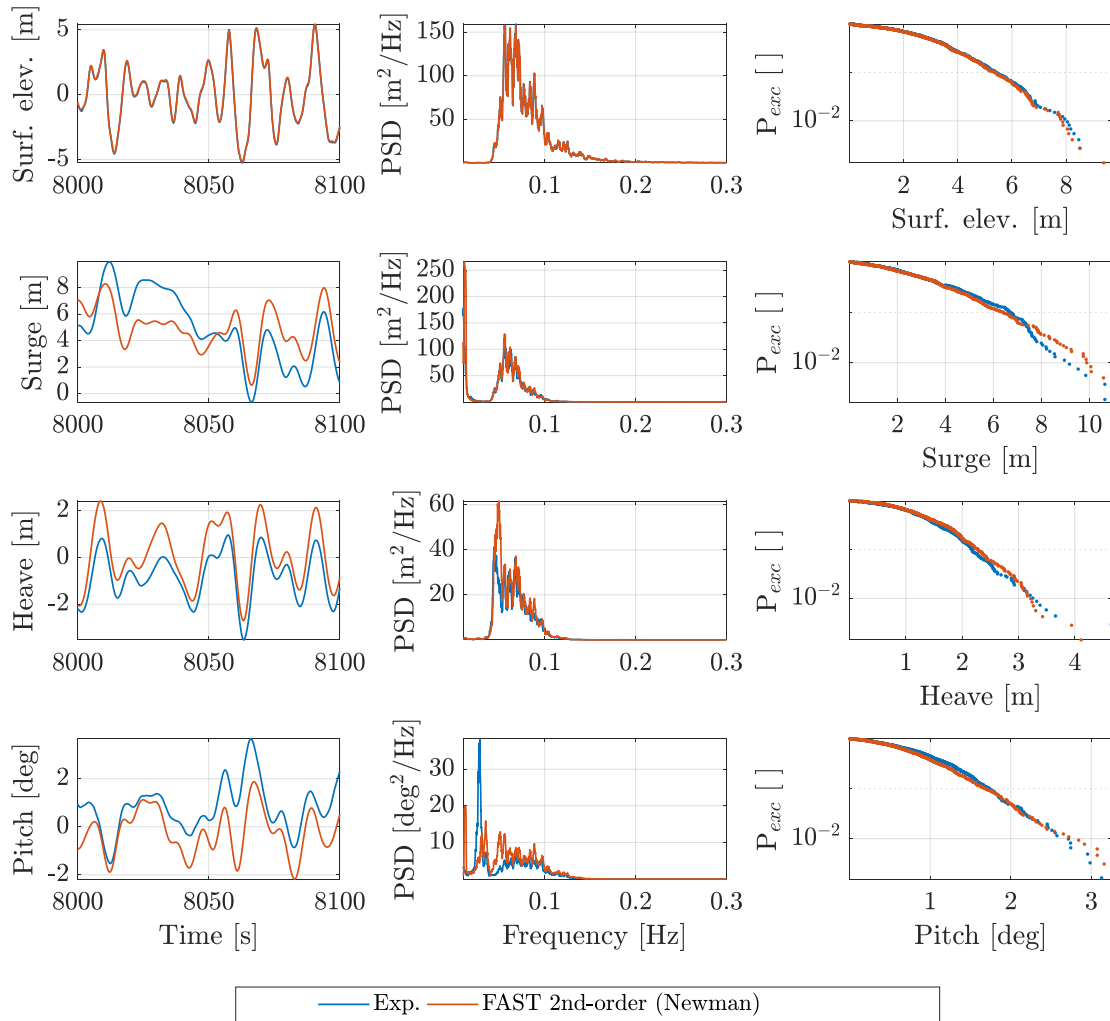


Figure 12: Time, frequency and exceedance probability plots for DLC 6.1 (2)

Table 7: Results statistics for DLC 6.1 (2)

	$\bar{\xi}_{test}$	$\bar{\xi}_{model}$	σ_{test}	σ_{model}	Error [%]	$\xi_{test}^{95\%}$	$\xi_{model}^{95\%}$	Error [%]
Surge [m]	2.57	4.77	3.28	3.21	-2.31	7.45	7.77	4.40
Heave [m]	-0.56	0.06	1.08	1.17	7.62	2.50	2.62	4.79
Pitch [deg]	0.68	-0.19	0.82	0.81	-1.17	1.97	2.00	1.91

3.2.4 Conclusions

It is apparent from the comparison study that the tuning of the global linear and quadratic damping matrix in the FAST model only against physical decay tests is not sufficient when waves are applied. It was seen that linear planar damping terms are depending on sea state and that significant high negative damping values were needed to replicate the experiments, which is compensating for the incomplete modelling of the wave excitation forces.

The FAST model was successfully fine-tuned for each load case and the results showed errors within 13% in the 95% percentile, with most cases under 8%. Response-wise the best matched load case was DLC 6.1 with $H_s = 9.4$ m, $T_p = 16$ with errors within 5% in the 95% percentile and within 8% in the standard deviation. A comparison of the present Newman based 2nd-order forcing method to the full-QTF based forcing will be presented in D4.8.

3.3 Comparison to a simplified frequency-domain model¹

3.3.1 Introduction

This study uses QuLAF [21] (**Quick Load Analysis of Floating wind turbines**), a frequency-domain code that captures the four dominant degrees of freedom (DoFs) in the in-plane global motion: floater surge, heave and pitch, and tower first fore-aft modal deflection. The model, which is here adapted to the DTU 10MW Reference Wind Turbine (RWT) [6] mounted on the OO-Star Wind Floater Semi 10MW [1], was set up through cascading techniques. In the cascading process, information is precomputed or extracted from more advanced models (*parent* models) to enhance the simplified models (*children* models). In this case, the hydrodynamic loads are extracted from the radiation-diffraction, potential-flow solver WAMIT [9]. The aerodynamic loads and aerodynamic damping coefficients are precomputed in the numerical tool FAST v8 [7], and the mooring module MoorDyn [8] is employed to extract a mooring stiffness matrix for different operating positions. This way, the model includes standard radiation-diffraction theory and realistic rotor loads through precomputed aeroelastic simulations. In the model, the system response is obtained by solving the linear equations of motion (EoM) in the frequency domain, leading to a very efficient tool. While the radiation-diffraction results allow a full linear response evaluation for rigid structure motion in waves, the ambition of this model is to extend them with the flexible tower and realistic stochastic rotor loads, thus going one step further than other simplified models in the literature. The results from QuLAF are here benchmarked against its time-domain, state-of-the-art (SoA) *parent* model in terms of time series, power spectral density (PSD), exceedance probability and fatigue damage-equivalent load (DEL).

3.3.2 The frequency-domain, cascaded numerical model

QuLAF represents the floating wind turbine as two lumped masses — floater and rotor-nacelle assembly — connected by a flexible tower. The model captures four planar DoFs — floater surge, heave, pitch and first tower fore-aft modal deflection — and is thus applicable to aligned wind and wave situations. The floating wind turbine is represented as depicted in Figure 13.

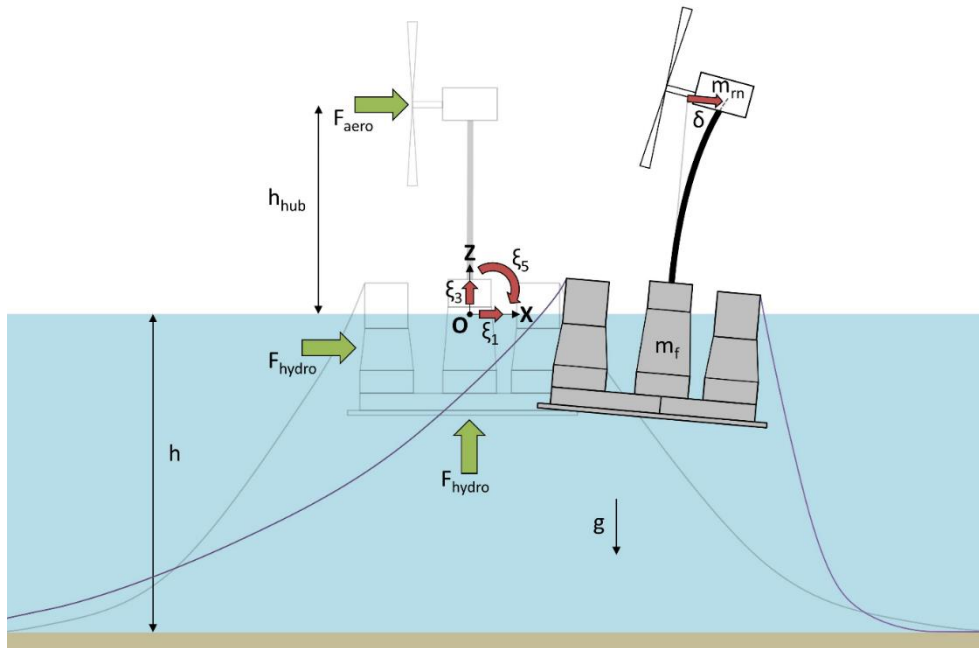


Figure 13: Sketch of the floating wind turbine as seen by the QuLAF model.

¹ This section is an extract of Pegalajar-Jurado et al. [21]. For further details please refer to the original paper.

The equation of motion is given by

$$[-\omega^2(\mathbf{M} + \mathbf{A}(\omega)) + i\omega\mathbf{B}(\omega) + \mathbf{C}]\hat{\xi}(\omega) = \hat{\mathbf{F}}(\omega) \rightarrow \hat{\xi}(\omega) = \mathbf{H}(\omega)\hat{\mathbf{F}}(\omega), \quad (3.3)$$

where:

- \mathbf{M} is the symmetric matrix of structural mass and inertia, obtained by looking at the forces needed to produce unit accelerations in the different DoFs.
- $\mathbf{A}(\omega)$ is the frequency-dependent, hydrodynamic added mass and inertia matrix, reduced by removing the rows and columns corresponding to the DoFs not included in the simplified model (sway, roll, yaw). A row and column of zeros is added for compatibility with the tower DoF.
- $\mathbf{B}(\omega)$ is the frequency-dependent global damping matrix that includes contributions from the hydrodynamic radiation damping $\mathbf{B}_{rad}(\omega)$, the hydrodynamic viscous damping \mathbf{B}_{vis} (see Section 3.3.2.2.1), the aerodynamic damping $\mathbf{B}_{aero}(\omega)$ (see Section 3.3.2.2.2) and the tower structural damping \mathbf{B}_{struc} .
- \mathbf{C} is the restoring matrix, which includes hydrostatic stiffness \mathbf{C}_{hst} , structural stiffness \mathbf{C}_{struc} and mooring stiffness \mathbf{C}_{moor} (see Section 3.3.2.2.3).
- The dynamic response vector $\hat{\xi}(\omega)$ has one element for each DoF: floater surge $\hat{\xi}_1(\omega)$, heave $\hat{\xi}_3(\omega)$, pitch $\hat{\xi}_5(\omega)$ and first tower fore-aft modal deflection $\hat{\alpha}(\omega)$. The sign convention is that shown in Figure 13. The physical tower deflection at any height z can be obtained by multiplying the mode shape $\phi(z)$ and the modal deflection $\alpha(t)$. The tower deflection at the hub height h_{hub} is therefore given by $\delta(t) = \phi_{hub}\alpha(t)$. If the absolute nacelle displacement is sought, the contributions from floater surge and pitch motions must be added to the tower deflection, thus the global response vector $\hat{\xi}_{glob}(\omega)$ is found by introducing a transformation matrix, $\hat{\xi}_{glob}(\omega) = \mathbf{T}_{glob}\hat{\xi}(\omega)$.
- The dynamic load vector $\hat{\mathbf{F}}(\omega)$ contains hydrodynamic loads $\hat{\mathbf{F}}_{hydro}(\omega)$ and aerodynamic loads $\hat{\mathbf{F}}_{aero}(\omega)$. Hydrodynamic loads are extracted from the solution to the diffraction problem. The only viscous effect considered in the model is viscous damping (see Section 3.3.2.2.1), but viscous forcing is neglected to keep the model computationally efficient. The time-domain aerodynamic loads for each mean wind speed W are precomputed in the SoA model, as detailed in Section 3.3.2.2.2.
- The static part of the response, ξ_{st} , is added to the dynamic part $\hat{\xi}(\omega)$ when it is converted from the frequency to the time domain via inverse fast Fourier transform (iFFT). The static loads applied include the static part of the aerodynamic loads $\mathbf{F}_{aero,st}$, the gravity loads \mathbf{F}_{grav} and the buoyancy loads \mathbf{F}_{buoy} .

3.3.2.1 System natural frequencies

The vector of natural frequencies ω_0 is found by solving the undamped eigenvalue problem given by

$$[-\omega_0^2(\mathbf{M} + \mathbf{A}(\omega_0)) + \mathbf{C}]\hat{\xi}(\omega_0) = 0 \rightarrow \omega_0^2\hat{\xi}(\omega_0) = (\mathbf{M} + \mathbf{A}(\omega_0))^{-1}\mathbf{C}\hat{\xi}(\omega_0). \quad (3.4)$$

Since the matrix of added mass depends on frequency, the eigenvalue problem is solved in a frequency loop. For each frequency ω , the four possible natural frequencies are computed. When one of the four possible frequencies obtained is equal to the frequency of that particular iteration in the loop, a system natural frequency has been found. The system natural frequencies computed in QuLAF are compared to those obtained with the SoA model in Section 3.3.3.1.



3.3.2.2 Cascading techniques applied to the simplified model

One disadvantage of frequency-domain models is their inability to directly capture loads that depend on the response in a nonlinear way. Some relevant examples are viscous drag, aerodynamic loads and catenary mooring loads. This section gives a description of the cascading methods employed to incorporate such nonlinear loads into the simplified model.

3.3.2.2.1 Hydrodynamic viscous loads

Viscous effects on submerged bodies depend nonlinearly on the relative velocity between the wave particles and the structure, hence they can only be directly incorporated in time-domain models. In the offshore community this is normally done through the drag term of the Morison equation [22], which provides the transversal drag force dF on a cylindrical member section of diameter D and length dl as

$$dF = \frac{1}{2} \rho C_D D |v_f - v_s| (v_f - v_s) dl, \quad (3.5)$$

where ρ is the fluid density, C_D is a drag coefficient, and v_f and v_s are the local fluid and structure velocities perpendicular to the member axis. The equation can be also written as

$$dF = \frac{1}{2} \rho C_D D \operatorname{sgn}(v_f - v_s) (v_f - v_s)^2 dl = \frac{1}{2} \rho C_D D \operatorname{sgn}(v_f - v_s) (v_f^2 + v_s^2 - 2v_f v_s) dl, \quad (3.6)$$

which shows that the drag effects can be separated into a pure forcing term, a nonlinear damping term and a linear damping term. Since the hydrodynamics on the given floating substructure are inertia-dominated and under the assumption of small displacements around the equilibrium position, the two first terms are neglected and only the linear damping term is retained in the QuLAF model. Invoking further the assumption of small displacements and velocities relative to the fluid velocity, we have $\operatorname{sgn}(v_f - v_s) \approx \operatorname{sgn}(v_f)$. With this assumption the linear damping term of the viscous force becomes

$$dF_l = \frac{1}{2} \rho C_D D \operatorname{sgn}(v_f - v_s) (-2v_f v_s) dl \approx -\rho C_D D |v_f| v_s dl. \quad (3.7)$$

A symmetric viscous damping matrix \mathbf{B}_{vis} is now derived by applying Eqn. (3.7) to the different DoFs. For the surge motion, integration over the submerged body gives the total viscous force in the x direction as

$$F_1 = - \int_{z_{min}}^0 \rho C_D D |u| \dot{\xi}_1 dz, \quad (3.8)$$

where z_{min} is the structure's deepest submerged point, u is the horizontal wave particle velocity and $\dot{\xi}_1$ is the surge velocity. The integral in Eqn. (3.8) requires the estimation of drag coefficients and the computation of wave kinematics at several locations on the submerged structure, which can be involved for complex geometries. These computations would reduce the CPU efficiency relative to the radiation-diffraction terms, so instead the local drag coefficient and wave velocity inside the integral are replaced by global, representative values outside the integral, C_{Dx} and u_{rep} . Hereby the force becomes

$$F_1 = -\rho \dot{\xi}_1 \int_{z_{min}}^0 C_D D |u| dz \approx -\rho C_{Dx} u_{rep} \dot{\xi}_1 \int_{z_{min}}^0 D dz = -\rho C_{Dx} A_x u_{rep} \dot{\xi}_1 \equiv -b_{11} \dot{\xi}_1, \quad (3.9)$$



where A_x is the integral of the local diameter D over depth, or the floater's area projected on the yz plane. This defines the surge-surge element of the viscous damping matrix \mathbf{B}_{vis} . Further the b_{51} element of the matrix is obtained by consideration of the moment from F_1 around the point of flotation,

$$\tau_1 = -\rho \dot{\xi}_1 \int_{z_{min}}^0 C_D D |u| z dz \approx -\rho C_{Dx} u_{rep} \dot{\xi}_1 \int_{z_{min}}^0 D z dz = -\rho C_{Dx} S_{y,Ax} u_{rep} \dot{\xi}_1 \equiv -b_{51} \dot{\xi}_1, \quad (3.10)$$

where $S_{y,Ax}$ is the first moment of area of A_x about the y axis (negative due to $z \leq 0$) and b_{51} is the surge-pitch element of the viscous damping matrix. In a similar way, the heave-heave and heave-pitch coefficients of \mathbf{B}_{vis} are obtained by applying Eqn. (3.7) to the heave motion,

$$F_3 = -\rho \dot{\xi}_3 \int_{x_{min}}^{x_{max}} C_D D |w| dx \approx -\rho C_{Dz} w_{rep} \dot{\xi}_3 \int_{x_{min}}^{x_{max}} D dx = -\rho C_{Dz} A_z w_{rep} \dot{\xi}_3 \equiv -b_{33} \dot{\xi}_3, \quad (3.11)$$

$$\tau_3 = \rho \dot{\xi}_3 \int_{x_{min}}^{x_{max}} C_D D |w| x dx \approx \rho C_{Dz} w_{rep} \dot{\xi}_3 \int_{x_{min}}^{x_{max}} D x dx = \rho C_{Dz} S_{y,Az} w_{rep} \dot{\xi}_3 \equiv -b_{53} \dot{\xi}_3. \quad (3.12)$$

Here $\dot{\xi}_3$ is the heave velocity, w is the wave particle vertical velocity, A_z is the floater's bottom area projected on the xy plane and $S_{y,Az}$ is the first moment of area of A_z about the y axis, which is zero for the present floating substructure due to symmetry. Finally, by applying Eqn. (3.7) to the pitch motion, the pitch-pitch element of the viscous damping matrix, b_{55} , is found. When the floater pitches with a velocity $\dot{\xi}_5$ an arbitrary point on the floater with coordinates (x, z) moves with a velocity $(z\dot{\xi}_5, -x\dot{\xi}_5)$. The motion creates a moment due to viscous effects given by

$$\begin{aligned} \tau_5 &= -\rho \dot{\xi}_5 \int_{z_{min}}^0 C_D D |u| z^2 dz - \rho \dot{\xi}_5 \int_{x_{min}}^{x_{max}} C_D D |w| x^2 dx \\ &\approx -\rho (C_{Dx} I_{y,Ax} u_{rep} + C_{Dz} I_{y,Az} w_{rep}) \dot{\xi}_5 \equiv -b_{55} \dot{\xi}_5, \end{aligned} \quad (3.13)$$

where $I_{y,Ax}$ and $I_{y,Az}$ are the second moments of area of A_x and A_z about the y axis, respectively. The complete symmetric matrix of viscous damping is therefore

$$\mathbf{B}_{vis} = \begin{bmatrix} \rho C_{Dx} A_x u_{rep} & 0 & \rho C_{Dx} S_{y,Ax} u_{rep} & 0 \\ & \rho C_{Dz} A_z w_{rep} & 0 & 0 \\ & & \rho (C_{Dx} I_{y,Ax} u_{rep} + C_{Dz} I_{y,Az} w_{rep}) & 0 \\ & & & 0 \end{bmatrix}. \quad (3.14)$$

The global drag coefficients above have been chosen generically as $C_{Dx} = 1$ and $C_{Dz} = 2$, given that the bottom slab of the floater under consideration has sharp corners and is expected to oppose a greater resistance to the flow than the smooth vertical columns. To obtain the representative velocity u_{rep} , the time- and depth-dependent horizontal wave velocity at the floater's centreline $u(0, z, t)$ is first averaged over depth and then over time,

$$u_{avg}(t) = \frac{1}{|z_{min}|} \int_{z_{min}}^0 u(0, z, t) dz \equiv \frac{1}{|z_{min}|} \Re \left\{ \text{iFFT} \left(\frac{\omega \hat{\eta}(\omega)}{k} \left(1 - \frac{\sinh(k(z_{min} + h))}{\sinh(kh)} \right) \right) \right\}, \quad (3.15)$$

$$u_{rep} = |u_{avg}|.$$

Here k is the wave number for the angular frequency ω and h is the water depth. The representative velocity w_{rep} is chosen as the time average of the vertical wave velocity at the centre of the bottom plate,

$$w_{avg}(t) = w(0, z_{min}, t), \quad w_{rep} = \overline{|w_{avg}|}. \quad (3.16)$$

This simplification of the wave kinematics history, although drastic, allows the characterization of the viscous damping for each sea state and avoids the need to compute wave kinematics locally and integrate the drag loads.

3.3.2.2.2 Aerodynamic loads

Aerodynamic loads depend on the square of the relative wind speed seen by the blades. The relative wind speed includes contributions from the rotor speed, the blade deflection, the tower deflection, and the motion of the floater. The fact that the aerodynamic thrust depends on the blade relative velocity produces the well-known aerodynamic damping. State-of-the-art numerical models incorporate aerodynamic loads based on relative velocity, because both the wind speed and the blade structural velocity are known at each time step. However, this cannot be done in a frequency-domain model. In the approach implemented in QuLAF, the aerodynamic loads considering the motion of the blades are simplified and approximated by loads considering a fixed hub with rigid blades and linear damping terms. The time series of fixed-hub loads and the aerodynamic damping coefficients are extracted from the SoA model for each mean wind speed.

The aerodynamic loads are obtained at each wind speed W by a SoA simulation with turbulent wind and no waves where all DoFs except shaft rotation and blade pitch are disabled and where the wind turbine controller is enabled. The time series of fixed-hub, pure aerodynamic loads are extracted from the results and stored in a data file which is loaded into the model. Hence, these SoA simulations need to be as long as the maximum simulation time needed in the simplified model (5400 s in this case). These loads include $F_{aero,1}(t)$, $F_{aero,3}(t)$ (horizontal and vertical components of the aerodynamic loads on the rotor, respectively) and $\tau_{aero}(t)$ (tilt torque on the rotor). The vector of aerodynamic loads in the frequency domain is thus

$$\hat{\mathbf{F}}_{aero}(\omega) = \begin{bmatrix} \hat{F}_{aero,1}(\omega) \\ \hat{F}_{aero,3}(\omega) \\ \hat{F}_{aero,1}(\omega)h_{hub} + \hat{\tau}_{aero}(\omega) \\ \hat{F}_{aero,1}(\omega)\phi_{hub} + \hat{\tau}_{aero}(\omega)\phi_{z,hub} \end{bmatrix}. \quad (3.17)$$

Here the fourth element of $\hat{\mathbf{F}}_{aero}$ represents the effect of the aerodynamic loads on the tower modal deflection, hence the mode shape deflection ϕ_{hub} and its slope $\phi_{z,hub}$ evaluated at the hub are involved.

For a given rotor, the work carried out by the aerodynamic damping is a function of wind speed, rotational speed, turbulence intensity, motion frequency and oscillation amplitude. Here, we define an equivalent linear damping which delivers the same work over one oscillation cycle and can be extracted from a decay test. Schl er et al. [23] used this principle for the tower fore-aft mode of a bottom-fixed offshore turbine and found that the damping was only slightly dependent on the motion amplitude. We make a further simplification and carry out the decay tests in steady wind. Since the mass and stiffness of floater and tower only affect the aerodynamic damping through the motion frequency, we transfer the damping coefficients b from the decay tests in FAST to the QuLAF model. On the contrary, if the damping ratio ζ was transferred, changes in mass or stiffness properties would imply a change in the

aerodynamic forcing, which is not physically correct. With the transfer of damping coefficients b , recalculation of the decay tests is only necessary in the event that the change of natural frequencies should affect the damping values significantly. Here, the decay tests from which aerodynamic damping ratios were extracted were carried out at representative natural frequencies equal to those of the present floater. These decay tests in calm water and with the wind turbine controller active were carried out for each DoF with all the other DoFs locked. This way, the floating wind turbine was a one-DoF spring-mass-damper system in each case, where the horizontal position of the hub x_{hub} was of interest. The decay tests were carried out as a step test in steady wind where the wind speed goes from the minimum to the maximum value with step changes every 600 s. With every step change of wind speed, the structure moves to a new equilibrium position. If all sources of hydrodynamic and structural damping are disabled, the aerodynamic damping is the only responsible for the decay of the hub motion, and it can be extracted from the time series of x_{hub} . The n peaks extracted from the signal are used in pairs to estimate each local logarithmic decrement d_i , and from it, a local damping ratio ζ_i , which is then averaged to obtain the aerodynamic damping ratio ζ_{aero} for the given DoF and W :

$$d_i = \log \frac{x_{hub,i}}{x_{hub,i+1}} \rightarrow \zeta_i = \frac{d_i}{\sqrt{4\pi^2 + d_i^2}} \rightarrow \zeta_{aero} = \frac{1}{n-1} \sum_{i=1}^{n-1} \zeta_i. \quad (3.18)$$

Figure 14 shows examples of $x_{hub}(t)$ and selected peaks for surge, pitch and clamped tower DoFs for a wind speed of 13 m/s. The wind changed from 12 m/s to 13 m/s at $t = 0$, and the mean of the signals has been subtracted. For surge and pitch, peaks within the first 40 s are neglected to allow the unsteady aerodynamic effects to disappear. For the tower DoF, however, the frequency is much higher and the signal has died out by the time the aerodynamics are steady. For that reason, the tower decay peaks are extracted after 300 s, and a sudden impulse in wind speed is introduced at $t = 300$ s to excite the tower. This method was chosen since the standard version of FAST does not allow an instantaneous force to be applied.

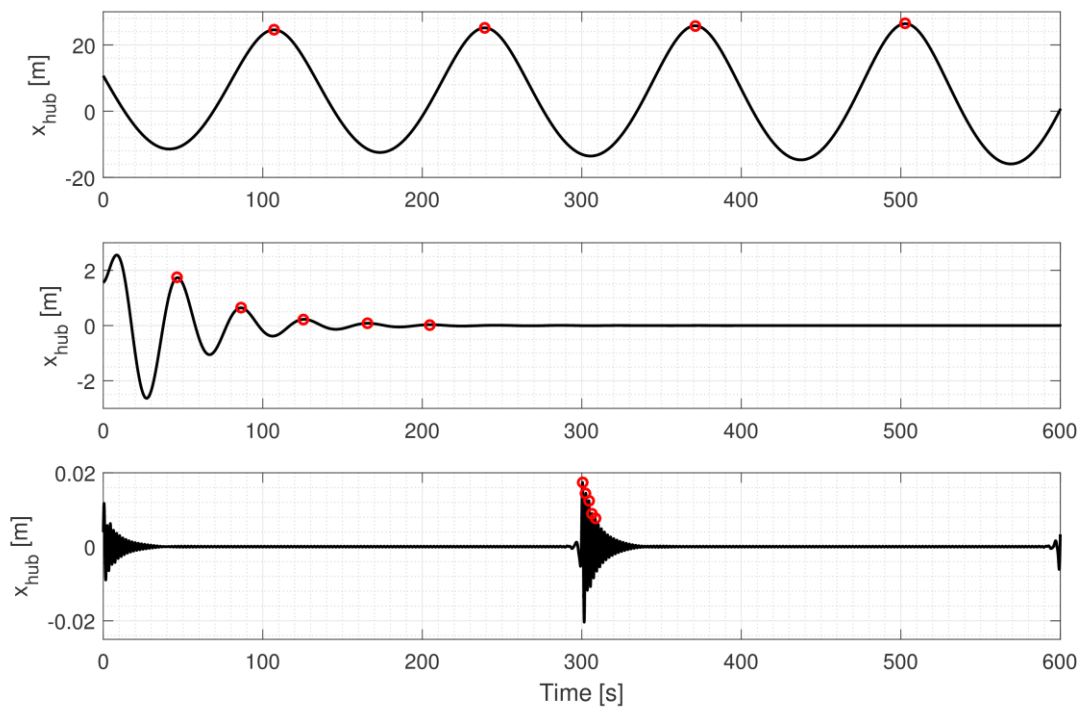


Figure 14: Example of time series of hub position and selected peaks for the extraction of aerodynamic damping. From top to bottom: surge, pitch and clamped tower degrees of freedom.

In Figure 15 the aerodynamic damping ratio is shown for all DoFs as a function of W . It is observed that the aerodynamic damping in surge is negative for wind speeds between 11.4 m/s and 16 m/s, due to the wind turbine controller. However, in real environmental conditions with wind and waves, it has been observed that the hydrodynamic damping contributes to a positive global damping of the surge motion. This controller effect is similar to the "negative damping problem" reported in, for example, Larsen and Hanson [24] or Jonkman [25]. The negative aerodynamic damping in surge may be eliminated if one tunes the controller natural frequency so it lies sufficiently below the surge natural frequency of the floating wind turbine, as it was done in [24] for the floater pitch motion. This solution, however, would make the controller too slow and would affect power production, thus it was not adopted here because the global damping in surge has been observed to be positive when all other damping contributions are taken into account.

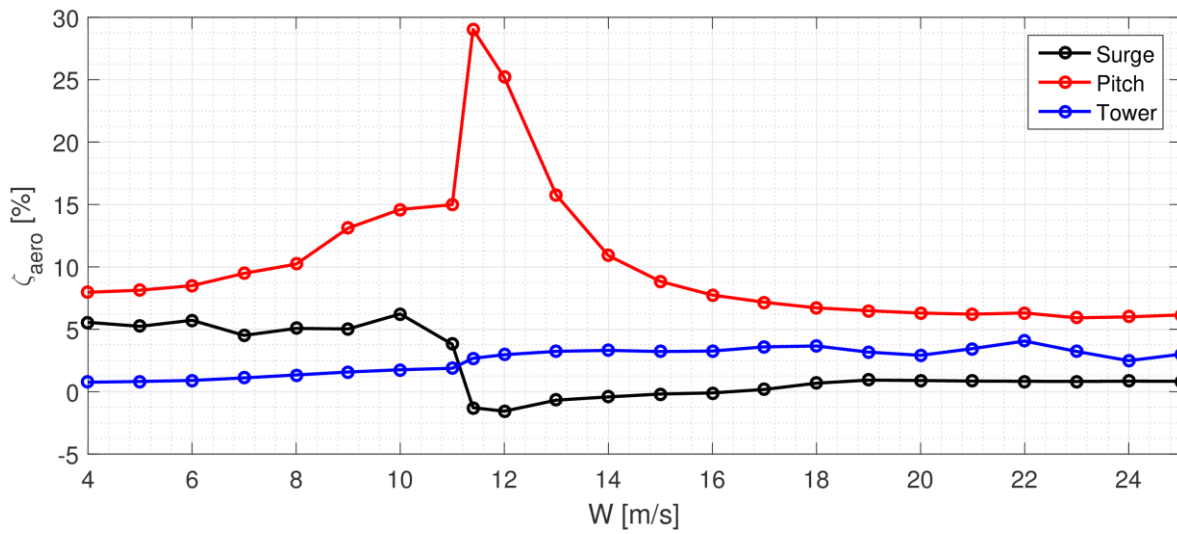


Figure 15: Aerodynamic damping ratios for different degrees of freedom as a function of wind speed.

The damping ratio for the i^{th} DoF and each wind speed, $\zeta_{aero,i}(W)$, is next converted to a damping coefficient by

$$b_{aero,i}(W) = 2\zeta_{aero,i}(W)\sqrt{C_{ii}(M_{ii} + A_{ii}(\omega))}, \quad (3.19)$$

where C_{ii} , M_{ii} and $A_{ii}(\omega)$ are taken from the one-DoF oscillator in the corresponding decay test. The table of aerodynamic damping coefficients as a function of wind speed $b_{aero}(W)$ is stored in a data file, which is loaded into the model. Since the aerodynamic damping coefficients are extracted from simulations with steady wind, but applied in the model in simulations with turbulent wind, an averaging is applied to account for the variability of the wind speed in turbulent conditions. Given the time series of wind speed at hub height $V(t)$, the probability density function (PDF) of a normal distribution given by $\mathcal{N}(\bar{V}, \sigma_V)$ is used to estimate the probability of occurrence within $V(t)$ of each discrete value of W . Then the aerodynamic coefficient for the given turbulent wind conditions and the i^{th} DoF is

$$b_{aero,i} = \sum_{j=1}^{N_W} PDF(W_j) b_{aero,i}(W_j). \quad (3.20)$$

The diagonal matrix of aerodynamic damping is thus built as



$$\mathbf{B}_{aero}(\omega) = \begin{bmatrix} b_{aero,11}(\omega) & 0 & 0 & 0 \\ & 0 & 0 & 0 \\ & & b_{aero,55}(\omega) & 0 \\ & & & b_{aero,tow} \end{bmatrix}. \quad (3.21)$$

3.3.2.2.3 Mooring loads

The equations that provide the loads on a catenary cable depend nonlinearly on the fairlead position. In dynamic mooring models the drag forces on the mooring cables are also included, therefore the mooring loads also depend on the square of the relative velocity seen by the lines. These nonlinear effects can easily be captured by time-domain models, but cannot be directly accommodated in a linear frequency-domain model. In QuLAF, the mooring system is represented by a linearized stiffness matrix for each wind speed, which is extracted from the SoA model and where hydrodynamic loads on the mooring lines are neglected. The dependence of the mooring matrix on wind speed is necessary because different mean wind speeds generally produce different mean thrust forces, which displace the floating wind turbine to different equilibrium states. The stiffness of the mooring system is different at each equilibrium position because of the nonlinear force-displacement behaviour of the catenary lines.

For each wind speed a first SoA simulation is needed with steady uniform wind and no waves, where only the tower fore-aft and floater surge, heave and pitch DoFs are enabled. After some time the floating wind turbine settles at its equilibrium position $(\xi_{eq,1}, \xi_{eq,3}, \xi_{eq,5})$, which is stored. These simulations should be just long enough so that the equilibrium state is reached (600 s in this case). Then, a new short SoA simulation with all DoFs disabled is run, where the floater initial position is the equilibrium with a small positive perturbation in surge, $(\xi_{eq,1} + \Delta\xi_1, \xi_{eq,3}, \xi_{eq,5})$. This simulation should be just long enough for the mooring lines to settle at rest (120 s in this case). The global mooring forces in surge and heave and the global mooring moment in pitch are stored, namely $(F_{moor,1}^{\xi1+}, F_{moor,3}^{\xi1+}, \tau_{moor,5}^{\xi1+})$. The process is repeated now with a negative perturbation in surge $(\xi_{eq,1} - \Delta\xi_1, \xi_{eq,3}, \xi_{eq,5})$, giving $(F_{moor,1}^{\xi1-}, F_{moor,3}^{\xi1-}, \tau_{moor,5}^{\xi1-})$. All this information is enough to compute the first column of the mooring matrix \mathbf{C}_{moor} for the wind speed W . Perturbations in heave $\pm\Delta\xi_3$ and pitch $\pm\Delta\xi_5$ provide the necessary information to compute the rest of the columns, and therefore the full matrix:

$$\mathbf{C}_{moor}(W) = - \begin{bmatrix} \frac{F_{moor,1}^{\xi1+} - F_{moor,1}^{\xi1-}}{2\Delta\xi_1} & \frac{F_{moor,1}^{\xi3+} - F_{moor,1}^{\xi3-}}{2\Delta\xi_3} & \frac{F_{moor,1}^{\xi5+} - F_{moor,1}^{\xi5-}}{2\Delta\xi_5} & 0 \\ \frac{F_{moor,3}^{\xi1+} - F_{moor,3}^{\xi1-}}{2\Delta\xi_1} & \frac{F_{moor,3}^{\xi3+} - F_{moor,3}^{\xi3-}}{2\Delta\xi_3} & \frac{F_{moor,3}^{\xi5+} - F_{moor,3}^{\xi5-}}{2\Delta\xi_5} & 0 \\ \frac{\tau_{moor,5}^{\xi1+} - \tau_{moor,5}^{\xi1-}}{2\Delta\xi_1} & \frac{\tau_{moor,5}^{\xi3+} - \tau_{moor,5}^{\xi3-}}{2\Delta\xi_3} & \frac{\tau_{moor,5}^{\xi5+} - \tau_{moor,5}^{\xi5-}}{2\Delta\xi_5} & 0 \\ 0 & 0 & 0 & 0 \end{bmatrix} \quad (3.22)$$

3.3.2.3 Estimation of extreme responses: a spectral approach

Classical Monte-Carlo analysis of response to stochastic loads entails running a simulation, extracting the peaks from the response time series, sorting them in ascending order and assigning an exceedance probability to each peak based on their position in the sorted list. Several simulations of the same environmental conditions with different random seeds provide a family of curves in the exceedance probability plot, which can be used to estimate the expected response level for a given exceedance

probability. We note that the extracted exceedance probability curves are based on the assumption that the peaks are independent, which may not always be the case. Yet, in this section the linear nature of the simplified model will be further exploited to obtain an estimation of the extreme responses to wave loads by solely using the wave spectrum and the system transfer function, thus eliminating the need of a response time series and the bias introduced by a particular random seed. An extension of the method to wind and wave forcing is further presented and discussed.

In a Gaussian, narrow-banded process, the peaks follow a Rayleigh distribution. In linear stochastic sea states, the free-surface elevation $\eta(t)$ is a Gaussian random variable R_η with zero mean. Thus, within the narrow-banded assumption, which often applies to good approximation, the crest heights follow a Rayleigh distribution [26] given by

$$P(R_\eta > \eta) = e^{-\frac{1}{2}\left(\frac{\eta}{\sigma_\eta}\right)^2}, \quad (3.23)$$

where the variance of $\eta(t)$ is σ_η^2 , which can be obtained from the integral of the wave spectrum,

$$\sigma_\eta^2 = \int_0^\infty S_\eta(\omega) d\omega. \quad (3.24)$$

If we consider only linear wave forcing, for the linear system in Eqn. (3.3) the response is also Gaussian. If the response is also narrow-banded, its exceedance probability can be found via the standard deviation of the response, which in turn can be obtained by integration of the response spectrum. From Eqn. (3.3) we have

$$\hat{\xi}(\omega) = \mathbf{H}(\omega)\hat{\mathbf{X}}(\omega)\hat{\eta}(\omega) \rightarrow \hat{\xi}_{glob}(\omega) = \mathbf{T}_{glob}\mathbf{H}(\omega)\hat{\mathbf{X}}(\omega)\hat{\eta}(\omega) \equiv \mathbf{TF}_{\eta \rightarrow \xi}(\omega)\hat{\eta}(\omega), \quad (3.25)$$

where $\mathbf{TF}_{\eta \rightarrow \xi}(\omega)$ is a direct transfer function from surface elevation to global response. The global response spectra $\mathbf{S}_{\xi, glob}(\omega)$ is related to the wave spectrum $S_\eta(\omega)$ in a similar way [27],

$$\mathbf{S}_{\xi, glob}(\omega) = \mathbf{TF}_{\eta \rightarrow \xi}(\omega)S_\eta(\omega)\mathbf{TF}_{\eta \rightarrow \xi}^{*T}(\omega). \quad (3.26)$$

Here *T indicates the transpose and complex conjugate. By virtue of Eqn. (3.23), the exceedance probability of e.g. the surge response ξ_1 is known from the variance of the surge response $\sigma_{\xi,1}^2$, which is given by

$$\sigma_{\xi,1}^2 = \int_0^\infty S_{\xi, glob, 11}(\omega) d\omega. \quad (3.27)$$

For nacelle acceleration we can write the response as a function of the global nacelle displacement $\xi_{glob,4}$, therefore

$$\hat{\xi}_{glob,4}(\omega) = -\omega^2 \xi_{glob,4}(\omega) \rightarrow \sigma_{\xi,4}^2 = \int_0^\infty \omega^4 S_{\xi, glob, 44}(\omega) d\omega. \quad (3.28)$$

The turbulent part of the wind speed can also be considered a Gaussian random variable [26]. On the other hand, aerodynamic loads are not a linear function of wind speed. Therefore the response to wind loads cannot be assumed to be Gaussian, and the approach shown above is not valid. However, the method above can be applied to cases with wind and wave forcing, bearing in mind that the results may

not be accurate since the necessary assumptions are not fulfilled. If wind and wave forcing are considered, Eqn. (3.3) can be written as

$$\hat{\xi}(\omega) = \mathbf{H}(\omega)\hat{\mathbf{F}}(\omega) \rightarrow \hat{\xi}_{glob}(\omega) = \mathbf{T}_{glob}\mathbf{H}(\omega)\hat{\mathbf{F}}(\omega) \equiv \mathbf{TF}_{F \rightarrow \xi}(\omega)\hat{\mathbf{F}}(\omega), \quad (3.29)$$

where $\mathbf{TF}_{F \rightarrow \xi}(\omega)$ is a direct transfer function from load to global response. The global response spectra $\mathbf{S}_{\xi, glob}(\omega)$ is now given by [27]:

$$\mathbf{S}_{\xi, glob}(\omega) = \mathbf{TF}_{F \rightarrow \xi}(\omega)\mathbf{S}_F(\omega)\mathbf{TF}_{F \rightarrow \xi}^{*T}(\omega). \quad (3.30)$$

Here $\mathbf{S}_F(\omega)$ is the spectra of the total loads (hydrodynamic and aerodynamic),

$$\mathbf{S}_F(\omega) = \frac{1}{2d\omega} \hat{\mathbf{F}}(\omega)\hat{\mathbf{F}}^{*T}(\omega). \quad (3.31)$$

This method provides the exceedance probability of the dynamic part of the response, therefore the static part should be added *after* applying Eqn. (3.23). Exceedance probability results from this method are compared in the next section to the traditional way of peak extraction from response time series.

3.3.3 Validation of the QuLAF model

We now compare and discuss the QuLAF and FAST responses to the same environmental conditions (see Table 9) representative of the Gulf of Maine, one of the defined LIFES50+ reference sites given in the design basis D7.2 [14]. The cases considered include five irregular sea states with and without turbulent wind, with a single realization for each sea state. In all cases the total simulated time was 5400 s in both models. The first 1800 s were neglected to discard initial transient effects in the time-domain model. The free-surface elevation of irregular sea states was computed in FAST from a Pierson-Moskowitz spectrum, and the turbulent wind fields in TurbSim from an IEC Kaimal spectrum. Since the turbulent wind fields used in the SoA simulations are the same employed for the precomputation of aerodynamic loads, and the free-surface elevation signal in the cascaded model is also taken from the FAST simulation, a deterministic comparison of time series is possible for all cases. In the plots shown in this section the left-hand side shows a portion of the time series of wind speed at hub height, free-surface elevation, floater surge, heave and pitch, and nacelle acceleration; and the right-hand side shows the PSDs of the same signals. The PSD signals were smoothened with a moving-average filter of 20 points to ease the spectral comparison between models. The short blue vertical lines in the PSD plots indicate the position of the system natural frequencies predicted by the simplified model (see Table 8). In addition, exceedance probability plots of the responses with both models are shown, based on peaks extracted from the time series. The peaks were sorted and assigned an exceedance probability based on their position in the sorted list. The exceedance probability of the extracted peaks is compared to the one estimated with the method described in Section 3.3.2.3, labeled as "Rayleigh".

3.3.3.1 System identification

The system natural frequencies were calculated in QuLAF by solving the eigenvalue problem in Eq. (3.4). In FAST, decay simulations were carried out with all DoFs active, where an initial displacement was introduced in each relevant DoF and the system was left to decay. A PSD of the relevant response revealed the natural frequency of each DoF. A comparison of natural frequencies and periods found with the two models is given in Table 8, where it is shown that all floater natural frequencies in the simplified model are within 1.3% error compared to the SoA model. On the other hand, the tower frequency is 8.6% below the one estimated in FAST. This difference is due to the absence of flexible blades in the simplified model, which are known to affect the coupled tower natural frequency. With rigid blades, the

SoA model predicts a coupled tower natural frequency of 0.684 Hz, only 0.3% above the tower frequency in QuLAF.

Table 8: Natural frequencies and periods obtained in FAST and QuLAF.

	Surge	Heave	Pitch	Tower
Natural frequency FAST [Hz]	0.0054	0.0478	0.0316	0.746
Natural frequency QuLAF [Hz]	0.0054	0.0480	0.0320	0.682
Error [%]	0.00	+0.42	+1.27	-8.58
Natural period FAST [s]	185.19	20.92	31.65	1.34
Natural period QuLAF [s]	185.19	20.83	31.25	1.47
Error [%]	0.00	-0.42	-1.25	+9.38

The model presented here may be calibrated against other numerical or physical models if needed, by introducing user-defined additional restoring and damping matrices. For the present study, however, no calibration against the state-of-the-art model was applied, in order to keep the model calibration-free and assess its suitability for optimization loops.

3.3.3.2 Response to irregular waves

The response to irregular waves with $H_s = 6.14$ m and $T_p = 12.5$ s (case "Waves 5" in Table 9) is shown in Figure 16. On the frequency side, all motions show response mainly at the wave frequency range, and there is a very good agreement between both models for surge and heave. In pitch — and consequently in nacelle acceleration — the QuLAF model shows a lower level of excitation at the wave frequency range when compared to FAST. This deviation was traced to the absence of viscous forcing in the simplified model, since the two pitch responses are almost identical if viscous effects are disabled in both models. As expected, the agreement is better for milder sea states, where viscous forcing is less important. In surge and pitch some energy is visible at the natural frequencies, only in the FAST model. Since the peaks lie out of the wave spectrum and are not captured by QuLAF, they could originate from nonlinear mooring effects or from the drag loads, which are also nonlinear.

Figure 17 shows exceedance probability plots of the response to irregular waves. The Rayleigh curves fit well to the responses given by the simplified model, which is expected, given that the free-surface elevation and the hydrodynamic forcing are linear in the model, and the response can be considered narrow-banded. In the comparison between the two models, the surge and heave peaks are very well estimated by QuLAF. In nacelle acceleration and especially in pitch, however, the model underpredicts the response, with a difference of about 30% in pitch and about 8% in nacelle acceleration for the largest peak when compared to FAST. These observations in extreme response are consistent with the spectral results of Figure 16 discussed above.

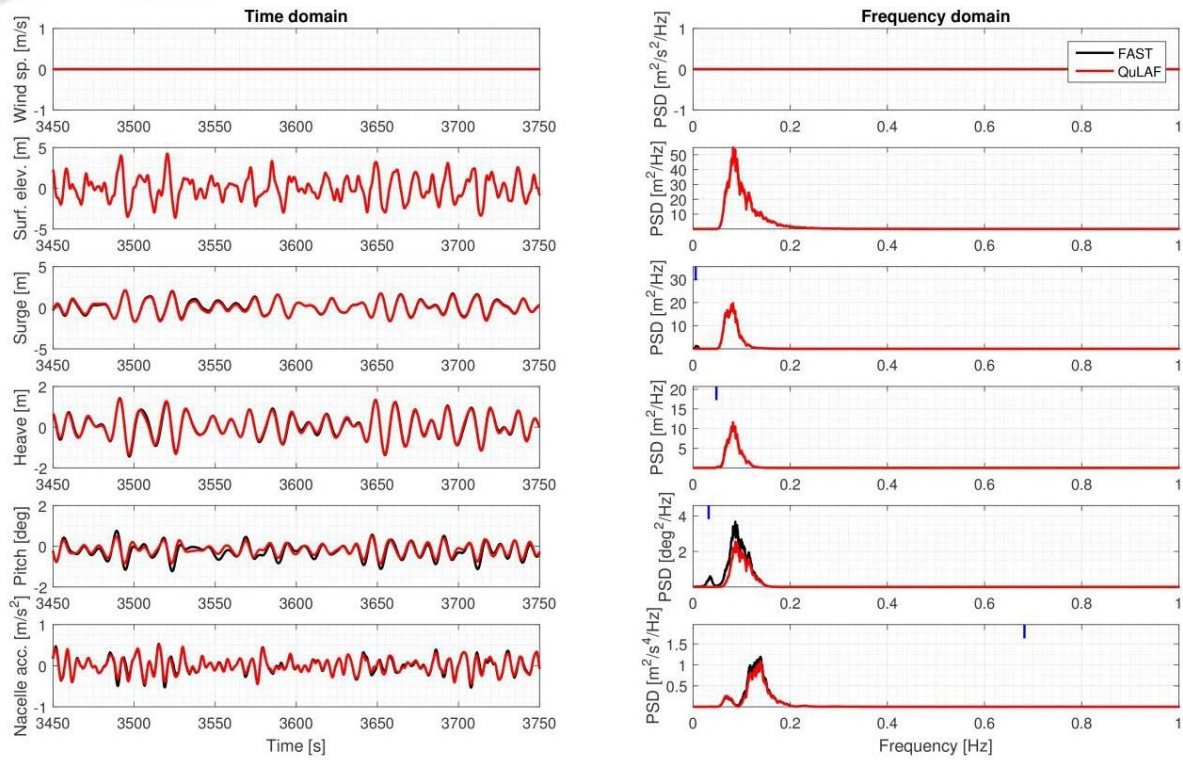


Figure 16: Response to irregular waves in time and frequency domain.

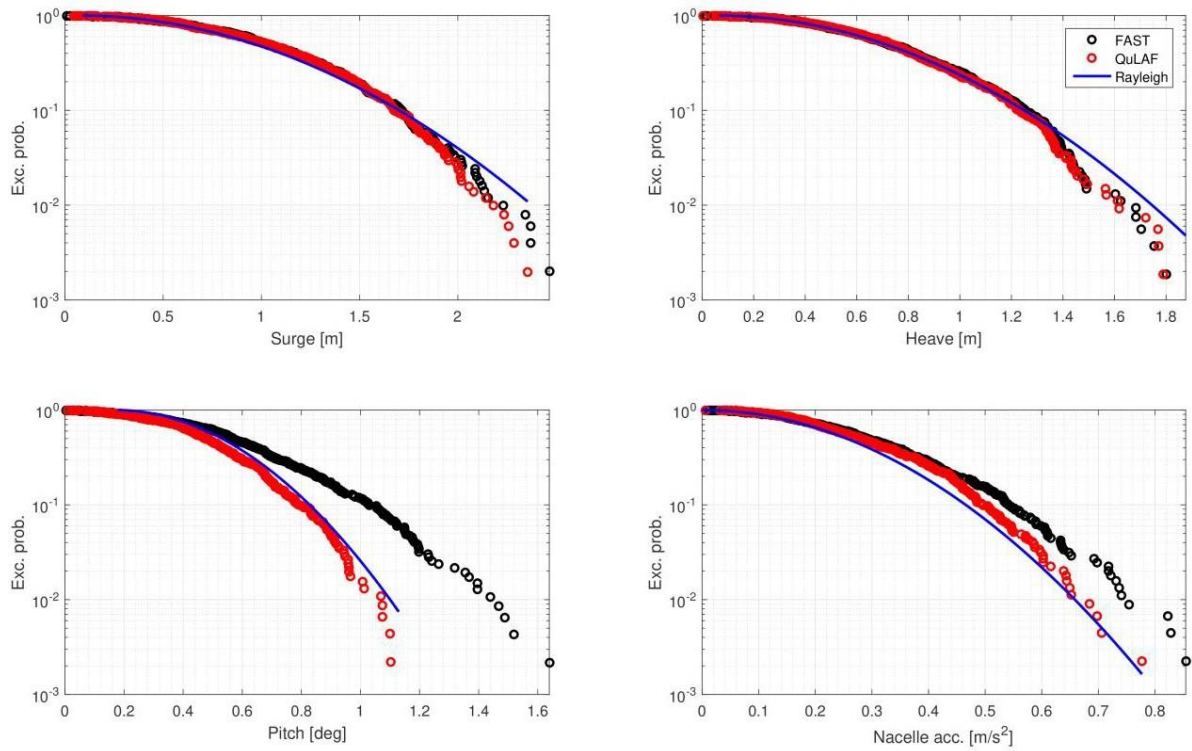


Figure 17: Exceedance probability of the response to irregular waves.

3.3.3.3 Response to irregular waves and turbulent wind

The response to irregular waves with $H_s = 6.14$ m and $T_p = 12.5$ s (case "Waves + wind 5" in Table 9) and turbulent wind at $W = 22$ m/s is shown in Figure 18. The surge motion is dominated by the surge natural frequency, which is clearly excited by the wind forcing. The linear model slightly underpredicts this resonance of the wind forcing with the surge natural frequency. Heave is dominated by the wave forcing, and the response of both models agree well. In pitch, resonance with the natural frequency also exists in both models, although QuLAF predicts more energy at that frequency than FAST. Both surge and pitch responses are resonant, thus they are especially sensitive to the amount of damping. The overprediction of pitch motion also leaves a footprint on the PSD of nacelle acceleration, which shows energy at the pitch natural frequency, the wave frequency range and the tower natural frequency. The level of excitation of the tower mode at 0.682 Hz, however, is slightly underpredicted by QuLAF, likely due to an overestimation of the aerodynamic damping on the tower DoF.

The associated exceedance probability plots are shown in Figure 19. In this case the Rayleigh curves generally do not fit the responses predicted by the linear model, as the extreme peaks are no longer Rayleigh-distributed. This is because the nonlinear nature of the wind loads makes the response non-Gaussian, and in some cases broad-banded with distinct frequency bands excited (e.g. the tower response cannot be considered narrow-banded here). The best fit is seen for heave, which is mainly excited by linear wave loads and is also narrow-banded. When compared to FAST, however, QuLAF shows a good agreement with errors in the largest response peaks of approximately 8% in surge, 12% in pitch and 4% in nacelle acceleration.

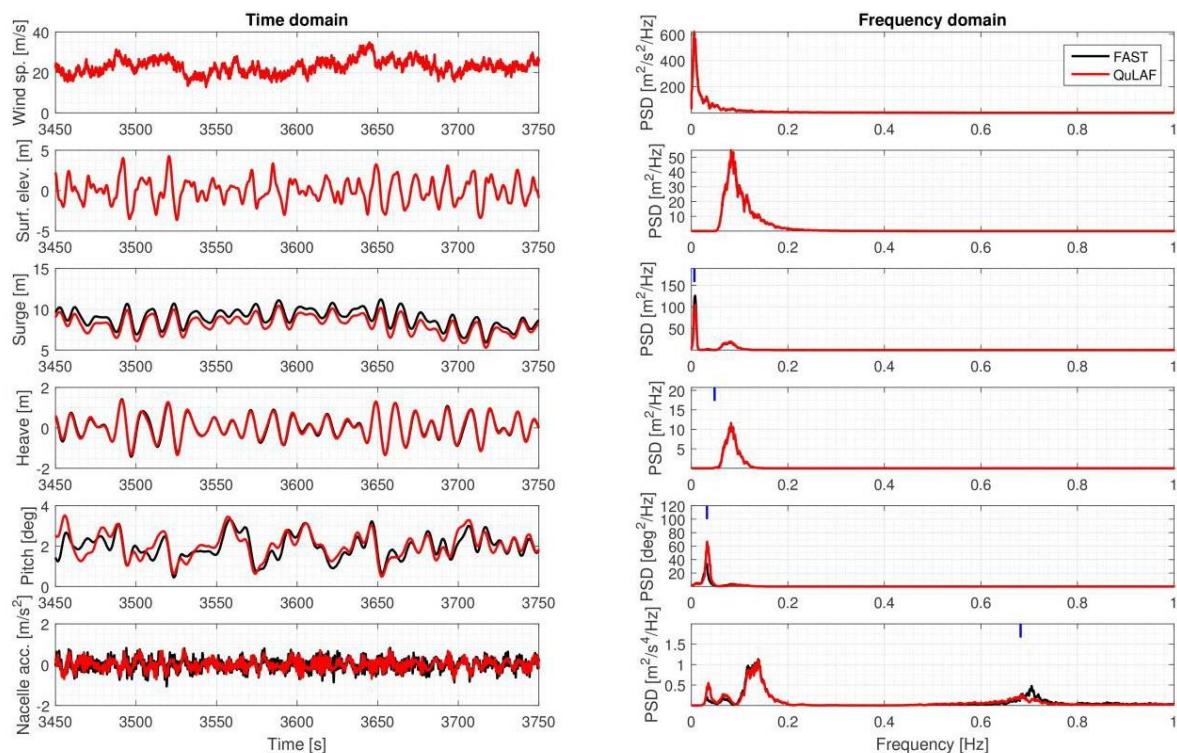


Figure 18: Response to irregular waves and turbulent wind in time and frequency domain.

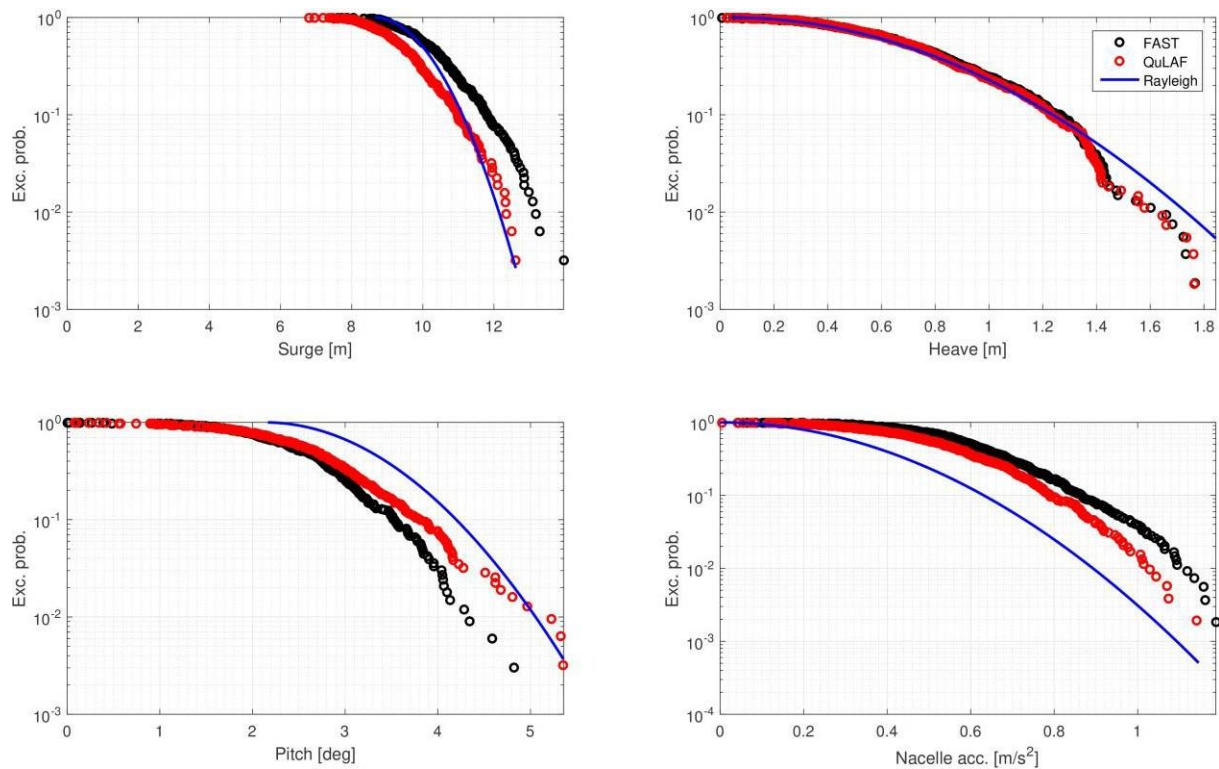


Figure 19: Exceedance probability of the response to irregular waves and turbulent wind.

3.3.3.4 Comparison of fatigue damage-equivalent loads

Table 9 below shows a summary of fatigue DELs for a wider range of environmental conditions. Each case is defined by the significant wave height H_s , the wave peak period T_p and the mean wind speed W . The fatigue damage-equivalent bending moment at the tower base estimated with the two models is presented, as well as the error for the simplified model. Finally, the last column shows the ratio between the simulated time and the CPU time in QuLAF, T_{rel} . The cases labeled as "5" correspond to the results discussed in the previous section. The two DEL columns in Table 9 are also shown in Figure 20 as a bar plot.

Table 9: Summary of environmental conditions [14] and tower bottom bending moment DEL results obtained in FAST and QuLAF.

Case	H_s	T_p	W	DEL_{FAST}	DEL_{QuLAF}	Error	T_{rel}
	[m]	[s]	[m/s]	[MNm]	[MNm]	[%]	[-]
Waves 1	1.51	7.65	-	75.69	76.44	+1.00	2402
Waves 2	1.97	8.00	-	98.44	98.62	+0.19	2695
Waves 3	2.43	8.29	-	120.74	119.95	-0.65	2595
Waves 4	3.97	9.85	-	179.45	170.55	-4.96	2404
Waves 5 (Figure 16,Figure 17)	6.14	12.50	-	219.31	194.63	-11.25	2595
Waves + wind 1	1.51	7.65	6.0	167.13	158.74	-5.02	1354
Waves + wind 2	1.97	8.00	9.0	290.96	284.53	-2.21	1409
Waves + wind 3	2.43	8.29	11.4	375.12	349.37	-6.87	1400
Waves + wind 4	3.97	9.85	17.0	319.95	324.68	+1.48	1365
Waves + wind 5 (Figure 18,Figure 19)	6.14	12.50	22.0	339.01	348.77	+2.88	1408

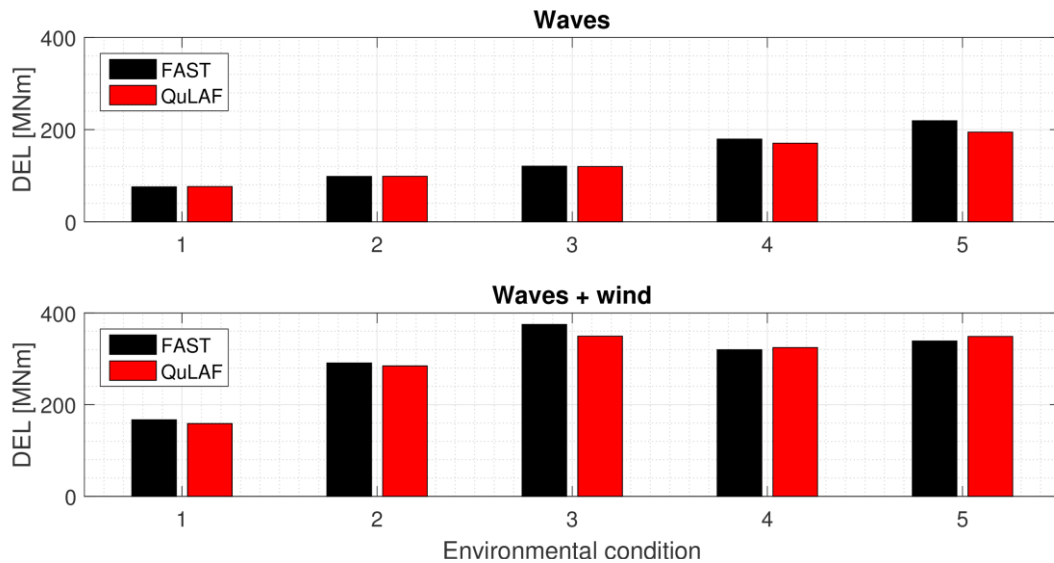


Figure 20: Damage-equivalent bending moment at the tower base for different environmental conditions.

For the cases with waves only, the model underpredicts the DEL at the tower base with errors from 0.2% to 11.3% that increase with the sea state, as observed in Figure 20. The significant wave height also increases with the sea state, as do the associated nonlinear effects of position-dependent mooring stiffness and viscous hydrodynamic forcing, which are both included in FAST. QuLAF does not include viscous hydrodynamic forcing, and as a linear model, its accuracy is bound to the assumptions of small displacements around the equilibrium point. Hence, it is expected that the linear model performs worse for the environmental conditions where nonlinear effects are not negligible. This observation is also consistent with the discussion around Figure 16, which corresponds to the most severe sea state.

For the cases with wind the errors range from 1.5% to 6.9%, but the trend is not as clear. The predictions seem to be worst for the environmental condition corresponding to rated wind speed. Around rated speed the wind turbine operation switches between the partial- and the full-load regions, which correspond to very distinct regimes of the generator torque and blade pitch controller. The complexity of the dynamics involved in this transition zone is not well captured by the simplified model. The vibration of the tower is also more likely to be excited around rated wind speed, where the thrust is maximum. As the coupled tower natural frequency is different for the two models, this will also have an impact on the resulting DEL. This effect has been quantified for rated wind speed ("Waves + wind 3"), where the DEL error becomes -5.6% when the FAST simulation is carried out with rigid blades, which indicates that the difference in coupled tower frequency has some impact on the DEL error. In addition, the aerodynamic damping — which plays an important role in the resonant response of the tower — is dependent on the frequency at which the rotor moves in and out of the wind. Since the aerodynamic damping on the tower is extracted from a SoA simulation with fixed foundation and rigid blades, it corresponds to a tower natural frequency of 0.51 Hz, different to the coupled tower frequency observed when the floater DoFs are active (0.682 Hz in QuLAF, 0.746 in FAST). This difference in the frequencies at which the aerodynamic damping is extracted and applied is likely to lead to an overprediction of the aerodynamic damping, and an underprediction of the tower vibration and the DEL. This observation is consistent with the level of tower response at the coupled tower frequency shown in Figure 18. On the other hand, the aerodynamic simplifications in the cascaded model seem to work best for wind speeds above rated, likely due to the thrust curve being flatter in this region. The last column of Table 9 shows that the ratio between simulated time and CPU time is between 1300 and 2700 in a standard laptop with an Intel Core i5-5300U processor at 2.30 GHz and 16 GB of RAM. In other words, all the simulations in Table 9 together, 1.5 h long each, can be done in about half a minute.

3.3.4 Conclusions on the QuLAF model

A model for Quick Load Analysis of Floating wind turbines, QuLAF, has been presented and validated. The model is a linear, frequency-domain tool with four planar degrees of freedom: floater surge, heave, pitch and tower modal deflection. The model relies on higher-fidelity tools from which hydrodynamic, aerodynamic and mooring loads are extracted and cascaded. Hydrodynamic and aerodynamic loads are precomputed in WAMIT and FAST respectively, while the mooring system is linearized around the equilibrium position for each wind speed using MoorDyn. A simplified approach for viscous hydrodynamic damping was implemented, and the decay-based extraction of aerodynamic damping of Schløer et al. [23] was extended to multiple degrees of freedom. Without introducing any calibration, a case study with a semi-submersible 10MW configuration showed that the model is able to predict the motions of the system in stochastic wind and waves with acceptable accuracy. The damage-equivalent bending moment at the tower base is estimated with errors between 0.2% and 11.3% for all the five load cases considered in this study, covering the operational wind speed range. The largest errors were observed for the most severe wave climates in wave-only conditions and for turbine operation around rated wind speed for combined wind and wave conditions, due to three main limitations in the model: i) underprediction of hydrodynamic loads in severe sea states due to the omission of viscous drag forcing; ii) difficulty to capture the complexity of aerodynamic loads around rated wind speed, where the controller switches between the partial- and full-load regions; and iii) errors in the estimation of the tower response due to underprediction of the coupled tower natural frequency and overprediction of the aerodynamic damping on the tower. The computational speed in QuLAF is between 1300 and 2700 times faster than real time. Although not done in this study, introducing viscous hydrodynamic forcing and calibration of the damping against the SoA model would likely result in improved accuracy, but at the expense of lower CPU efficiency and less generality in the model formulation.

It has been shown that the model can be used as a tool to explore the design space in the preliminary design stages of a floating substructure for offshore wind. The model can quickly give an estimate of the main natural frequencies, response and loads for a wide range of environmental conditions with aligned wind and waves, which makes it useful for optimization loops. Although a better performance may be achieved through calibration, a calibration-free approach was used here to emulate the reality of an optimization loop, where calibration is not possible. In such process, once an optimized design has been found, a full aero-hydro-servo-elastic model is still necessary to assess the performance in a wider range of environmental conditions, including nonlinearities, transient effects and real-time control. Since the model is directly extracted from such a state-of-the-art model, this step can readily be taken. While the state-of-the-art model should thus still be used in the design verification, the present model provides an efficient and relatively accurate complementary tool for rational engineering design, parameter studies and concept optimisation of offshore wind turbine floaters.

3.3.5 Extended study of D7.8

In addition, the QuLAF and FAST models presented here have been recently used in deliverable D7.8 [28] for a broader analysis of different design-driving load cases, including normal operation, extreme and transient events (see Figure 21). Generally, the results of the broader study and the conclusions drawn are aligned with the ones presented here, as well as the limitations observed in the simplified model when compared to its SoA counterpart.

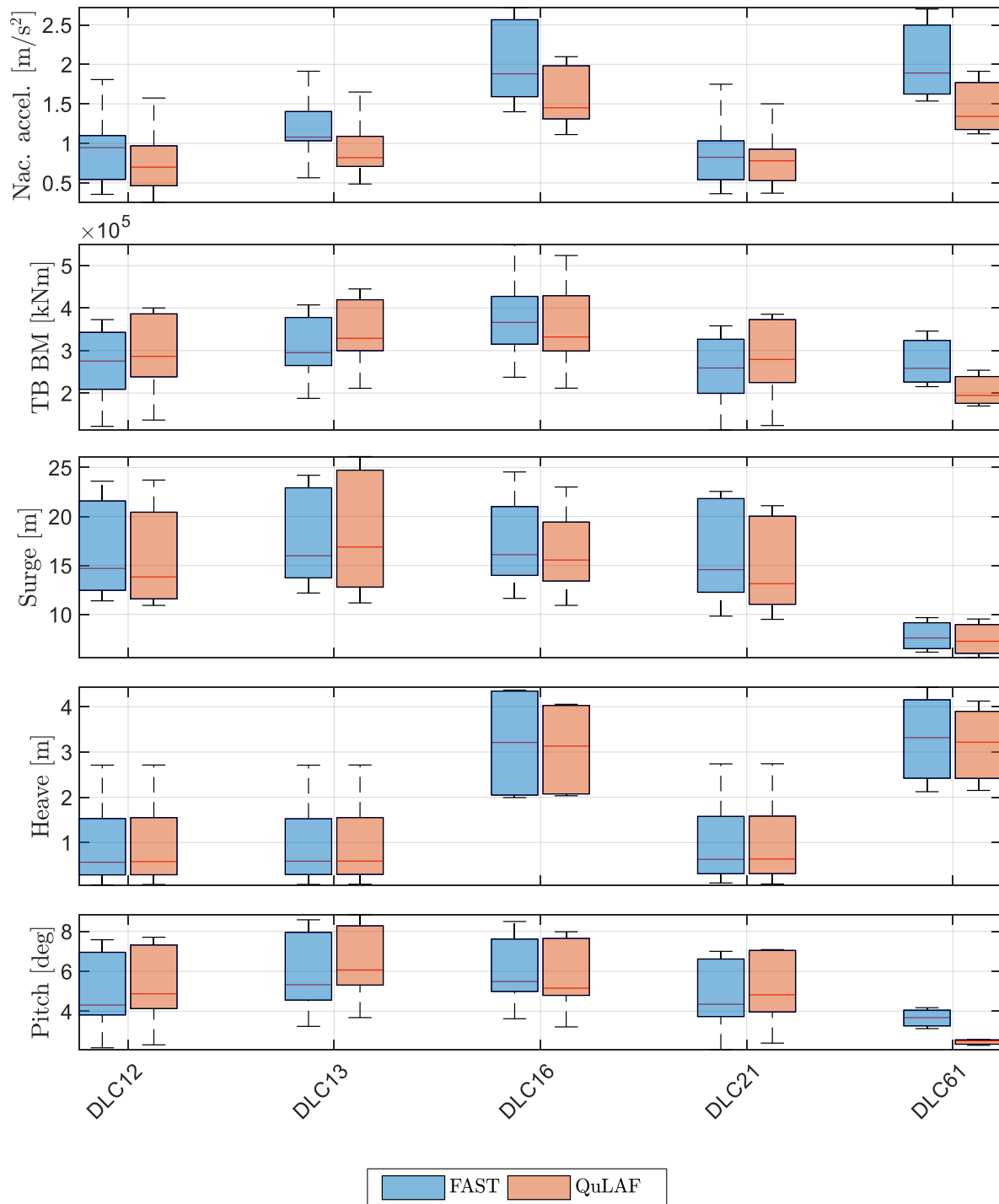


Figure 21: Comparative ULS analysis based on the planar version of DLC 1.2, 1.3, 1.6, 2.1 and 6.1 extracted from [28]. From top to bottom, the plots show the population of the maximum values of nacelle acceleration, tower-base bending moment, and floater surge, heave and pitch obtained with FAST and QuLAF.

3.4 Conclusions for the OO-Star Wind Floater Semi 10MW

In the comparison between the state-of-the-art numerical model and the physical tests, it has been shown that calibration of the linear and quadratic global damping matrices against the decay tests is not sufficient to predict the response to waves. On the other hand, if the global linear damping matrix is calibrated for each specific sea state, the model is able to reproduce the measured response with errors up to 13% in the 95% percentile, with most cases under 8%.

The simplified model can predict the damage-equivalent bending moment at the tower base with errors up to 11.3% for the operational wind speed range. The largest deviations in wave-only conditions occur for severe wave climates due to the absence of viscous drag forcing. In cases with wind, the largest deviations are observed for wind speeds around rated, due to the different load regions for the controller and to the overprediction of the aerodynamic damping on the tower. The simplified model is between 1300 and 2700 faster than real time.

Regarding the design-driving load cases, studies carried out in WP7 indicate that DLC 1.2, 1.6 and 6.1 provide a good overview of the system's performance. Failure conditions such as loss of mooring lines (DLC 10.x) also generates design-driving loads which are, however, highly dependent on floater design details.

4 State-of-the-art model of the NAUTILUS-DTU10

4.1 Design-driving load cases

Similar evaluations as for the OO-Star Wind Floater Semi 10MW were also performed for the Nautilus concept as part of this deliverable and in [3]. While the principle trends regarding load sensitivity can be translated to this semi-submersible platform, some general difference was found in the sensitivity towards the wave periods and wave height. For this Nautilus platform for fatigue loads during normal sea states, a smaller impact of wave heights and wave periods was found, which may be resulting from the active ballasting system, which limits the pitch motion during sea states with large wave heights (which typically occur during large wind speeds). Furthermore, for this platform, larger wave periods may lead to increased ultimate loads in the mooring system, which was not found for the OO-Star Wind Floater Semi 10MW (where a semi-taut mooring system is applied instead of a full catenary). Figure 4-1 shows exemplary results in the form of scatterplots from the sensitivity analysis for DLC 1.6.

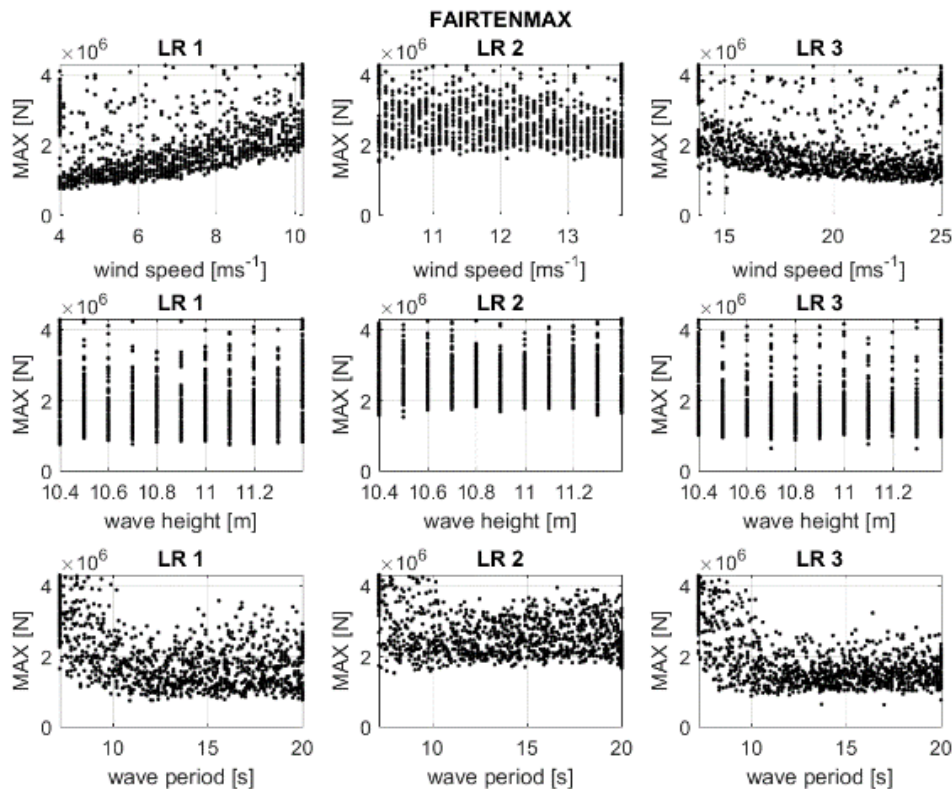


Figure 4-1: NAUTILUS-DTU10 results of sensitivity study for maximum fairlead tension (FAIRTENMAX). Results are shown for different load ranges (columns) and environmental conditions (rows).

4.2 Comparison to ocean wave tests

In LIFES50+ Deliverable 4.5 [2], a FAST model has been outlined to describe the DTU 10MW Reference Wind Turbine mounted on the NAUTILUS-10 floating substructure. The report is based on the description of the two FOWT designs of LIFES50+ D4.2 [1].

The hydrodynamics of the FAST model are based on first order radiation-diffraction hydrodynamics through the Cummins equation. The potential damping, potential added mass and the force-RAO are

calculated in WAMIT [9]. Additionally, it uses linear and quadratic lumped damping matrices to capture viscous effects. These are applied at the centre of flotation in the FAST model. This however neglects the relative velocity between the floating substructure and the wave field.

Furthermore, an alternative Morison-based formulation of the viscous effects on the NAUTILUS-10 floating substructure can be seen in the Appendix of Deliverable D4.5. Based on the latter modelling approach, the following chapter compares simulation results to the wave basin tests. The Morison element model is thus first calibrated and tuned to the free decay tests carried out in the wave basin, and finally a comparison with an irregular wave tests is made.

4.2.1 Model adaption

A series of changes had to be made to the FAST model to have the geometry that the model tested in the wave basin possessed. The tower tested at the basin on the scaled model had a different Eigen-frequency than the up-scaled prototype which the FAST model in Deliverable D4.5 is based on. This tower characteristic is mentioned in page 11 of Part II of Deliverable D3.4 [4].

The changes of the wave basin scaled model are outlined in Deliverable D3.4. This includes:

- Overhang of the rotor-nacelle assembly (RNA) is neglected
- Numerical part of the HiL model includes two DOFs in addition to the platform DOFs; the generator and the first flapwise mode of the blade
- Platform mass and inertias are slightly different for the scaled model test than those of the FAST Nautilus model. The properties of the scaled model were identified through a pendulum test
- Active ballast system of NAUTILUS-DTU10 is not entirely modelled in the experiment, five static distributions of the ballast mass are tested
- Modified mooring system is used in the experiment with two separate lines, connected by a spring.

This has some implications on the FAST model:

- Downwind distance from the tower-top to the nacelle centre of mass (NacCMxn parameter) was set to 0
- Overhang (OverHang parameter) in FAST is set to 0
- Shaft tilt angle is set to zero
- Two flapwise modes of the blades are turned off.
- Nacelle inertia about the yaw axis (NacYIner) is set to 0
- Platform mass and inertias are set to match those of the experiment
- Platform ballast and submerged volume is modelled in one configuration only, the one corresponding to zero wind speed.
- Mooring model is not changed but the original system is simulated

The panel code calculation was run with a draft of 17.36m, corresponding to the ballast mass for zero wind speed. The mean drift coefficients from the nearfield solution are used for Newman's approximation of the second-order difference-frequency wave forces. The wave direction is of -15 degrees, according to the main wave heading angle of the tests [4].

Table 4-1: Summary of hydrodynamic modelling of the applied FAST model

FAST Model	First order potential flow forces	Second Order waves	Second order potential flow forces	Tuned lumped stiffness or damping matrix	Morison Elements
Modified D4.5 Morison elements model with second-order forces	Yes	No	Yes	No	Yes

Modified refers to the fact that the masses and inertias of the FAST files have been changed to match those of the wave basin test.

4.2.1.1 Mass properties

Table 4-2 shows a summary of the mass properties of the FAST models and compared to the one tested in the wave basin. The hub height is 119m.

Table 4-2: Summary of masses of the FAST models

	Modified FAST models	Sintef wave basin test (ballast filled for 0m/s wind speed)
Blade mass (kg)	41,692.85	
Nacelle mass (kg)	446,036	
Hub mass (kg)	10,5520	
Tower (kg)	879,380.62	
Tower-top Mass (3 blades + hub+nacelle) (kg)	676,634.56	
RNA + tower (kg)	1,556,015.19	1,557,000
Platform mass (kg)	7,328,000	7,328,000
Ixx platform (kg m ²)	4.635E+09	4.635E+09
Iyy platform (kg m ²)	4.634E+09	4.634E+09
Izz platform (kg m ²)	7.981E+09	7.981E+09

4.2.1.2 Damping properties

FAST allows modelling of viscous drag through Morison elements. This modelling approach, used in HydroDyn, only allows cylindrical members to represent drag.

For the Nautilus platform, the horizontal pontoon element diameter (1.5m) was chosen in D4.5 to match the drag in the surge/sway direction. For the vertical drag, the creation of a virtual heave plate, centered underneath the tower base, was implemented in the D4.5 Appendix (also see green circle in Figure 4-2). To ease the damping calibration, an alternative approach was developed in the present work. Instead of a virtual centred heave plate, a series of circular heave plates, located along the area where the elements that connect the columns, is defined (3 per section of the pontoon connecting 2 different columns). This helps support a streamline tuning of the damping coefficient during the calibration of the decay tests. The coefficient of drag of these vertical pontoon plates was taken by dividing the value used in D4.5 (15.61) by 12 (remembering that the areas of each plate are the same as the area of the virtual heave plate). These pontoon plates only contribute a vertical direction drag. The circular areas underneath the columns have another vertical drag coefficient. This was specified in D4.5.

The new, alternative layout of the vertical heave plate drag nodes is shown in Figure 4-3.

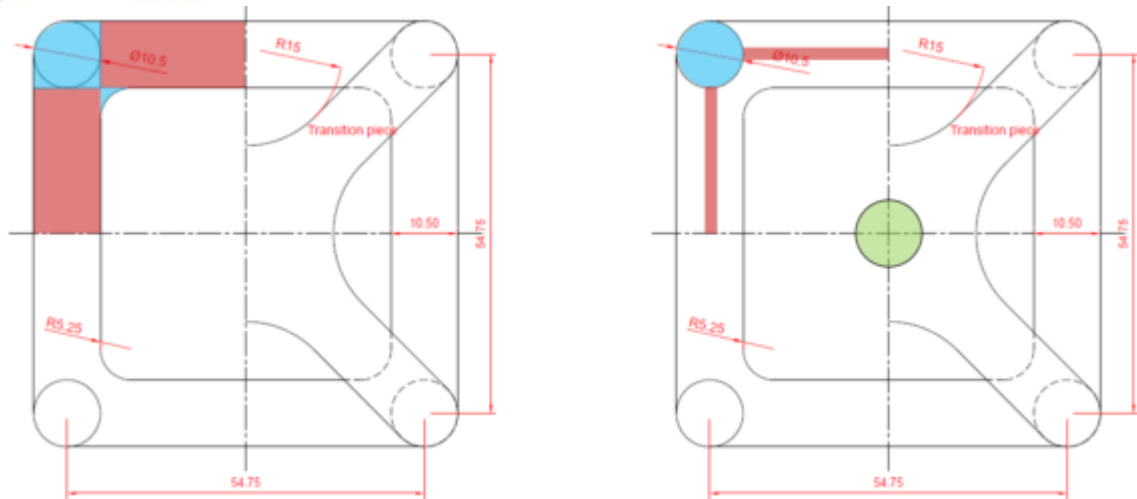


Figure 4-2 : Physical (left) and model (right) representations of the pontoons for the NAUTILUS-10 floating substructure [2].

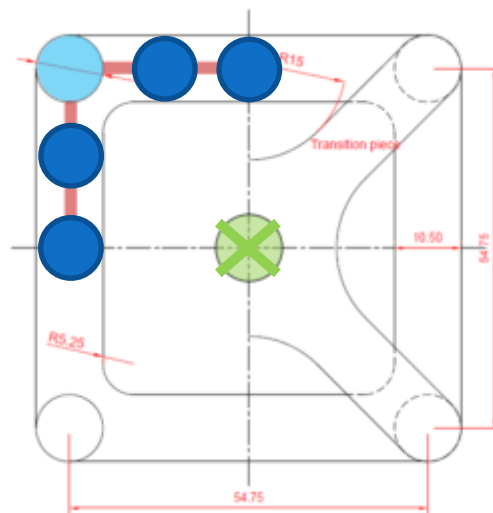


Figure 4-3: Modified Morison element model. Modification to modelling of heave plates of the Nautilus platform for FAST

The coefficients of drag are mentioned in the following table.

Table 4-3: Coefficients of drag used in the Morison element model based on the values given in D4.5

	Diameter	Deliverable 4.5	Modified Morison Element model
Cd columns lateral (Cd_col_lat)	10.5	0.715	0.715
Cd heave plate lateral (Cd_hp_lat)	1.5	2.05	2.05
Cd virtual heave plate vertical (Cd_vhp_ver)	10.5	31.12	-
Cd column heave plate vertical (Cd_chp_ver)	10.5	15.61	15.61
Cd pontoon circular plates vertical (Cd_pon_ver)	10.5	-	2.59

4.2.2 Model calibration

The following experimental tests were used for comparison and tuning purposes. The test number is outlined in detail in Appendix A of Deliverable D3.4 [4].

Table 4-4: Test carried out at the wave basin

Test number	Test description
2011	PULL OUT TEST SURGE
3011	DECAY FREE HEAVE LC_NW
3020	DECAY FREE PITCH LC_NW
3110	DECAY MOORED SURGE LC_NW
3130	DECAY MOORED HEAVE LC_NW
3150	DECAY MOORED PITCH LC_NW
3160	DECAY MOORED YAW LC_NW
6270	DLC1.6 PM H7.7 T12.4 D0 LC_NW
6241	DLC1.6 PM H10.9 T15.0 D0 LC_NW
4220	PN H4 T4.5-18.2 D0 LC_NW

PM = Pierson Moskowitz, PN = Pink noise, DLC = design load case, LC_NW = load case no wind

As reference for this deliverable, the following tables Table 4-5 and Table 4-6 from D3.4 show the results from the decay analysis of the experimental data.

Table 4-5: Decay analysis free floating floater. Natural period T_n , relative damping coefficient, linear and quadratic damping coefficients (p_1 and p_2 , relative damping coefficient). No wind lines.

Degree of freedom	T_n (s)	Rel. Damping (-)	p_1 (1/s)	p_2 (1/m or 1)
Heave	19.22	0.039	6.41E+01	2.08E+3
Pitch	32.44	0.037	7.71E+01	6.50E-02

Table 4-6: Decay analysis moored floater. Natural period T_n , relative damping coefficient, linear and quadratic damping coefficients (p_1 and p_2 , relative damping coefficient). No wind lines.

Degree of freedom	T_n (s)	Rel. Damping (-)	p_1 (1/s)	p_2 (1/m or 1)
Surge	126.55	0.040	1.38E+01	3.38E+02
Heave	19.18	0.039	6.67E+01	2.29E+03
pitch	31.27	0.106	2.05E+02	5.18E-01
yaw	95.19	0.029	2.23E+01	6.99E+03

4.2.2.1 Decay free heave: Load Case No Wind

Figure 4-4 show a section of the test data for decay in the heave direction with no mooring and compares it with the FAST simulation model results. The mean offset of the test data has been removed to be able to better visualize the comparison of the damping and frequencies. As can be seen in the figure, the Modified Morison elements model still needs tuning of the coefficients of drag to better fit the damping.

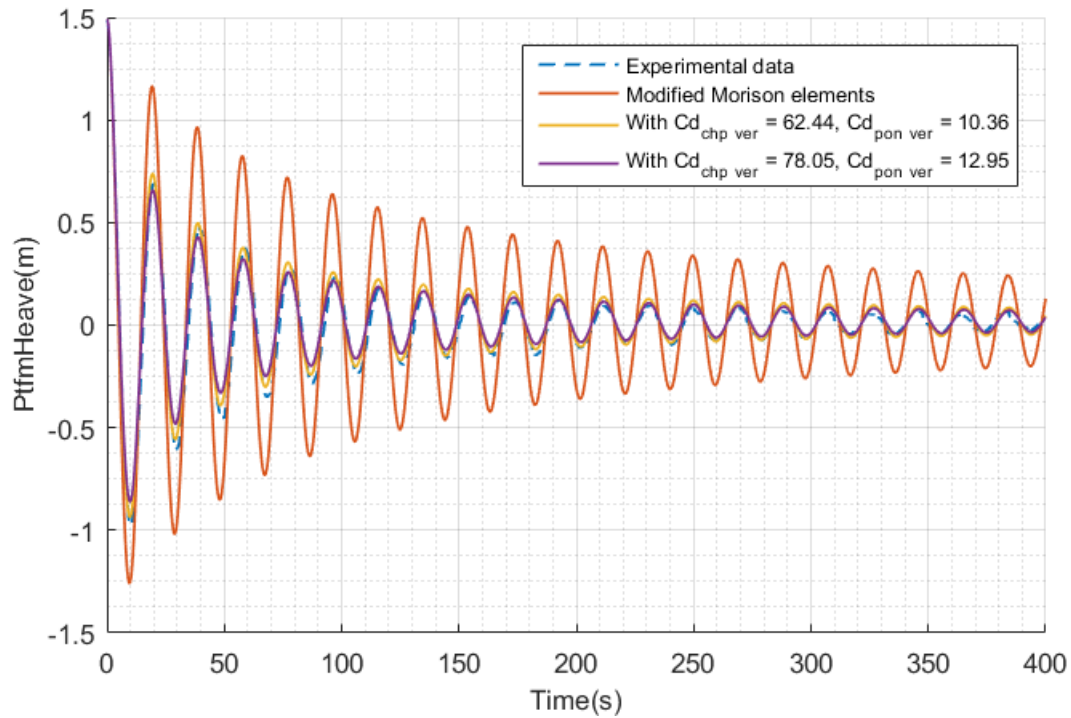


Figure 4-4 : Test3011 comparison of heave decay simulation with experimental data for different FAST models

To perform the tuning, the vertical coefficients of drag are changed in order to find a good fit with the experimental results. The coefficients of drag of the Modified Morison elements model have 4 different values, representing two different elements types in the lateral direction and two different in the vertical direction. In the vertical direction, the pontoon circular plates and the columns contribute to the damping in heave. These have been increased by a factor of 4 and 5, respectively, compared to the original values to match the measured response.

4.2.2.2 Free decay pitch: Load Case No Wind

Figure 4-5 shows a section of the test data for decay in the pitch with no mooring.

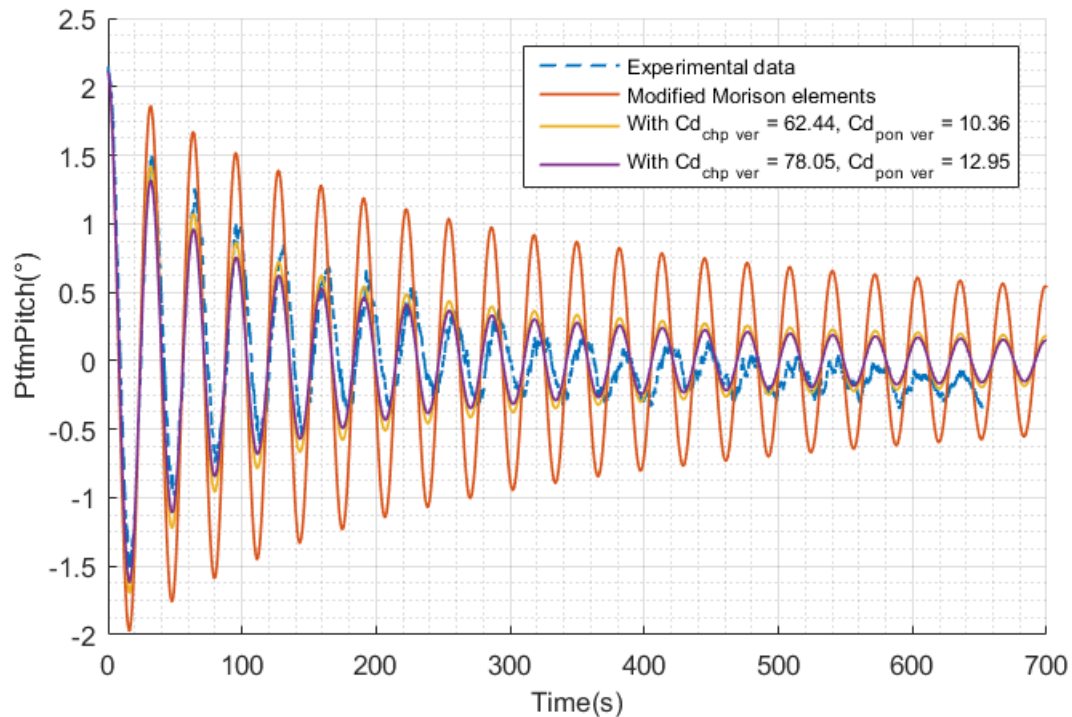


Figure 4-5: Test3020 comparison of pitch free decay simulation with no mooring with experimental data for different FAST models

The pitch decay test data shown in the previous Figure 4-5 seems to not come to a complete rest at 0° pitch. The frequency of the time series calculated with a fast Fourier transform yields a frequency of 0.0307 Hz, which is well aligned with the measurement data. An increase by factor five (shown in the solid blue line) of the vertical damping yields a reasonable match of the decay.

4.2.2.3 Summary of unmoored free decay damping properties

Following is a summary of the free decay properties regarding frequencies (Table 4-8) and coefficients of drag (Table 4-7) in the axial direction.

Table 4-7: Coefficients of drag used in the Morison element model after tuning of free decay tests

	Diameter (m)	Deliverable 4.5	Modified Morison Element model
Cd virtual heave plate vertical	10.5	31.12	-
Cd column heave plate vertical	10.5	15.61	78.05
Cd pontoon plates vertical	10.5	-	12.95

Table 4-8: Frequency of the Morison element model after tuning of free decay tests and the tests

	Test	Modified Morison Element model	Percentage difference
Free decay heave (Hz)	0.0522	0.0522	0%
Free decay pitch (Hz)	0.0307	0.0311	1.3%

4.2.2.4 Mooring and surge pull-out test

The mooring model of the test was modified in order to fit the tested mooring line, which was composed of 3-line sections with different specific weights and elasticity moduli (EA). The mooring lines of the tested platform were described in D3.4.

The test value of the specific weight of the mooring line which was then used for the Modified Morison elements model was calculated to be 180.652(kg/m). This results from the equation:

$$S_{w_0} = \frac{S_{w_1}L_1 + S_{w_2}L_2 + S_{w_3}L_3}{L_0} \quad (4.1)$$

Where S_w is the specific weight (kg/m) of the mooring line. There are 3 lines sections per mooring line used in the test model with different lengths L.

During the moored decay tests, it was found that the surge frequency did not match well that of the experiments. Therefore, the mooring model was tuned to give a better match to the tests. There is a trade-off though, and as the surge frequency improves, then the yaw frequency deviates from the test yaw frequency. The catenary mooring lines have an effect on the surge and yaw response, but they are not very significant for the heave and pitch response. The influence of the cable-driven robot is not addressed in this work. It was chosen to have the best fit for the surge response because the surge-DOF shows the largest response to wind and waves. This was achieved by changing the value of the weight of the mooring line (kg/m). A modification of the elasticity (EA) value by 10% showed no significant changes in the frequency or tension of the mooring lines, so this approach was not used. The tuning is shown later on.

The static equilibrium test was used to verify the static tension on the mooring lines. Table 4-9 shows the tensions calculated by the model after they have been initialized and converge to static equilibrium and compared with those already presented in Deliverable D3.4.

Table 4-9: Static equilibrium mooring line tension.

	Line 1	Line 2	Line 3	Line 4
Specified pre-tension (kN)	5.810E+02	5.810E+02	5.810E+02	5.810E+02
Measured pre-tension D3.4 (kN)	5.413E+02	5.280E+02	5.380E+02	5.260E+02
deviation %	-6.82	-9.13	-7.40	-9.46
Morison element model (kN)	5.07E+02	5.07E+02	5.07E+02	5.07E+02
deviation % compared to D3.4	-6.34	-3.98	-5.76	-3.61

Furthermore, the pull-out Test2021 was used to obtain the static tension at the anchor with different displacements of the floater and compare the results to static simulations. The results are shown in Table 4-10. The pull-out test started with an offset in surge of -1.356m. The values presented are mean values as the signals and simulations contain some noise and vibrations.

Table 4-10: Pull out Test 2021 mooring line tension

	Test	FAST	Test	FAST	Test	FAST	Test	FAST	Test	FAST
Surge Displacement (m)	-1.356	0	-3.848	2.5	-10.74	9.4	-20.82	19.5	-31.81	30.5
Remove offset (m)	0		-2.492		-9.384		-19.464		-30.454	
Ankerline 1 tension (N)	5.341E5	5.07E+05	5.687E5	5.41E5	6.856E5	6.63E5	9.809E5	9.6E5	1.624E6	1.6515E6
Ankerline 2 tension (N)	5.278E5	5.07E+05	5.631E5	5.41E5	6.814E5	6.63E5	9.717E5	9.6E5	1.605E6	1.6515E6
Ankerline 3 tension (N)	5.362E5	5.07E+05	5.038E5	4.77E5	4.372E5	4.11E5	3.693E5	3.4E5	3.234E5	2.955E5
Ankerline 4 tension (N)	5.24E5	5.07E+05	4.931E5	4.77E5	4.305E5	4.11E5	3.62E5	3.4E5	3.211E5	2.955E5

4.2.2.5 Decay moored heave: Load Case No Wind

Figure 4-7 shows a section of the test data for decay in the heave direction when the platform is moored. The mean offset of the experimental data has been removed for comparison purposes. It is seen that the Modified Morison Element model has a slight heave offset of about 5cm. The agreement between the model and the experiment is reasonable and no further tuning has been applied at this stage.

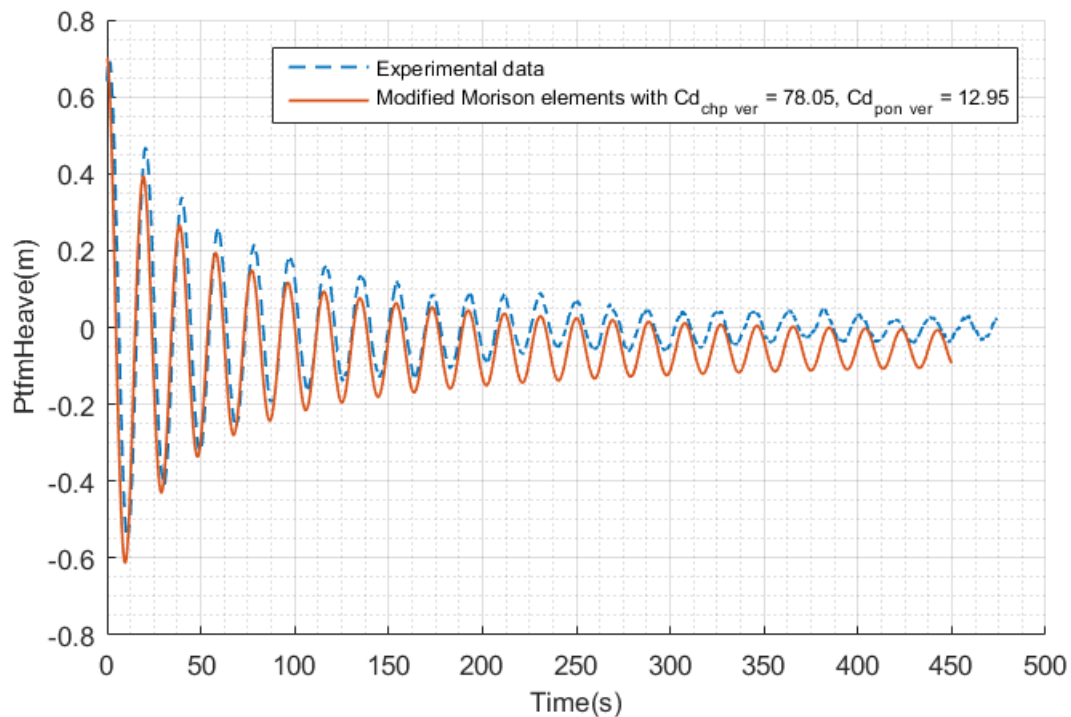


Figure 4-6: Comparison of moored heave decay simulation with experimental data

4.2.2.6 Decay moored pitch: Load Case No Wind

Figure 4-10 shows a section of the test data for decay in the pitch when the platform is moored. It is seen that the Modified Morison Element model is slightly underdamped, but the agreement between the Modified Morison Element model with five times the axial damping of D4.5 and the experiment is reasonable, and no further tuning has been applied at this stage.

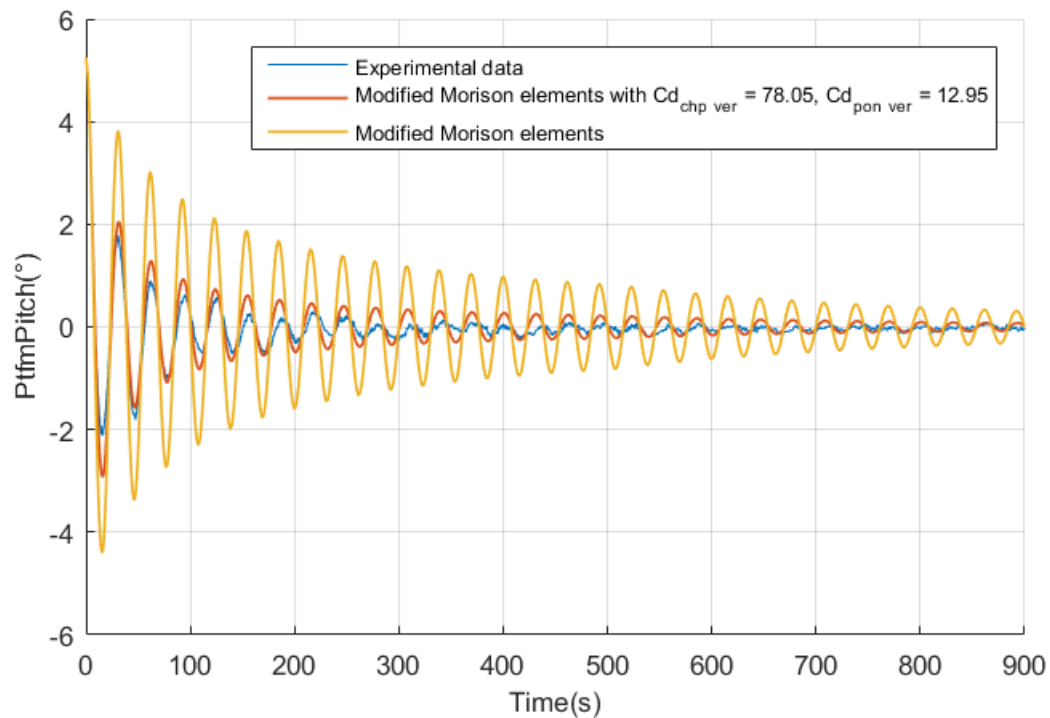


Figure 4-7: Comparison of moored pitch decay simulation with experimental data

4.2.2.7 Decay moored surge: Load Case No Wind

Figure 4-9 shows a section of the test data for decay in the surge direction with mooring. The Morison Element model needs to be tuned in order to better fit the test data and as mentioned beforehand, for this, the specific weight of the mooring model has been used. The factor for tuning was that of 0.87 leading to a value of 157.14(kg/m). The tuning from the previous sections was also included.

The damping of the surge also seems to be too large and thus the traverse damping values of the column and of the pontoon. The coefficients have been halved to better fit the data. However, halving the coefficient of drag of the column leads to a very low value of 0.3575, which is not something common from experimental data of a cylinder. This drag value might compensate an overly large drag coefficient of the mooring lines.

The damping behaviors still shows discrepancies in the region when the oscillation is below 1m in amplitude. Here, the response is overdamped. It would look like in this case less damping is needed to be able to achieve a higher oscillation amplitude at the lower oscillation amplitudes, yet it would probably also mean that more damping would be needed. Such fine tuning has already been shown necessary in this deliverable with the OO-Star Wind Floater Semi 10MW platform.

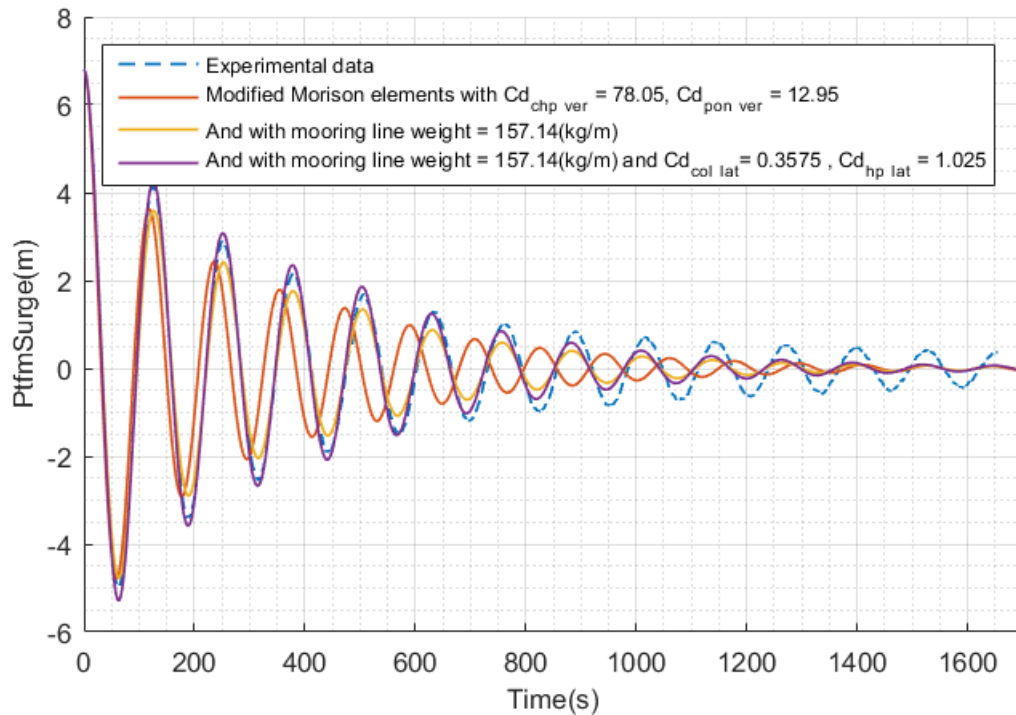


Figure 4-8: Comparison of moored surge decay simulation with experimental data

4.2.2.8 Decay moored yaw: Load Case No Wind

Figure 4-10 shows a section of the test data for decay in the yaw direction with mooring. The Modified Morison Elements model needs to be tuned in order to better fit the test data and as mentioned before-hand, there is a trade-off between tuning the yaw and surge frequencies. In this case the tuned specific mooring weight has a negative effect on the frequency.

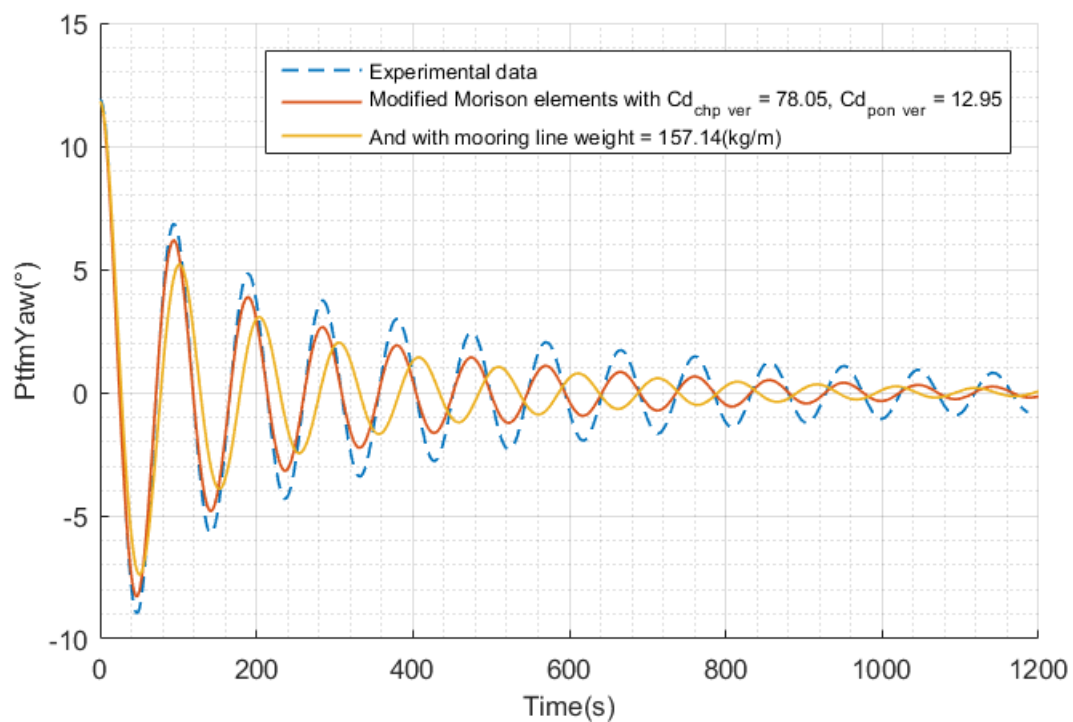


Figure 4-9: Comparison of moored yaw decay simulation with experimental data

4.2.2.9 Summary

The following table shows the tuned properties after the moored decay tests from the Modified Morison elements model.

Table 4-11: Tuned properties after decay tests

	Modified Morison Model	Test	Percentage deviation
Moored Yaw frequency (Hz)	0.0100	0.0110	10.0%
Moored Pitch frequency (Hz)	0.0322	0.0314	2.5%
Moored Heave frequency (Hz)	0.0511	0.0527	3.1%
Moored Surge frequency (Hz)	0.0082	0.0079	3.6%
Damping coefficient column heave plates vertical (Cd_col_ver)	78.05	-	-
Damping coefficient pontoon heave plates vertical (Cd_pon_ver)	12.95	-	-
Damping coefficient column lateral (Cd_col_lat)	0.715	-	-
Damping coefficient heave plate lateral (Cd_hp_lat)	2.05	-	-
Specific weight mooring lines (kg/N)	157.14	-	-

4.2.3 Results

With the obtained drag coefficients and global damping values of the free decay tests simulations of additional test cases will be shown in this section.

4.2.3.1 DLC1.6 PM H7.7 T12.4 D0: Load Case No Wind

In order to better understand the tuned Morison Element model's response, it is compared to the test scenario of extreme waves with the case of a Pierson Moskowitz spectrum with a significant wave height of 7.7m and a peak period of 12.4s. As mentioned beforehand, the wave height sensor in the test was used as input to the simulations.

The simulations with irregular waves are of 11800 second and the first 1000s are cut. This is the same as with the experimental data. Following, the results are presented in the plot.

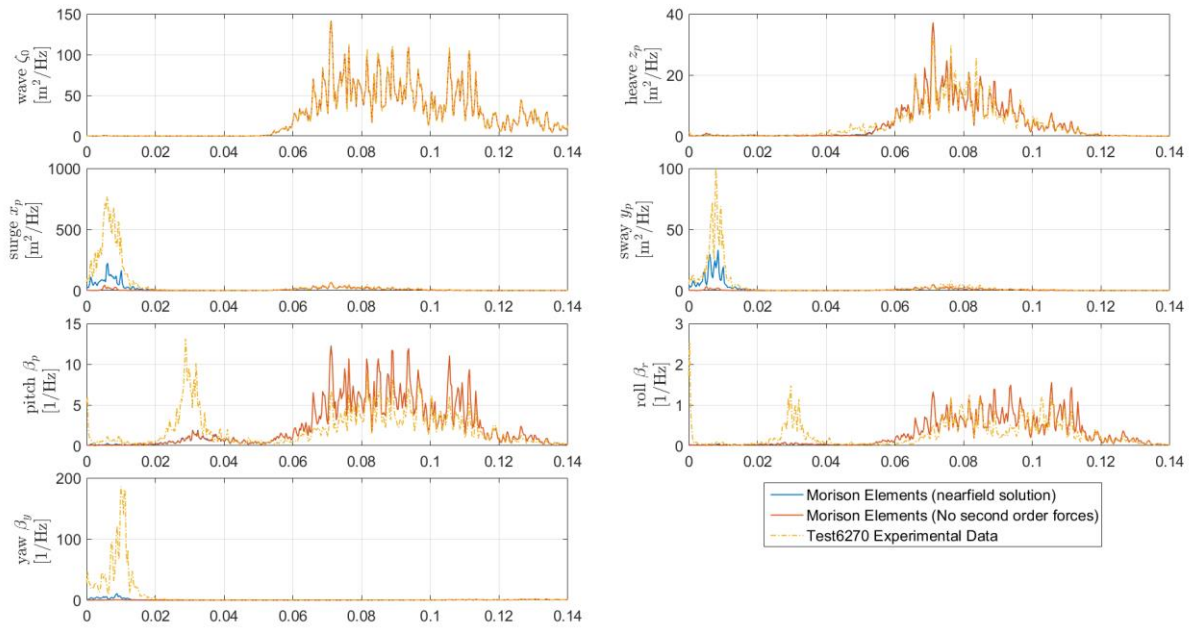


Figure 4-10: Comparison in the frequency domain of the simulation with experimental data for different FAST models for Test 6270. The x-axis is in Hz.

Figure 4-11 shows the response of the model with different hydrodynamics. It is seen that the FAST model with Morison elements with no second order forces cannot approximate the low frequency response in surge, sway, pitch, roll, and yaw. Once the 2nd-order slow-drift forces, computed with Newman's approximation, are used in the model, the response of the surge, yaw and sway in the low frequency range is shown. The response however in these degrees of freedom seems to be overdamped for the low frequency range below 0.04Hz.

To be able to better capture the pitch and roll response, the model coefficients of drag need to be further tuned to be able to include the load case specific conditions. The need for load case specific coefficients has already been shown in the publication from [18]. However, after several iterations it was found that the applied setup of the FAST8 model with MoorDyn was not able to reproduce excitation of the resonant frequency in pitch, even when the all the Morison elements (both in the vertical and the lateral direction) in the model were given nulls as their damping coefficients. This is shown in. Figure 4-12.

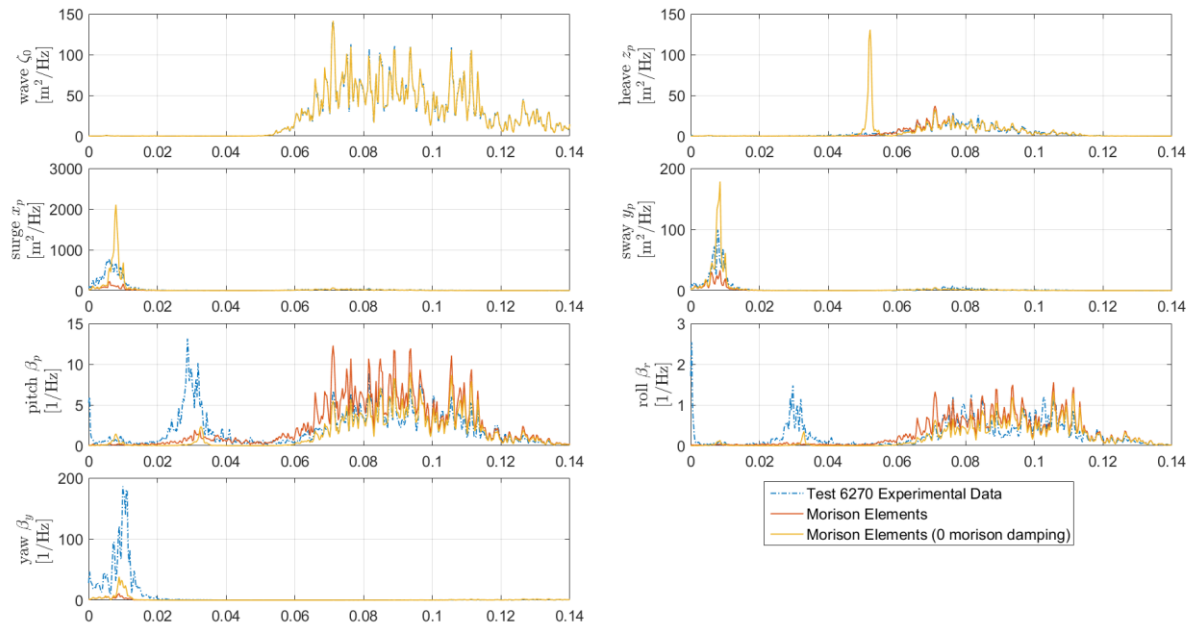


Figure 4-11: Comparison in the frequency domain of the simulation with experimental data for different FAST models for Test 6270. The x-axis is in Hz.

As is seen, neither the pitch, roll nor yaw show significant effect from the elimination of the Morison damping coefficients, which is not something expected. After some analysis of the damping values used in MoorDyn and due to the observation just mentioned, it was decided to run the same test run but instead of using the MoorDyn model, the MAP++ mooring model. MAP++ provides though the static line forces and does not account for the inertial forces and fluid drag loads.

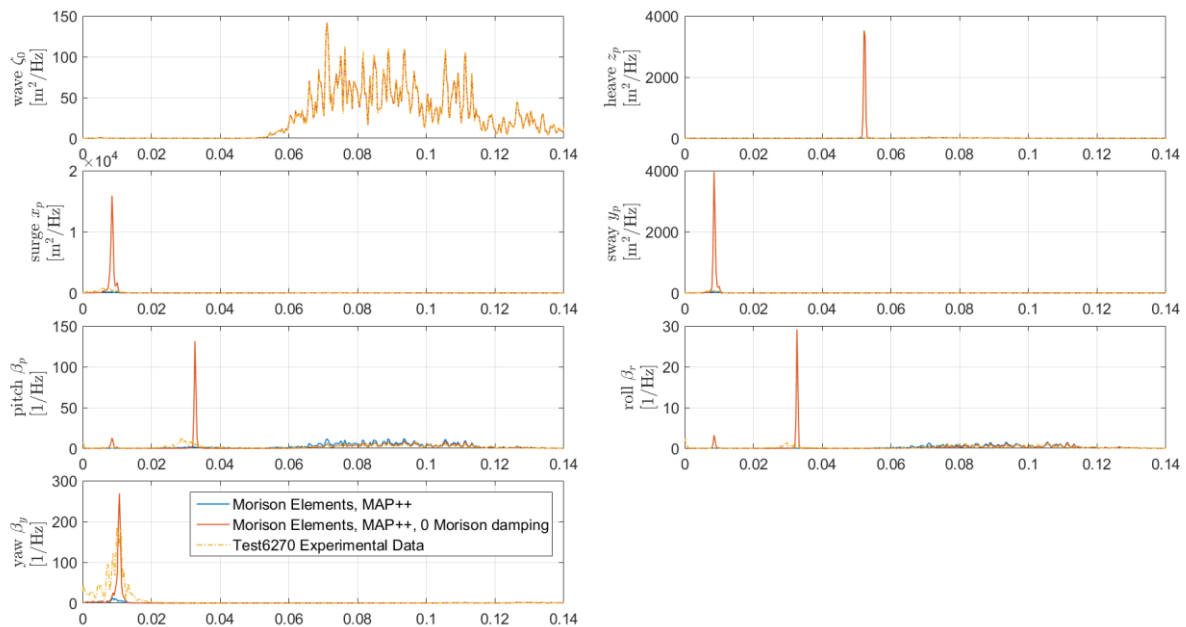


Figure 4-12: Response in the frequency domain of the simulation with MAP++ mooring model with null drag coefficients of drag for the Morison elements for Test 6270. The x-axis is in Hz.

In Figure 4-13 one case see the results from the MAP++ simulations. The MAP++ model does show, as expected, the over-excitation of not having any Morison damping in all degrees of freedom. A more in-depth analysis would be necessary to pinpoint the exact cause of the overdamped response from the

applied MoorDyn setup. This further analysis could include a sensitivity analysis of the coefficients of drag from the lines as well as, updating the modelling of the mooring line since the wave basin model has 3 different line segments per mooring line (see D3.4) as supposed to the simulated model which only has one-line segment per mooring line (see D4.5). However, further results only use the MAP++ mooring model in order to allow a broader sensitivity study on the drag.

Tuning of the Morison elements coefficients of drag for the lateral and vertical values used in the model showed to have certain trade-offs or unwanted side-effects. While trying to tune the surge and yaw response, the coefficient of drag in the lateral direction for the columns and the pontoons were decreased. As shown in Figure 4-14, decreasing the damping to Cd_{col_lat} to 0.3575 and $Cd_{pon_lat} = 1.025$, gives a good response in the low frequency range for the surge response. The yaw response, however, is still overdamped and the coefficients of drag need to be lowered even more for it to show the larger response of the tests. This comes at the expense of an over-excited surge sway and roll response in the low frequency range. The pitch response in the range of 0.02-0.04Hz seems to not be sufficiently excited by simulation model. There is the possibility that for this range, Newman's approximation underestimates the second-order difference-frequency wave forces. A further analysis is planned for LIFES50+ D4.8 with the full Quadratic Transfer Function (QTF).

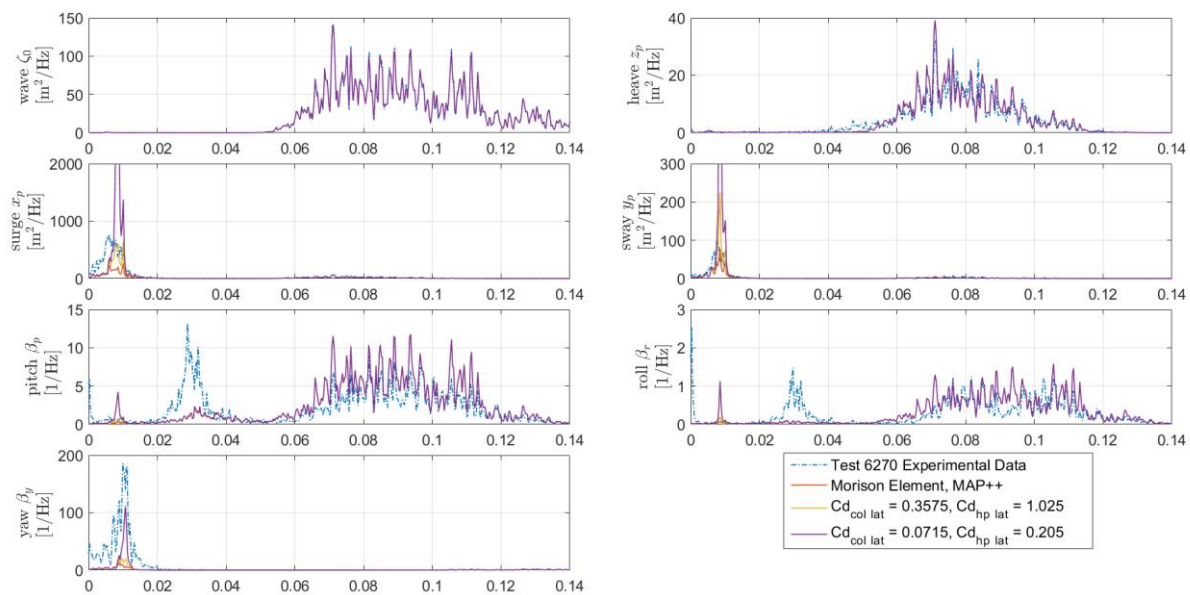


Figure 4-13: Response in the frequency domain of the simulation with MAP++ mooring model, for different values of the lateral coefficients of drag for different FAST models for Test 6270. The x-axis is in Hz.

In the case of tuning of the pitch, lower coefficients of drag for the Morison elements in the vertical direction were used. Figure 4-15 shows how decreasing the vertical coefficients of drag has only a minimal effect on the low frequency pitch response, with a low range of frequency response compared to the test. As a side effect, the heave response around the heave natural frequency increases significantly.

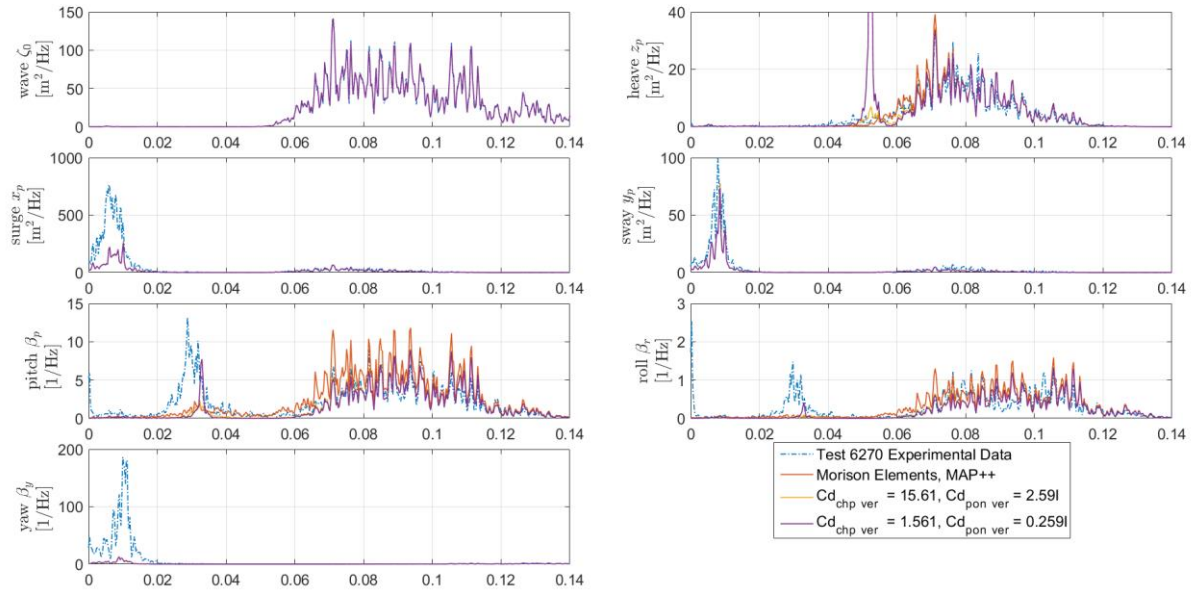


Figure 4-14: Response in the frequency domain of the simulation with MAP++ mooring model, for different values of the vertical coefficients of drag for different FAST models for Test 6270. The x-axis is in Hz.

4.2.3.2 DLC1.6 PM H10.9 T15.0 D0: Load Case No Wind (Test 6241)

One further load case with irregular waves is used for comparisons of the model. The test uses a Pierson Moskowitz spectrum with 10.9m significant wave height and 15.0s peak period. Similar to the previous case with irregular waves, a first comparison is made between the different hydrodynamic forcing options. The response of the displacements of the platform in the frequency domain is shown in the following figure.

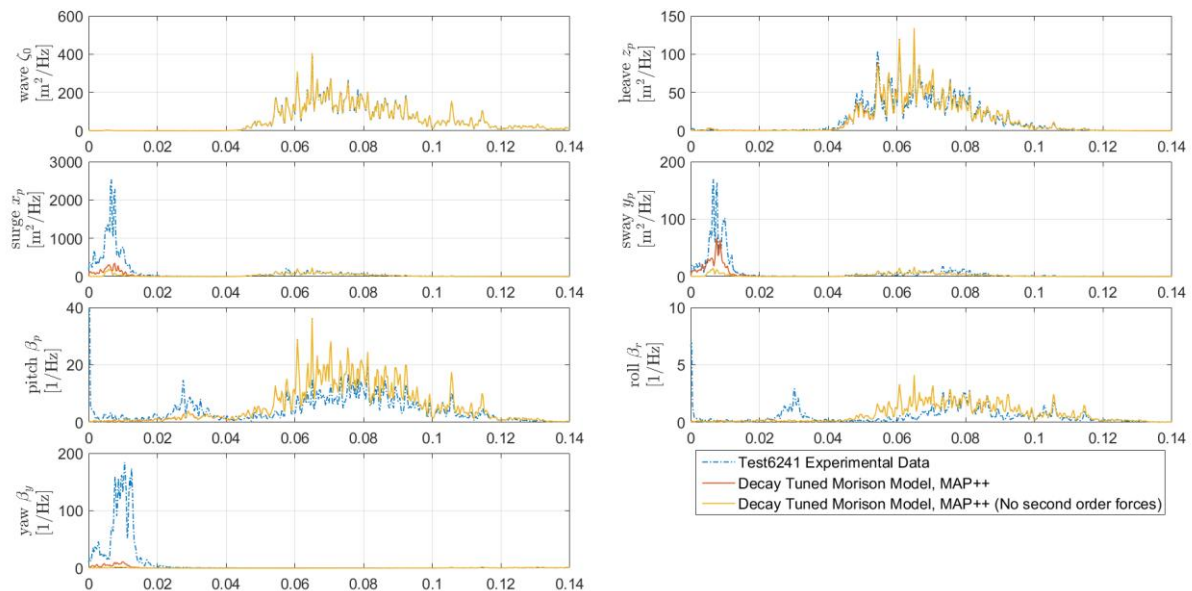


Figure 4-15: Comparison in the frequency domain of the simulation with experimental data for different FAST models for Test 6241. The x-axis is in Hz.

Similar to Figure 4-11, the response of the simulations of Figure 4-16 does not reproduce the excitations around the Eigen-frequencies of the different DOFs. In this case, the energy in the waves is larger compared to the test case 6270, and thus, unlike in Figure 4-11, it is not so evident that the pitch response at the Eigen frequency is also underestimated.

4.2.3.3 Pink Noise H4 D0: Load Case No Wind (Test 4220)

The pink noise test was also simulated in FAST. This case has a lower significant wave height of 4m.

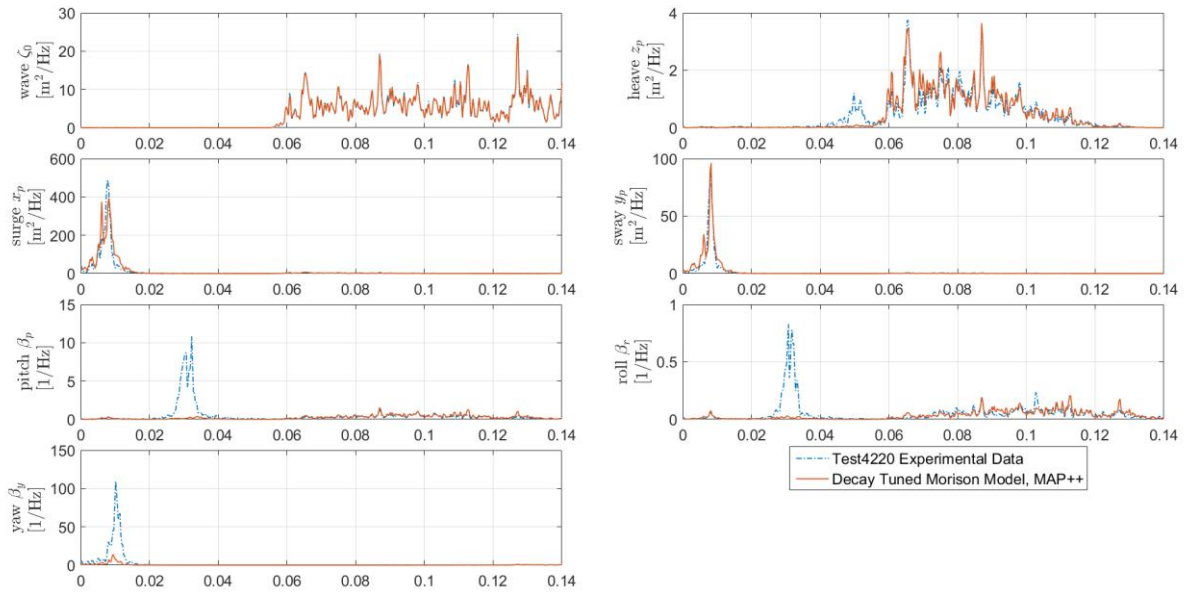


Figure 4-16: Response in the frequency domain of the simulation with MAP++ mooring model for Test 4220. The x-axis is in Hz.

The simulation results show a good agreement for the surge and sway, yet for the pitch, roll and yaw there is still a low response at the Eigen frequency of the platform. The heave DOF shows good agreement for the wave frequencies above 0.06Hz but is over damped for the case of the Eigen frequency. Again, tuning of the vertical drag coefficients has been attempted.

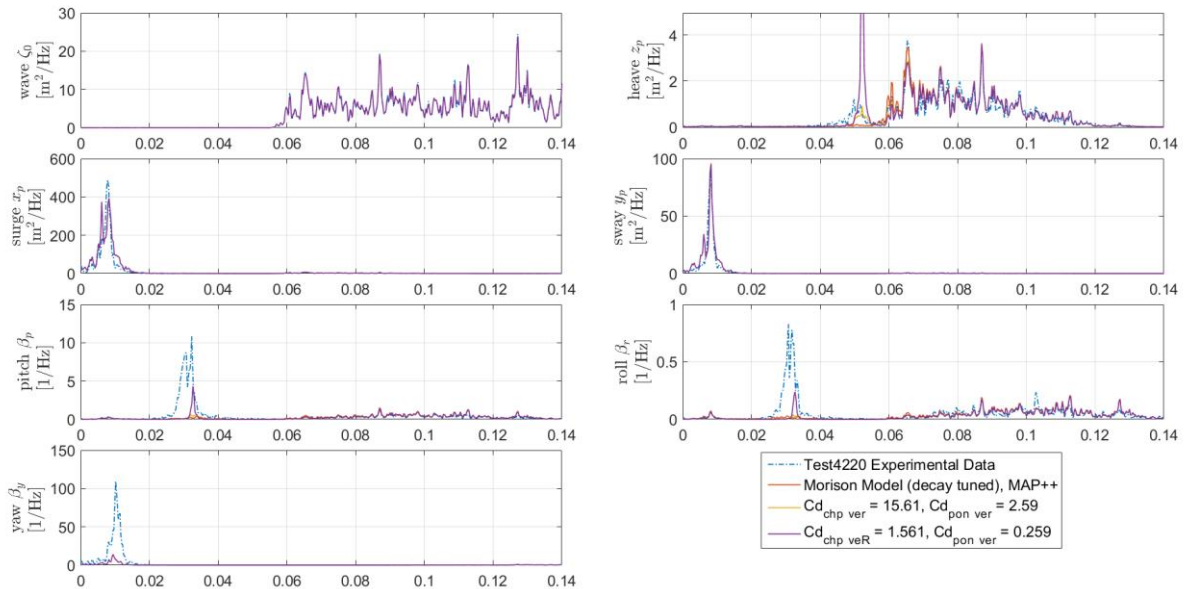


Figure 4-17: Response in the frequency domain of the simulation with MAP++ mooring model for Test 4220 with changing vertical coefficients of drag for the column heave plates and the pontoon heave plates. The x-axis is in Hz.

In Figure 4-17, again the trade off in the pitch and heave response can be seen, and as the pitch response improves, the heave response increases beyond the test results, for the region at around their Eigen frequencies. The same behaviour was noted for the irregular wave test

4.3 Comparison to a low-order model

In order to assess the validity of simpler models in comparison the Nautilus-DTU10 measurement data, a low-order model is employed as for the OO-Star Wind Floater Semi 10MW design. The low-order model used here is comparable to the one by Pegalajar-Jurado [21] used for the OO-Star Wind Floater Semi 10MW platform. Both models were directly compared in LIFES50+ D4.1 [5]. The assumptions will be introduced in the following.

4.3.1 Simplified low-order wind turbine (SLOW)

The SLOW model has been developed as coupled FOWT model with a focus on an optimal trade-off between computational efficiency and accuracy. The objective is a good representation of the overall system dynamics, meaning the platform motion, the tower bending and the rotor speed. The advantages of the model is to fill an existing gap of FOWT design tools between uncoupled static tools and aero-hydro-servo-elastic tools like FAST. It allows a good representation of the main dynamic properties of a design, which allows early stage sensitivity studies and optimization in the early design phase of the concept. The equations of motion are derived from physical first-principles and thus, the model is a white-box model without fitted or identified models or submodels. The structural model equations of motion are symbolic allowing computational efficient simulations. The model allows evaluations about 120 times as fast (time-domain) or faster (frequency domain) compared to state-of-the-art tools (e.g. FAST). This also enables portability for online model execution e.g. on a prototype for monitoring and model-predictive control applications.

The model has been used previously in LIFES50+ for loads analysis in D4.1 [5] and for an integrated optimization in D4.3 [29] with results published in [30]. It was used for FOWT control design studies in [31]. A comparison with scaled experiments of the TripleSpar design [32] was performed in [18]. A comprehensive description can be found in [33], of which a summary is presented here.

From the nonlinear equations of motion, linearized equations are derived. Thus, all physical assumptions of the submodels for hydrodynamics, aerodynamics, structural dynamics and mooring dynamics stay identical, except for the linearization. Hence, the influence of nonlinearity can be clearly assessed.

The structural equations of motion are derived using the formalized Newton-Euler algorithm [34], which allows a user-defined multibody layout. Thus, the tool is not limited to a given wind turbine, but new bodies like tuned-mass dampers or additional DOFs can be defined individually by the user. The representation of flexible bodies follows the theory of flexible multibody system, taking into account centrifugal, gyroscopic and Coriolis forces and the rigid-elastic couplings. The model used in this work has five DOFs: platform surge, heave and pitch, one DOF for the tower fore-aft deformation and the rotor speed. This planar 2D-model neglects any lateral motion response, but it captures the main response to aligned wind and waves. In the present work, a 15deg-misalignment angle between the Nautilus DTU-10 coordinate system and the 0-deg wave heading angle is present [4]. The 2D plane, where a floater motion is allowed is still aligned with the body-fixed surge axis.

The aerodynamic force model is a quasi-static actuator disk model. It avoids the iteration of standard BEM algorithms by modelling the wind turbine rotor as a rigid disk. The forces however, are a function of the Tip-Speed Ratio (TSR) and the blade pitch angle assessed in a pre-processing step. Therefore, the dynamics related to the generator torque and the blade pitch controller are accounted for. The model requires a BEM algorithm only as a pre-processing to obtain the rotor power and thrust coefficients.

The hydrodynamic model is based on a simplified representation of the Cummins equation. It assumes a constant added mass matrix, independent of the frequency, according to [35]. The potential/radiation

damping is completely neglected. This allows for equations of motion independent of the frequency with a significant increase of computational efficiency. It is shown in [33] that for most FOWT platforms the radiation damping is large at frequencies outside the resonance frequencies. At the resonance frequencies, damping forces are of little importance to the response.

Morison drag is accounted for through a flexible node-based mesh for horizontal and vertical directions, comparable to HydroDyn [36]. The quadratic drag can be linearized through a stochastic linearization and an efficient separation of the wave excitation force and the damping force. The procedure is detailed in [37].

The mooring lines are modelled through a quasi-static model, derived from the same equations as used in FAST v7 [38]. For the linearization, a perturbation analysis gives a generalized stiffness matrix about a user-defined reference point.

In comparison to the model used for the OO-Star Wind Floater Semi 10MW platform [21], the main difference is the equivalent time-domain and frequency-domain formulation and the aerodynamic model. While the previous model is based on aerodynamic force time series precomputed by FAST, the present model uses a scalar rotor-effective wind time series, which can be computed by TurbSim [39] or others.

The objective of applying simplified models in this work, next to FAST, is to assess its validity for the NAUTILUS-DTU10 concept. The comparison against FAST and the experimental data shall indicate its limitations in order to set clear boundaries for its use within the design phases of FOWTs. Dedicated model fidelities for the different design phases shall streamline the future FOWT development and the adaptation of FOWT concepts to specific site conditions.

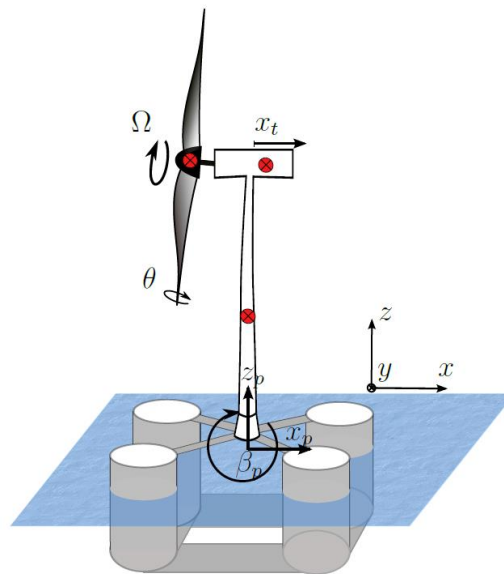


Figure 4-18: Simplified low-order wind turbine model (SLOW) mechanical sketch

4.3.2 Test Comparisons

A SLOW model of the NAUTILUS-DTU10 platform was created with the exact same settings as the FAST model in order to compare it to the test data. Two cases were used for comparison, Test6270 and Test4220, as described in the previous section and in D3.4. One represents extreme waves and the other a pink noise test. The comparisons were made with a focus on the numerical models. Therefore, the simplified setting of drag coefficients as shown in Table 4-12 was used for both, SLOW and FAST. The

horizontal column drag and the vertical pontoon drag is equal to the above cases, while the vertical drag at the column lower end and the horizontal pontoon drag are set to zero.

Table 4-12: Morison drag settings for model comparison

	Drag coefficient column heave plates vertical (Cd_col_ver)	Drag coefficient pontoon heave plates vertical (Cd_pon_ver)	Drag coefficient column lateral (Cd_col_lat)	Drag coefficient heave plate lateral (Cd_hp_lat)
Test 4220	0.0	2.59	0.715	0.0
Test 6270	0.0	12.95	0.36	0.0

Figure 4-20 shows the PSD for both models and the experiment. It can be seen that the low-frequency surge x_p and heave z_p response is well captured as well as the first-order wave response around 0.1 Hz. Above is the tower natural frequency which is also reflected in the results. The surge resonance response is under-predicted by the models, due to the selected column drag coefficients.

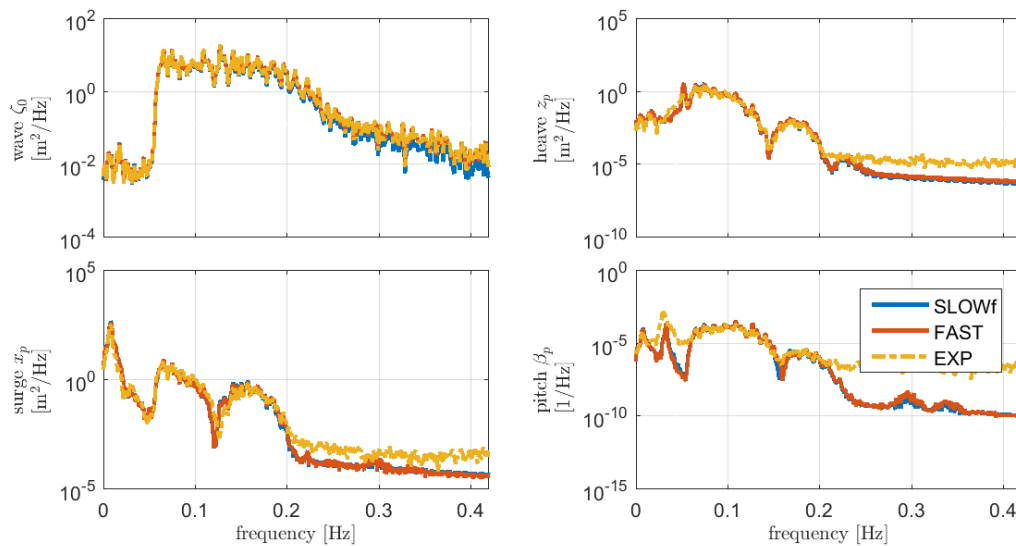


Figure 4-19: Comparison Test 4220 of FAST, SLOW against experiments, spectra

The time series ζ_0 of Figure 4-21 have been produced by shifting the measured time series of the WAVE01 probe, see [4], from the sensor location to the platform position of 180m. This was done through a transformation to the frequency-domain, a frequency-dependent phase transformation, and a subsequent re-transformation to the time-domain. It can be seen that the response is well in phase for the platform signals. There is a static offset in surge and pitch (β_p), which suggests that the numerical models underpredict the mean drift forces through Newman's approximation.

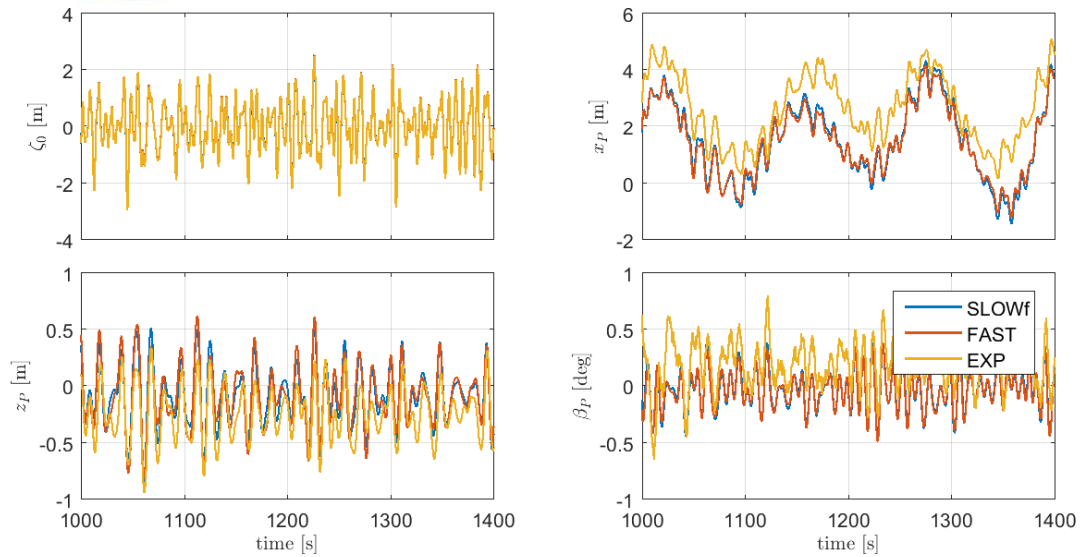


Figure 4-20: Comparison Test 4220 of FAST, SLOW against experiments, time series

Figure 4-22 shows the PSDs of the pink noise tests. They have a comparable agreement among SLOW, FAST and the experiments with an under-prediction of the surge resonance motion.

The time series of Figure 4-23 show again a good agreement in terms of phase. In this test, the mean simulated response in pitch agrees better with the measurements, while the measured mean surge displacement is still larger than the numerical. It will have to be assessed in future works if this is a result of Newman's approximation.

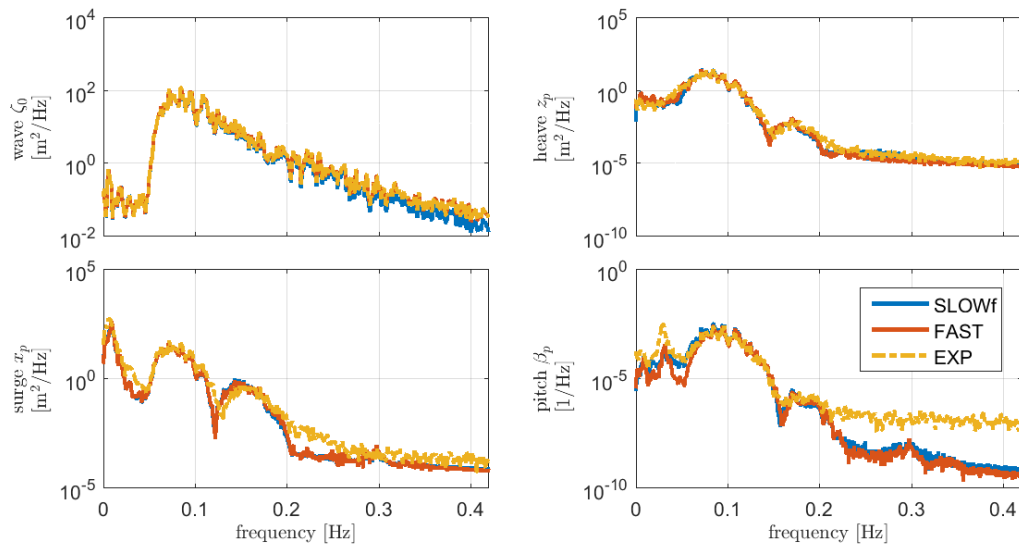


Figure 4-21: Comparison Test 6270 of FAST, SLOW against experiments, spectra

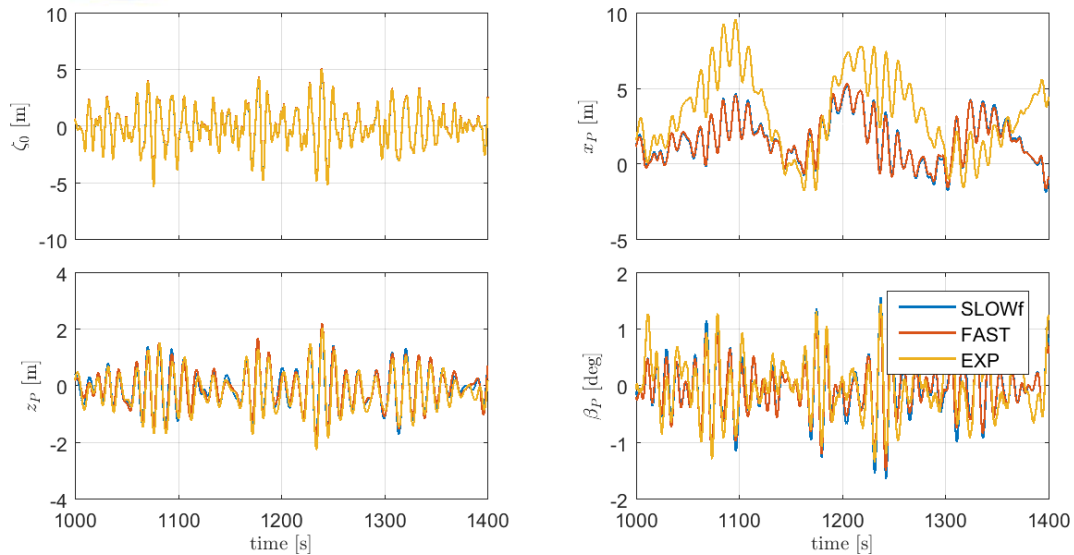


Figure 4-22: Comparison Test 6270 of FAST, SLOW against experiments, time series

The comparison shows that the reduced-order model is well able to capture the Eigen frequencies of the platform and the tower, including the mooring system. The Morison drag-induced damping, the Morison drag-induced excitation and the potential wave force models give the same response as FAST. This suggests that it is possible to use computationally more efficient, simplified models for an assessment of the mentioned dynamics. This can be of advantage in early design stages or for sensitivity studies.

4.4 Conclusions for the NAUTILUS-DTU10

The exercise of the present sections for the NAUTILUS-DTU10 platform has shown that separate identifications of the component properties are necessary before combining them in a coupled FOWT experiment. The hydrodynamic viscous drag depends on different non-dimensional numbers, which include the amplitude of oscillation. Therefore, the drag of the mooring lines, as well as the member-based drag of the floating platform, needs to be identified for various amplitudes of motion. Additionally, damping could come from power or signal cables. Such a separate identification of the components is necessary to minimize the uncertainty with coupled FOWT experiments.

In summary, the following findings were obtained:

- Tuning of the drag coefficients to the experimental data can lead to an approximation of the free decay tests. When the moored decay tests were compared, tuning of the mooring model was needed to be able to reach to better match the Eigen-frequencies of the yaw and surge DOFs.
- The analysis of the irregular wave test showed several response phenomena. For the employed setup, the best results for pitch, roll and yaw response was achieved by application of the quasi-static MAP++ mooring model.
- No global damping values were able to provide a satisfactory response for all tests analysed. It is thus clear that the tuned model needs sea state-specific values for the coefficients of drag as suggested in Lemmer et al. [18], and as done with the linear damping coefficients for the OO-Star Wind Floater Semi 10MW. The tuning obtained from the decay tests was thus not sufficient for replication of all the platform DoFs for the irregular wave test cases and the pink noise test.
- For the pink-noise wave test with lower significant wave height of 4 m, the model was able to reach the experimental response of heave, surge and sway with appropriate tuning.

The results also highlight a couple of shortcomings which can either be solved by further model adjustment or is recommended for investigation as further work:

- The physical mooring system consists of 3 segments per mooring line with each one having different lengths, specific weight and elasticity. In the present modelling setup, a simplified representation with only one segment per line was used, but was found to over-damp the pitch, roll and yaw degrees of freedom. Better results were achieved with the quasi-static MAP++ mooring model and it was left for further investigation to clarify the damping aspects of the applied MoorDyn setup.
- The mooring lines have an important effect on the damping of surge, sway and yaw. Large yaw excitations were found in the tests for irregular waves and pink noise, and thus further investigation is needed to be able to determine why the mooring simulation model was not able to reproduce them. This could be due to the simplified mooring line representation and the quasi-steady modelling approach that is likely to affect the mooring damping.
- For the extreme irregular wave cases, tuning of the vertical coefficients of drag and lateral coefficients of drag was found to have trade-offs with respect to the platform response. This effect did not fully allow an appropriate solution to best describe the response of all DOFs from the simulations. There were certain trade-offs between the response of the DOFs, as one response would improve but the other would worsen.
- Under-prediction of the low-frequency pitch, roll and yaw response were observed in the irregular wave test cases. While this may be a result of an incomplete damping description, the modelling error of the Newman approximation may also explain the deviation. A comparison of the Newman approximation and modelling with the full QTF is thus planned as future work.

Finally, in the comparison of the reduced order SLOW model to the State-of-the-art FAST model, it was found that the reduced-order model is well able to capture the floating wind turbine systems. The Morison drag-induced damping, the Morison drag-induced excitation and the potential wave force models give the same response as FAST. This suggests that it is possible to use computationally more efficient, simplified models for an assessment of the mentioned dynamics.

5 Conclusions

The design driving load cases for both the OO-Star Wind Floater Semi 10MW and the For the NAUTILUS-DTU10 has been identified, summarizing work of D7.7. Next, comparison of calibrated state-of-the-art models in FAST to the experimental results of the Ocean Basin tests were presented, followed by a comparative analysis with the simplified QULAF and SLOW models.

The findings for the two floater studies can be summarized as follows.

For the OO-Star Wind Floater Semi 10MW:

- Regarding the design-driving load cases, studies carried out in WP7 indicate that DLC 1.2, 1.6 and 6.1 are design driving. Failure conditions such as loss of mooring lines (DLC 10.x) also generates design-driving loads which are, however, highly dependent on floater design details.
- In the comparison between the state-of-the-art numerical model and the physical tests, it has been shown that calibration of the linear and quadratic global damping matrices against the decay tests is not sufficient to predict the response to waves. On the other hand, if the global linear damping matrix is calibrated for each specific sea state, the model is able to reproduce the measured response with errors up to 13% in the 95% percentile, with most cases under 8%.
- The simplified model can predict the damage-equivalent bending moment at the tower base with errors up to 11.3% for the operational wind speed range. The largest deviations in wave-only conditions occur for severe wave climates due to the absence of viscous drag forcing. In cases with wind, the largest deviations are observed for wind speeds around rated, due to the different load regions for the controller and to the overprediction of the aerodynamic damping on the tower. The simplified model is between 1300 and 2700 faster than real time.

For the NAUTILUS-DTU10:

- Studies of WP7 indicate that DLC 1.2, 1.6 and 6.1 are design driving.
- The calibrated FAST model was able to provide a good match for the decay tests upon tuning on the Morison drag coefficients. For the irregular sea state cases, the low-frequency response was generally under-predicted. This was linked to a simplified and quasi-static representation of the mooring system; difficulties in achieving a calibrated damping that could reproduce all DOFs accurately at the same time; and possible in-accuracies in the applied Newman approximation for the second-order forcing. The latter will be investigated as further work in D4.8 on advanced model validation.
- In the comparison of the reduced order SLOW model to the State-of-the-art FAST model, it was found that the reduced-order model is well able to capture the floating wind turbine systems. The Morison drag-induced damping, the Morison drag-induced excitation and the potential wave force models give the same response as FAST. This suggests that it is possible to use computationally more efficient, simplified models for an assessment of the mentioned dynamics.

As a general conclusion for both floater studies, it was found that calibration of hydrodynamic coefficients in time domain simulations of floating wind turbines is essential to achieve sufficiently accurate load predictions. The results demonstrate that pre-calculations of hydrodynamic coefficients with potential flow codes could provide good starting points for the simulations but cannot replace the additional adjustment against the basin model tests. Further, for both floaters, sea-state dependent calibration of the damping was needed to achieve comparable dynamic behaviour of the basin model and the simulation model.

The presented simplified QuLAF and SLOW models provide a big benefit for concept and design studies. After setting up the linearised system matrices the frequency domain tool enables calculations of the response to fatigue loading from stochastic sea states and turbulent wind within a fraction of the computational effort of a time domain simulation. This is of interest for efficient pre-design and allows for application of optimization routines in the initial design.

6 References

- [1] W. Yu, K. Müller and F. Lemmer, “LIFES50+ D4.2: Public definition of the two LIFES50+ 10MW floater concepts,” University of Stuttgart, 2018.
- [2] A. Pegalajar-Jurado, F. Madsen, M. Borg and H. Bredmose, “LIFES50+ D4.5: State-of-the-art models for the two LIFES50+ 10MW floater concepts,” 2018.
- [3] K. Müller, Faerron-Guzmán and M. a. M. A. Borg, “D7.7 Identification of critical environmental conditons and design load cases. Deliverable of the LIFES50+ project”.
- [4] M. Thys, H. S. Andersen, T. Landbø, G. P. Moran and J. G. Fernandez, “LIFES50+ D3.4: Ocean Basin Test Report,” SINTEF Ocean, 2018.
- [5] F. Lemmer, K. Müller, A. Pegalajar-Jurado and M. a. B. H. Borg, “D4.1 Simplified numerical models for up-scaled design.,” DTU , 2016.
- [6] C. Bak, F. Zahle, R. Bitsche, T. Kim, A. Yde, L. Henriksen, A. Natarajan and M. Hansen, “Description of the DTU 10 MW reference wind turbine,” 2013.
- [7] J. Jonkman and B. Jonkman, “NWTC Information Portal (FAST v8),” 2016. [Online]. Available: <https://nwtc.nrel.gov/FAST8>.
- [8] M. Hall, “MoorDyn,” 2017. [Online]. Available: <http://www.matt-hall.ca/moordyn.html>.
- [9] C. Lee and J. Newman, “WAMIT,” 2016. [Online]. Available: <http://www.wamit.com/>.
- [10] W. Cummins, “The impulse response functions and ship motions,” *Schiffstechnik*, vol. 9, pp. 101-109, 1962.
- [11] J. Jonkman, “Dynamics of offshore floating wind turbines - Model development and verification,” *Wind Energy*, vol. 12, no. 5, pp. 459-492, 2009.
- [12] A. Pegalajar-Jurado, H. Bredmose, M. Borg, J. Straume, T. Landbø, H. Andersen, W. Yu, K. Müller and F. Lemmer, “State-of-the-art model for the LIFES50+ OO-Star Wind Floater Semi 10MW floating wind turbine,” *Journal of Physics: Conference Series*, 2018.
- [13] J. Frias Calvo, “Response analysis of an offshore floating 10MW wind turbine support structure, M.Sc. thesis,” DTU Wind Energy M-0184, Kgs. Lyngby, Denmark, 2017.
- [14] A. Krieger, G. Ramachandran, L. Vita, G. Gómez-Alonso, J. Berque and G. Aguirre, “LIFES50+ D7.2: Design basis,” 2015.
- [15] K. Müller, R. Faerron Guzman, P. W. Cheng, J. Galván, M. Sánchez Lara, R. Rodriguez Arias and A. Manjock, “Load Sensitivity Analysis for a Floating Wind Turbine on a Steel Semi-Submersible Substructure,” *Proceedings of the 1st International Offshore Wind Technical Conference IOWTC2018*, November 2018.



- [16] M. Borg, H. Bredmose, H. Stiestal, A. Pegalajar-Jurado, F. Madsen, T. Nielsen, R. Mikkelsen, M. Mirzaei and A. Lomholt, “Physical model testing of the TetraSpar floater in two configurations. Part I: Experimental setup and hydrodynamic analysis,” *Marine Structures* (submitted), 2018.
- [17] P. A. Berthelsen, E. Bachynski, M. Karimirad and M. Thys, “Real-time hybrid model tests of a braceless semi-submersible wind turbine. Part III: Calibration of a numerical model,” in *Proceedings of the ASME 35th International Conference on Ocean, Offshore and Arctic Engineering*, Busan, Korea, 2016.
- [18] F. Lemmer, A. Pegalajar Jurado, W. Yu, M. Borg, R. Mikkelsen, P. W. Cheng and H. Bredmose, “The Triplespar campaign: Validation of a reduced-order simulation model for floating wind turbines,” Vols. Proceedings of ASME 2018 37th International Conference on Ocean, Offshore and Arctic Engineering, no. OMAE2018-78119, 2017.
- [19] M. Kvittem, P. Berthelsen, L. Eliassen and M. Thys, “Calibration of hydrodynamic coefficients for a semi-submersible 10MW wind turbine,” in *37th International Conference on Ocean, Offshore and Arctic Engineering*, Madrid, Spain, 2018.
- [20] A. Pegalajar-Jurado and H. Bredmose, “Reproduction of slow-drift motions of a floating wind turbine using second-order hydrodynamics and Operational Modal Analysis,” *Marine Structures* (in review), 2018.
- [21] A. Pegalajar-Jurado, M. Borg and H. Bredmose, “An efficient frequency-domain model for quick load analysis of floating offshore wind turbines,” *Wind Energy Science*, vol. 3, no. 1, pp. 693-712, 2018.
- [22] J. Morison, J. Johnson and S. Schaaf, “The force exerted by surface waves on piles,” *Journal of Petroleum Technology*, vol. 2, no. 05, pp. 149-154, 1950.
- [23] S. Schlør, L. Garcia-Castillo, M. Fejerskov, E. Stroescu and H. Bredmose, “A model for quick load analysis for monopile-type offshore wind turbine substructures,” *Wind Energy Science*, vol. 3, no. 1, pp. 57-73, 2018.
- [24] T. Larsen and T. Hanson, “A method to avoid negative damped low frequent tower vibrations for a floating, pitch controlled wind turbine,” *Journal of Physics: Conference Series*, vol. 75, no. 1, 2007.
- [25] J. Jonkman, “Influence of control on the pitch damping of a floating wind turbine,” in *Proceedings of the 46th AIAA Aerospace Sciences Meeting and Exhibit*, Reno, USA, 2008.
- [26] M. Longuet-Higgins, “Statistical properties of a moving waveform,” *Proceedings of the Cambridge Philosophical Society*, vol. 52, pp. 234-245, 1956.
- [27] A. Naess and T. Moan, *Stochastic dynamics of marine structures*, 1st ed., Cambridge University Press, 2013.

- [28] F. Madsen, A. Pegalajar-Jurado, H. Bredmose, M. Borg, K. Müller and D. Matha, "LIFES50+ D7.8: Required numerical model fidelity and critical design load cases in various design phases," 2018.
- [29] F. Lemmer, K. Müller, W. Yu, R. Faerron-Guzmán and M. Kretschmer, "LIFES50+ D4.3: Optimization framework and methodology for optimized floater design," 2016.
- [30] F. Lemmer, K. Müller, W. Yu, D. Schlipf and P. W. Cheng, "Optimization of floating offshore wind turbine platforms with a self-tuning controller," in *Proceedings of the ASME 36th International Conference on Ocean, Offshore and Arctic Engineering*, Trondheim, 2017.
- [31] F. Lemmer, D. Schlipf and P. W. Cheng, "Control design methods for floating wind turbines for optimal disturbance rejection," *Journal of Physics: Conference Series*, vol. 753, 2016.
- [32] F. Lemmer, F. Amann, S. Raach and D. Schlipf, "Definition of the SWE-TripleSpar platform for the DTU10MW reference turbine," 2016.
- [33] F. Lemmer, W. Yu, D. Schlipf and P. W. Cheng, "Multibody Modeling for Concept-Level Floating Offshore Wind Turbine Design (to be submitted)," *Multibody System Dynamics*, 2018.
- [34] W. Schiehlen and P. Eberhard, *Applied Dynamics*, 1st ed., Springer International Publishing, 2014.
- [35] R. Taghipour, T. Pérez and T. Moan, "Hybrid frequency-time domain models for dynamic response analysis of marine structures," *Ocean Engineering*, vol. 35, pp. 685-705, 2008.
- [36] J. Jonkman, A. Robertson and G. Hayman, "HydroDyn user's guide and theory manual," Boulder, 2014.
- [37] F. Lemmer, W. Yu and P. W. Cheng, "Iterative frequency-domain response of floating wind turbines with parametric drag," *Journal of Marine Science and Engineering*, vol. 6, 2018.
- [38] J. Jonkman, "Dynamics modeling and loads analysis of an offshore floating wind turbine," 2007.
- [39] B. Jonkman and L. Kilcher, "TurbSim user's guide," Boulder, 2009.